UNIVERSITY OF OKLAHOMA

GRADUATE COLLEGE

PASSIVE RADAR CLUTTER MODELING AND EMITTER SELECTION FOR GROUND MOVING TARGET INDICATION

A DISSERTATION

SUBMITTED TO THE GRADUATE FACULTY

in partial fulfillment of the requirements for the

Degree of

DOCTOR OF PHILOSOPHY

By

JAMES R. LIEVSAY
Norman, Oklahoma
2017

PASSIVE RADAR CLUTTER MODELING AND EMITTER SELECTION
FOR GROUND MOVING TARGET INDICATION

A DISSERTATION APPROVED FOR THE
SCHOOL OF ELECTRICAL AND COMPUTER ENGINEERING

BY

Dr. Nathan Goodman, Chair

Dr. Caleb Fulton

Dr. Julie Jackson

Dr. Robert Palmer

Dr. Mark Yeary

To Corrie, Jackson and Ava.

Acknowledgments

I would like to acknowledge the help I received from several sources. First and foremost, I would like to thank my wife, children, and parents. Their love, support, and sacrifices were invaluable. Second, my advisor, Dr. Nathan Goodman, was instrumental in my research. I could not have made my contributions without his knowledge and expertise. Third, I would like to thank my fellow graduate student, David Lucking. His guidance and feedback improved the quality of my dissertation and research. I would also like to acknowledge my committee members for their hard work and flexibility. Furthermore, I wish to thank Dr. Julie Jackson for sharing the Air Force Institute of Technology's Passive Radar Toolbox. This toolbox generated the signals I needed for my research. I would finally like to thank the administration staff at the Advanced Radar Research Center. They have always been there for me to assist and ensure my successful completion.

Table of Contents

List of Tables

List of Figures

Abstract

Moving target detection with a passive radar system relies on many competing and coupled variables. When simulating a passive bistatic radar (PBR) system for ground moving target indication (GMTI) a three-dimensional model is critical. The signal path geometry induced from separating the radar receiver and transmitter causes several performance effects that change with location.

Since a performance prediction is only as good as the model, the choice of how to model clutter becomes important. Measured data of bistatic clutter shows that the received clutter power depends on scattering angles. Therefore, a new in-plane out-of-plane (IPOP) interpolation model was developed. The IPOP model causes high clutter returns to reside in regions near an in-plane orientation (forward or backward scattering). The model produces a more localized clutter spectrum in angle-Doppler space when compared to monostatic radar.

Generally, the stationary transmitter is modeled as a communication emitter due to the availability. These continuous waveforms must be par-

titioned as pulses spaced at constant intervals over the coherent processing interval (CPI). This diverse pulse train is non-ideal for pulse-Doppler radars. The waveform produces high range sidelobes and causes colored noise to spread in Doppler. It is shown for the first time that these waveform effects can be modeled through a covariance matrix taper (CMT).

Choosing an optimal emitter becomes an interesting problem when multiple emitters are present. A common metric for GMTI when using space-time adaptive processing (STAP) is signal-to-interference-plus-noise ratio (SINR). However, SINR changes based off relative geometries, and GMTI depends on where a target's location and two-dimensional velocity maps into angle-Doppler space. Therefore, average SINR, weighted average SINR, minimum SINR, and usable velocity space fraction (UVSF) are the newly developed metrics proposed for down-selecting to an optimal emitter. The choice of metric is extremely dependent on the scenario.

Finally, in STAP large clutter discretes (LCDs) can cause either false alarms or missed detections. Ultimately, they contaminate the data, and it is very desirable, yet very hard, to remove LCDs. However, the clutter structure in angle-Doppler space for PBR can offer a benefit for removing an LCD. Due to the fact that bistatic clutter can be more localized in angle-Doppler, the detection and estimation of an LCD can be accomplished for an out-of-plane geometry. Then the LCD can be successfully removed from the data,

and new application of spectral estimation techniques have been developed for this purpose.

Chapter 1

Introduction

1.1 Introduction

Passive radar is an area of research that receives much attention. As commercial signals are becoming more accessible, the attractiveness of passive radar increases. Furthermore, there is no need to compete for costly frequency spectrum or invest in any transmitter hardware. With these eliminations, the cost of passive radar systems is reduced.

A passive system can also be considered as a passive bistatic radar (PBR). Generally, many advantages and disadvantages of bistatic systems are also seen in PBR. For ground moving target indication (GMTI), a major disadvantage of bistatic radar is the mitigation of ground clutter. Bistatic clutter filtering efficiency is reduced compared to monostatic clutter filtering because bistatic ground clutter is inherently non-stationary. Stationarity is typically considered in statistics where a random process is stationary if the

statistical moments do not change with time [1]. In radar engineering, clutter is stationary if the statical moments do not vary over space. Measurements across various terrains and over many angles and frequencies have been accomplished and show bistatic radar configurations induce varying clutter statistics over space [2]–[6]. With these measurements, research into the modeling of bistatic ground clutter began [4], [5], [7]–[12].

Not only is bistatic ground clutter non-stationary, but it is also range dependent. While non-stationary clutter is defined in general terms of clutter statistics, range dependent clutter is defined as the clutter spectrum varies in the angle-Doppler domain over range bins. So the structure of this clutter spectrum is strongly dependent on relative geometry, velocities, and antenna configurations of the transmitter and receiver [13], [14]. There are many clutter filtering methods that exist for range dependent clutter including angle-Doppler compensation (ADC) [15], adaptive ADC (A^2DC) [16], adaptive Doppler compensation [17], derivative based updating (DBU) [18], Doppler warping [19], high order Doppler warping (HODW) [20], localized processing [21], [22], localized DBU [23], registration based (RB) using direction Doppler (DD) curves [24], and RB using focusing matrices [25]. Ultimately, the structure of bistatic clutter creates a need for the previous methods, and it is crucial for bistatic clutter to be properly modeled when assessing the efficacy of any clutter mitigation method.

Advantages of bistatic radar have been discussed for many decades [26], [27]. Some advantages translate to PBR. For example, the receiver susceptibility to deliberate interference is reduced due to the receiver being passive and difficult to locate. On the other hand, there are other advantages to bistatic radar that cannot be achieved for PBR because these rely on cooperative transmitters and/or waveform designs. For example, range ambiguities can be resolved by using staggered pulse repetition intervals (PRIs) [26].

The radar waveforms for PBR are generated from uncooperative systems. Therefore, the performance of PBR depends on many properties of the emitter of opportunity. Research into the performance and feasibility of PBR has been conducted for digital video broadcasting-terrestrial (DVB-T) signals [28]–[34], global system for global communications (GSM) signals [35], long term evolution (LTE) signals [36]–[38], and various others [27], [39]–[44]. As is evident, most of the waveform research exists for commercial waveforms, which have not been designed for radar applications. When a direct path exists from the transmitter to the receiver, a passive radar can conduct pulse-Doppler processing by capturing short windows of the direct path signal at constant time intervals. However, this forces the PBR to use a pulse-diverse waveform, which leads to poor clutter suppression through matched filtering [45]. The range sidelobes produced from

compression will vary with each pulse and thus cause the clutter energy to spread across Doppler [46], [47]. Therefore, it is critical to include the clutter-Doppler spreading effect when modeling passive GMTI effectiveness.

Space-time adaptive processing (STAP) is commonly implemented for GMTI. The effectiveness of STAP strongly depends on the clutter structure and statistics. For example, a large clutter discrete (LCD) can cause false alarms and missed detections because the bright specular scatterer does not follow the distributed clutter statistics. So while limited research into passive bistatic STAP exists, LCD mitigation for PBR has not been addressed. Topics for passive bistatic STAP do include the analysis and suppression of interference [6], PBR clutter mitigation techniques [48], and some proof of concepts [6], [49], [50]. Typically, though, LCD removal is found in research for monostatic radars that incorporate knowledge-aided STAP (KA-STAP) [51] where a priori knowledge is collected and examined to predict clutter statistics.

Finally, the research into GMTI via STAP and multiple transmitters becomes very scarce [52]. In [52] the clutter contributions are estimated and mitigated by means of the sparse Bayesian learning (SBL) method. Upon the completion of clutter mitigation, a target's two-dimensional velocity vector is estimated from the combination of multiple transmitters.

However, no research has been conducted into optimizing emitter selection for GMTI purposes. As will be seen, GMTI performance depends on many coupled variables for a multi-transmitter passive system. Therefore, this research develops metrics that can be used for down-selecting to an optimal transmitter based off the relative geometries. Simulated performance is analyzed across a wide search area and many two-dimensional target velocities.

1.2 Overview

This paper is organized such that Chapter 2 introduces the three dimensional geometry associated with PBR along with common post-processing methods for GMTI. Chapter 3 details the modeling of PBR for GMTI by developing the heterogeneous clutter model, defining passive STAP along with the associated pulse-diverse waveform effects. Chapter 3 will further stress the importance of modeling by analyzing the changes in expected performance that are dictated by the chosen clutter model.

Chapter 4 develops new metrics for down-selecting to an optimal transmitter when multiple exist. These metrics become inherently reliant on the chosen clutter model along with relative geometries. This chapter will conclude by analyzing the results from a large simulation.

Chapter 5 first derives detection and estimation techniques. These techniques are then applied to simulated data in order to remove a LCD. The results from the algorithm will then be showcased.

Finally, Chapter 6 will give a brief conclusion that will highlight the research contributions. These contributions all pertain to GMTI in a passive radar system. They can be further sub-categorized into the areas of clutter and waveform modeling, emitter selection metrics, and LCD removal.

Chapter 2

Foundational Theory

Some foundational understanding is required to model PBR for GMTI. In particular, the geometry incurred from separating the receiver and transmitter induces range delays that create elliptical range gates. Furthermore, unlike monostatic, the non-circular isorange contours exhibit varying SNR performance within the same range gate. These observations are derived in Section 2.1.

Since STAP is often implemented for GMTI, this adaptive filtering method is presented in Section 2.2. However, STAP is very computationally intensive and can become impractical. Therefore, a sub-optimal reduced-dimension STAP algorithm is introduced in Section 2.3 and is known as the extended factored algorithm (EFA). The EFA is used throughout the research to compare STAP performance more efficiently.

2.1 Passive Bistatic Geometry

The passive bistatic radar system is assumed to contain a multiple-channel radar receiver that collects radar echoes emanating from a non-cooperative stationary source. It is further assumed the receiver is mounted on an airborne platform in a side-looking configuration. The receiver and transmitter heights above the ground plane (x-y plane) are represented as h_R and h_T, where it is assumed that $h_R > h_T$. The angle between the receiver and transmitter is known as the elevation angle, θ_T, and is defined as negative. The bistatic baseline, L, is physical separation between the receiver and transmitter, and calculated as

$$L = \left| \frac{h_R - h_T}{\sin \theta_T} \right|. \tag{2.1}$$

The angle between the receiver and transmitter in the x-y plane is defined as the azimuth angle, ϕ_T, where 0° and 90° correspond to the x-axis and y-axis, respectively. Assuming a flat earth model and letting the receive platform be defined with global coordinates of $(0, 0, h_R)$ results in transmitter location of $(L \cos\theta_T \cos\phi_T, L \cos\theta_T \sin\phi_T, h_T)$. Refer to Figure 2.1 for a complete illustration of these coordinate parameters.

The direct paths from the receiver and transmitter to any point on the ground, $(x, y, 0)$, can be represented as range vectors notated as $\vec{R}_R$ and $\vec{R}_T$, respectively. The range from the point on the ground to either the receiver

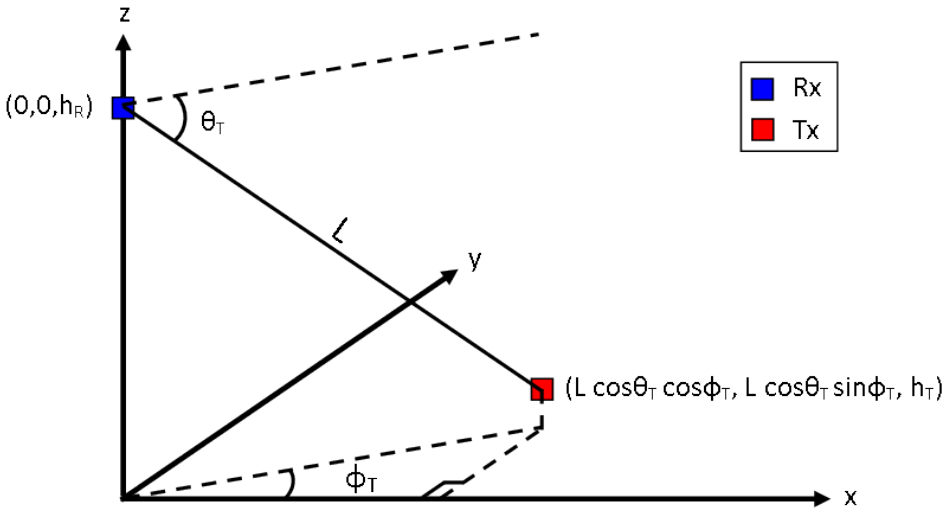

Figure 2.1: Receiver and transmitter locations in three dimensional space.

or transmitter is simply the magnitude, R_R and R_T, of the respective range vectors. The plane containing both range vectors is commonly known as the bistatic plane. The angle between in the range vectors in the bistatic plane is known as the bistatic angle, β, and is easily calculated as

$$\beta = \cos^{-1}\left(\frac{\vec{R}_R \cdot \vec{R}_T}{\left|\vec{R}_R\right|\left|\vec{R}_T\right|}\right) = \cos^{-1}\left(\frac{\vec{R}_R \cdot \vec{R}_T}{R_R R_T}\right). \tag{2.2}$$

Finally, the total distance traveled from the transmitter to a point on the ground and back to the receiver, is known as the bistatic range, R_B, such that

$$R_B = R_T + R_R. \tag{2.3}$$

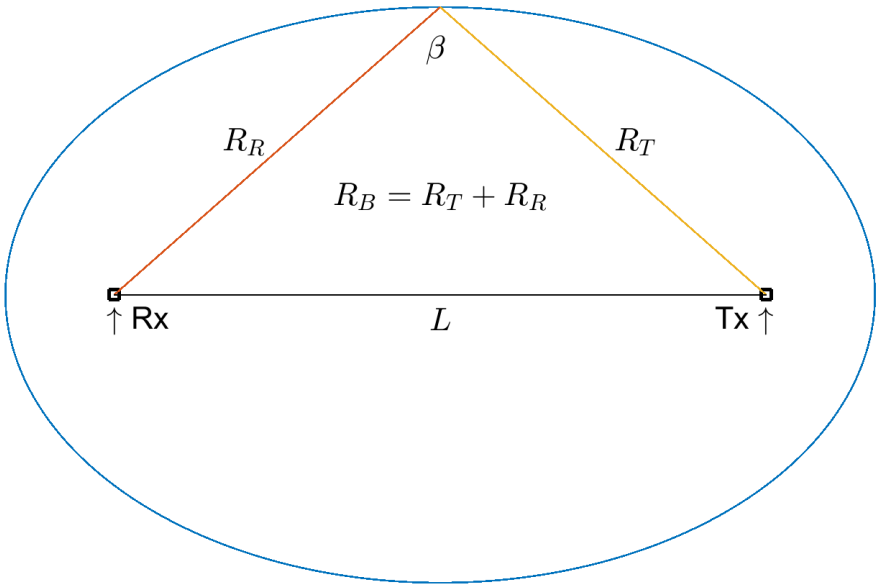

Figure 2.2: Bistatic range and angle within the bistatic plane.

2.1.1 Isorange Contours

Isorange contours represent a constant propagation delay (e.g. bistatic range) from all the ground scatterers that lie on the contour. In the bistatic plane, an ellipse represents a constant bistatic range as seen in Figure 2.2. When extending to three-dimensional space, the surface of revolution known as a prolate spheroid defines a constant bistatic range. Revolving the ellipse from the bistatic plane about its major axis generates the prolate spheroid. Isorange contours are then found from the intersection of the prolate spheroid and the ground plane or the global x-y plane.

To solve for this intersection, the local coordinate axes containing the surface must have one axis that is parallel with its respective global axis [53]. Therefore, consider a transmitter with an azimuth angle,ϕ_T, of zero.

This yields global positions of $(0, 0, h_R)$ and $(L\cos\theta_T, 0, h_T)$ for the receiver and transmitter, respectively. Then let the receiver and transmitter represent the foci of the prolate spheroid with local positions of $(0, 0, 0)$ and $(L, 0, 0)$, respectively. This setup causes the local coordinate system to be translated and rotated with respect to the global system and is depicted in Figure 2.3.

A prolate spheroid with the major axis along the x-axis is given in local coordinates as

$$\frac{(x' - x_0)^2}{a^2} + \frac{(y' - y_0)^2}{b^2} + \frac{(z' - z_0)^2}{b^2} = 1, \tag{2.4}$$

where (x_0, y_0, z_0) is the center of the 3D surface and a and b are the semi-major and semi-minor axes respectively. Note that the repetition of b in (2.4) is what forces the ellipsoid to become a prolate spheroid (football shape). As an example, if $a < b$ then (2.4) generates an oblate spheroid (Earth shape), whereas if $a = b$ then a sphere is produced. Using the previous defined receiver and transmitter locations, the center of the spheroid must equal $(L/2, 0, 0)$. Then, for a point on the ground, $P(x, y, 0)$, the local coordinates can be represented as

$$\begin{aligned} x' &= \left(x - h_R \tan\theta_T\right)\cos\theta_T \\ &= x\cos\theta_T - h_R\sin\theta_T \qquad (2.5) \\ y' &= y \qquad (2.6) \end{aligned}$$

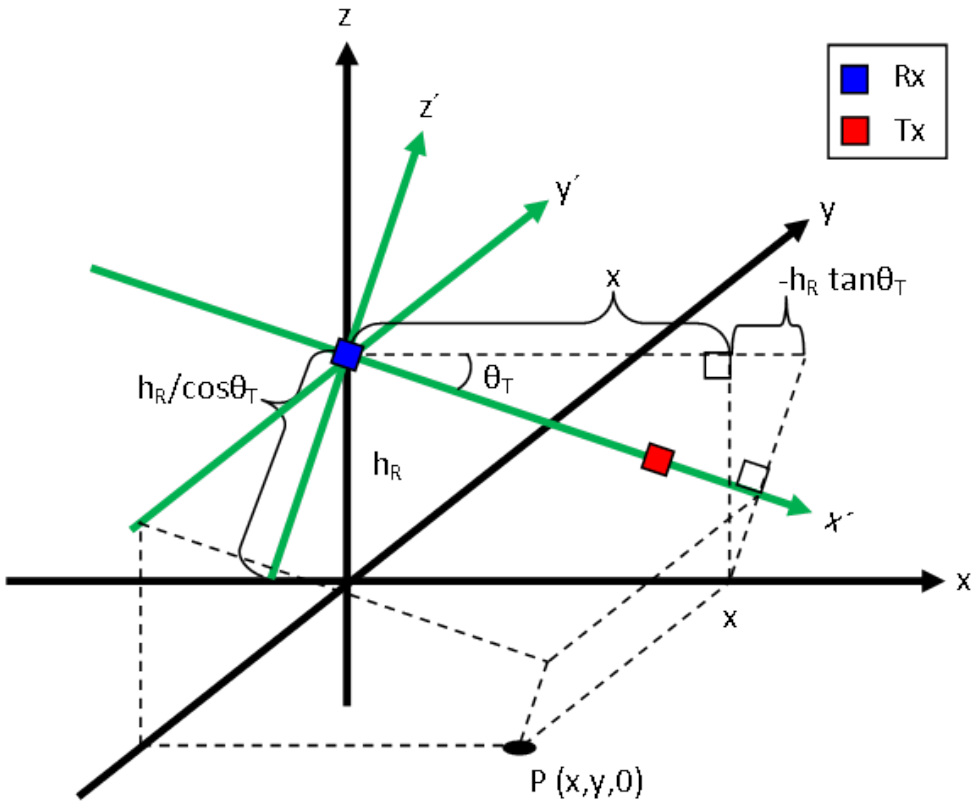

Figure 2.3: Prolate spheroid local coordinate system configure on the global coordinate system.

$$\begin{aligned} z' &= \frac{-h_R}{\cos\theta_T} - (x - h_R \tan\theta_T)\sin\theta_T \\ &= -x\sin\theta_T - h_R\left(\frac{1}{\cos\theta_T} - \frac{\sin^2\theta_T}{\cos\theta_T}\right) \\ &= -x\sin\theta_T - h_R\cos\theta_T, \end{aligned} \tag{2.7}$$

where the three equations above are based off the definition of θ_T as negative. Now substituting the change of variable equations into (2.4) yields

$$\frac{(x\cos\theta_T - h_R\sin\theta_T - {}^{L}/_{2})^2}{a^2} + \frac{y^2}{b^2} + \frac{(-x\sin\theta_T - h_R\cos\theta_T)^2}{b^2} = 1$$

$$\frac{b^2}{a^2}\left(x^2\cos^2\theta_T + h_R^2\sin^2\theta_T + \frac{L^2}{4} - xh_R\sin 2\theta_T - xL\cos\theta_T + h_RL\sin\theta_T\right)$$

$$+y^2 + x^2\sin^2\theta_T + xh_R\sin 2\theta_T + h_R^2\cos^2\theta_T = b^2 \tag{2.8}$$

$$x^2\left(\frac{b^2}{a^2}\cos^2\theta_T + \sin^2\theta_T\right) - 2x\left[\left(\frac{b^2}{a^2} - 1\right)\frac{h_R}{2}\sin 2\theta_T + \frac{b^2}{2a^2}L\cos\theta_T\right] + y^2 =$$

$$b^2 - \frac{b^2}{a^2}\left(h_R^2\sin^2\theta_T + \frac{L^2}{4} + h_RL\sin\theta_T\right) - h_R^2\cos^2\theta_T.$$

Let γ, α and ζ be

$$\gamma = \frac{b^2}{a^2}\cos^2\theta_T + \sin^2\theta_T, \tag{2.9}$$

$$\alpha = \left(\frac{b^2}{a^2} - 1\right)\frac{h_R}{2}\sin 2\theta_T + \frac{b^2}{2a^2}L\cos\theta_T, \tag{2.10}$$

and

$$\zeta = b^2 - \frac{b^2}{a^2}\left(h_R^2\sin^2\theta_T + \frac{L^2}{4} + h_RL\sin\theta_T\right) - h_R^2\cos^2\theta_T, \tag{2.11}$$

such that (2.8) becomes

$$\begin{aligned}
\gamma x^2 - 2\alpha x + y^2 &= \zeta \\
x^2 - 2\frac{\alpha}{\gamma}x + \left(\frac{\alpha}{\gamma}\right)^2 + \frac{1}{\gamma}y^2 &= \frac{\zeta}{\gamma} + \left(\frac{\alpha}{\gamma}\right)^2 \\
\frac{\left(x - \frac{\alpha}{\gamma}\right)^2}{\frac{\zeta}{\gamma} + \frac{\alpha^2}{\gamma^2}} + \frac{y^2}{\zeta + \frac{\alpha^2}{\gamma}} &= 1. \qquad (2.12)
\end{aligned}$$

Last, realizing $a = {}^{R_B}/_2$ and $b = \sqrt{R_B^2 - L^2}/2$ allows γ, α and ζ to be written in terms of bistatic radar parameters

$$\begin{aligned}
\alpha &= \frac{\left(R_B^2 - L^2\right) L}{2R_B^2}\cos\theta_T - \frac{L^2 h_R}{2R_B^2}\sin 2\theta_T \\
\gamma &= 1 - \frac{L^2}{R_B^2}\cos^2\theta_T \\
\zeta &= \frac{R_B^2 - L^2}{4}.
\end{aligned}$$

Again, (2.12) is only valid for $h_R > h_T$ and a transmitter elevation angle, θ_T, defined as negative. Then, letting R_B vary incrementally by the waveform's delay resolution, the resolved elliptical isorange contours on the ground are calculated. These contours are depicted in Figure 2.4. The parametric equations can be defined by rewriting (2.12) as

$$\frac{\left(x - \frac{\alpha}{\gamma}\right)^2}{\frac{\zeta}{\gamma} + \frac{\alpha^2}{\gamma^2}} + \frac{y^2}{\zeta + \frac{\alpha^2}{\gamma}} = \cos^2\omega + \sin^2\omega, \qquad (2.13)$$

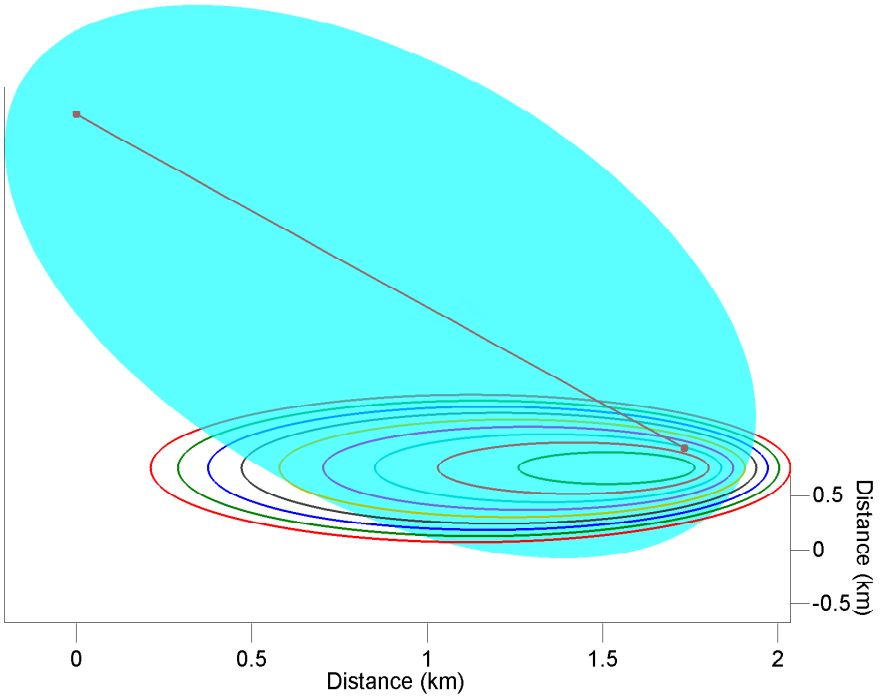

Figure 2.4: Isorange contours found through the intersection of the ground plane and a prolate spheroid with constant R_B.

and setting the x and y terms equal to the $\cos^2\omega$ and $\sin^2\omega$ respectively. After solving for x and y, the parametric equations become

$$x = \sqrt{\cos^2\omega\left(\frac{\zeta}{\gamma}+\frac{\alpha^2}{\gamma^2}\right)}+\frac{\alpha}{\gamma}, \tag{2.14}$$

and

$$y = \sqrt{\sin^2\omega\left(\zeta+\frac{\alpha^2}{\gamma}\right)}, \tag{2.15}$$

where the parametric parameter, $\omega \in [0, 2\pi)$, defines one trip around an isorange contour. Finally, the isorange contours for any generic transmitter with global coordinates of $(L\cos\theta_T\cos\phi_T, L\cos\theta_T\sin\phi_T, h_T)$, can be found

by rotating the parametric equations for the x and y coordinates by ϕ_T,

$$\begin{aligned} x &= \left(\sqrt{\cos^2\omega\left(\frac{\zeta}{\gamma}+\frac{\alpha^2}{\gamma^2}\right)}+\frac{\alpha}{\gamma}\right)\cos\phi_T \\ &\quad -\left(\sqrt{\sin^2\omega\left(\zeta+\frac{\alpha^2}{\gamma}\right)}\right)\sin\phi_T \qquad (2.16) \\ y &= \left(\sqrt{\cos^2\omega\left(\frac{\zeta}{\gamma}+\frac{\alpha^2}{\gamma^2}\right)}+\frac{\alpha}{\gamma}\right)\sin\phi_T \\ &\quad +\left(\sqrt{\sin^2\omega\left(\zeta+\frac{\alpha^2}{\gamma}\right)}\right)\cos\phi_T. \qquad (2.17) \end{aligned}$$

2.1.2 Bistatic Range Performance

The bistatic signal-to-noise ratio (SNR) is defined as [54]

$$SNR = \frac{P_T G_T G_R \lambda^2 \sigma_B F_T^2 F_R^2}{(4\pi)^3 k T_s B_n L_T L_R R_T^2 R_R^2} \qquad (2.18)$$

where

$$P_T = \text{Transmit power}$$

$$G_T = \text{Transmitter antenna gain and pattern}$$

$$G_R = \text{Receiver antenna gain and pattern}$$

$$\lambda = \text{Waveform wavelength}$$

$$\sigma_B = \text{Target bistatic RCS}$$

$$F_T = \text{Pattern propagation factor from Tx to target}$$

$$F_R = \text{Pattern propagation factor from Rx to target}$$

$$k = \text{Boltzmann's constant}$$

$$T_s = \text{Receiver system temperature}$$

$$B_n = \text{Receiver noise bandwidth}$$

$$L_T = \text{Transmitter system losses}$$

$$L_R = \text{Receiver system losses}$$

$$R_T = \text{Range from transmitter to target}$$

$$R_T = \text{Range from receiver to target.}$$

To understand how performance varies with bistatic range in the bistatic plane, let all non range-dependent variables in (2.18) be represented as the

constant, C, such that

$$SNR = \frac{C}{R_T^2 R_R^2}. \tag{2.19}$$

Then after some manipulation, (2.19) can represent a specific quartic polynomial known as a Cassini oval [54].

Giovanni Domenico Cassini was an Italian astronomer and professor during the seventeenth-century. In 1669, King Louis XIV invited Cassini to Paris where he eventually became the founding director of the Paris Observatory [55]. Cassini made many contributions to astronomy ranging from the discovery of Saturn's moons and rings to how to make longitudinal calculations for navigators and mapmakers [55]. During his time, Cassini rejected Kepler's theory that planetary motion followed elliptical orbits. Instead Cassini proposed what has been called the "Cassinoïde", ellipse of Cassini, and Cassini oval [56]. Unlike an ellipse that maintains a constant sum of the two distances from the foci to a point on the ellipse, a Cassini oval consists of a set of points where the product of the distances from the foci to any point on the oval is constant [57]. So while Cassini ovals may not accurately represent planetary motion, they can represent constant SNR (thermal noise only) for the bistatic radar range equation. Through the study of these ovals, a basic understanding can be attained for how bistatic geometry affects SNR performance.

First, let us define a two dimensional local coordinate system within the bistatic plane where the receiver lies at the origin. Then, assume the transmitter is located at $(L, 0)$. These definitions cause the range variables in (2.19) to be equal to

$$\begin{aligned} R_R &= \sqrt{x^2 + y^2} \\ R_T &= \sqrt{(x-L)^2 + y^2}, \end{aligned} \tag{2.20}$$

Then substituting (2.20) into (2.19) gives the following expression in Cartesian coordinates

$$\begin{aligned} \frac{C}{SNR} &= \left(x^2 + y^2\right)\left((x-L)^2 + y^2\right) \\ &= \left(x^2 + y^2\right)\left(x^2 + y^2 + L^2 - 2xL\right) \\ &= \left(x^2 + y^2\right)^2 + L^2\left(x^2 + y^2\right) - 2xL\left(x^2 + y^2\right). \end{aligned} \tag{2.21}$$

Next, through the use of polar coordinate transformations where $x = r\cos\theta$ and $r = \sqrt{x^2 + y^2}$, (2.21) becomes

$$r^4 + L^2 r^2 - 2r^3 L\cos\theta = \frac{C}{SNR}. \tag{2.22}$$

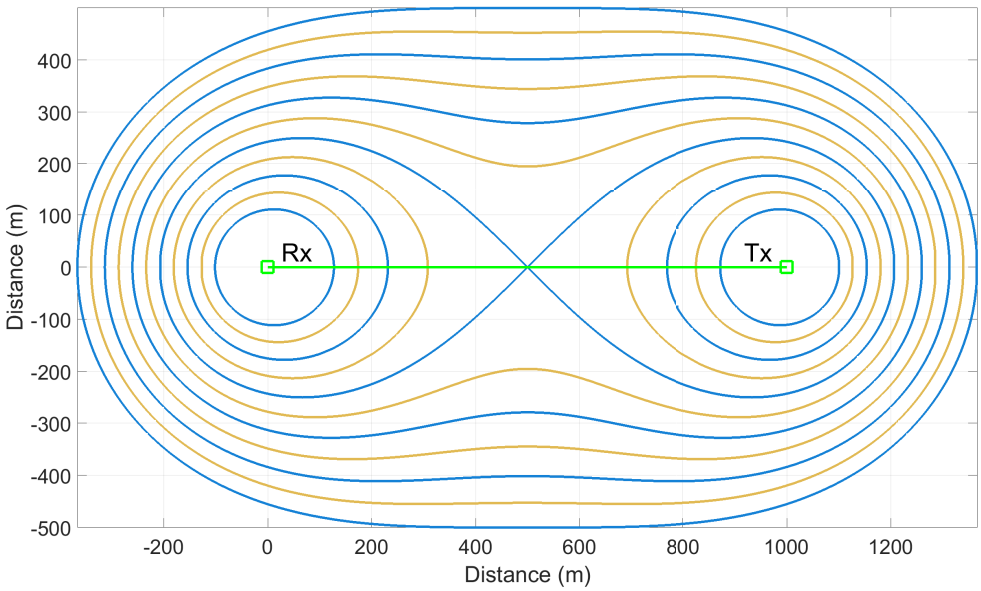

Figure 2.5: Cassini ovals that represent iso-SNR contours in the bistatic plane.

Immediately noticeable is that SNR is inversely proportional to the polar coordinate r^*. Therefore, as SNR decreases, the size of the Cassini oval increases.

Figure 2.5 depicts various constant SNR curves that can be separated into four categories: two separate closed curves, a figure eight (known as the Lemniscate of Bernoulli), a single closed curve with indentions, and a convex closed curve [58]. These categories depend on C/SNR from (2.22) in comparison to the bistatic baseline separation, L, and defined as follows,

*Radius r is the distance from the center of the oval at $(L/2, 0)$ to a point on the curve.

$$
\begin{aligned}
0 < \frac{C}{SNR} < \frac{L^4}{16}, &\quad \text{Two separate closed curves,} \\
\frac{C}{SNR} = \frac{L^4}{16}, &\quad \text{Figure eight,} \\
\frac{L^4}{16} < \frac{C}{SNR} < \frac{L^4}{4}, &\quad \text{Single closed curve with indentions,} \\
\frac{C}{SNR} \geq \frac{L^4}{4}, &\quad \text{Convex closed curve.}
\end{aligned}
$$

All four categories can be seen in Figure 2.5 where the largest Cassini oval is the only closed convex curve and calculated for when $C/SNR = L^4/4$.

The Cassini curves given in (2.22) are only defined in the bistatic plane as shown in Figure 2.5. In order to understand constant SNR for ground moving targets, the Cassini ovals must be revolved around the bistatic baseline and intersected with the ground plane (global x-y plane). Figure 2.6 illustrates a variety of intersected iso-SNR curves when the receiver is located at $(0, 0, 1000\text{ m})$ and the transmitter at $(940\text{ m}, 0, 60\text{ m})$.

Next, Figure 2.7 compares isorange contours with constant SNR curves that are spaced at intervals of 3 dB for the same receiver and transmitter locations as in Figure 2.6. It can be seen in Figure 2.7 that isorange contours near the transmitter experience greater SNR dynamic range while increasing bistatic range decreases the fluctuation of SNR around the isorange contour. As an example, the smallest bistatic range in Figure 2.7 can experience greater than 9 dB of SNR dynamic range while the largest bistatic range contour varies closer to 3 dB.

Finally, another parameter to assist in understanding bistatic range performance is the isorange contour eccentricity. The eccentricity, e, of each isorange contour is defined as $e = c/a$ where c is the distance from the center of an ellipse to a focus and a is the semi-major axis. From the properties of an ellipse, c is equal to $\sqrt{a^2 - b^2}$ where b is the semi-minor axis. Referring

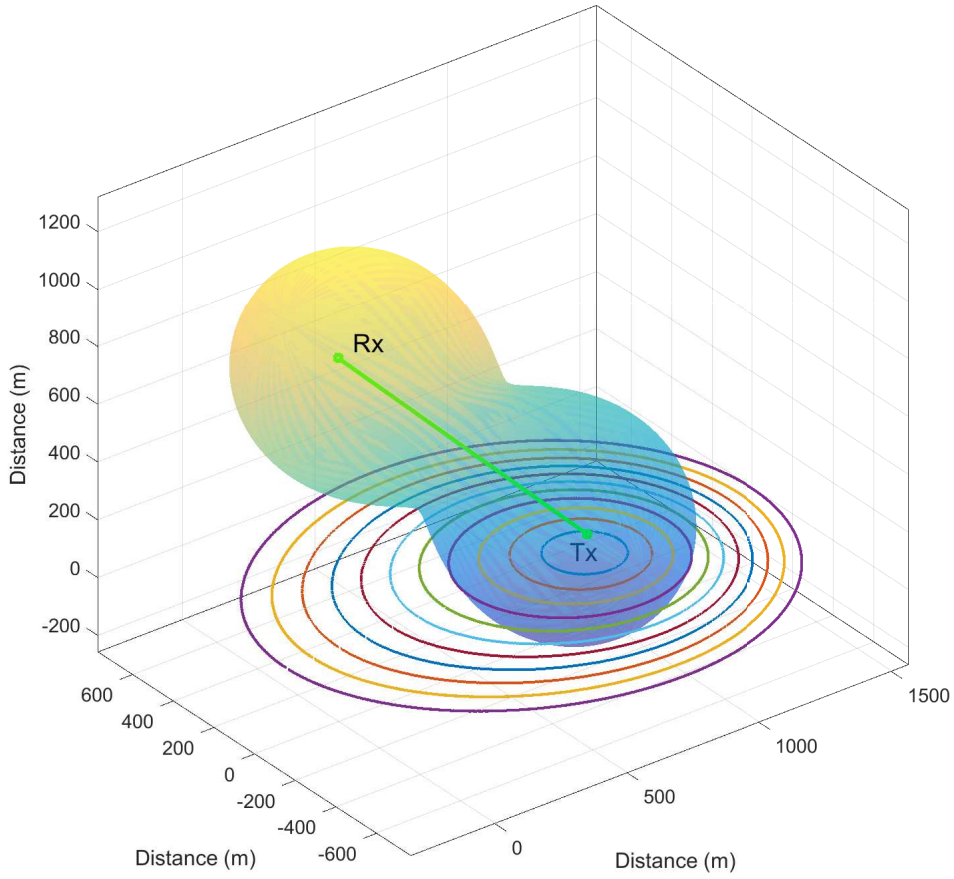

Figure 2.6: Constant SNR curves are found by revolving Cassini ovals around the baseline and finding the intersection with the ground plane. The SNR curves shown are spaced every 3 dB.

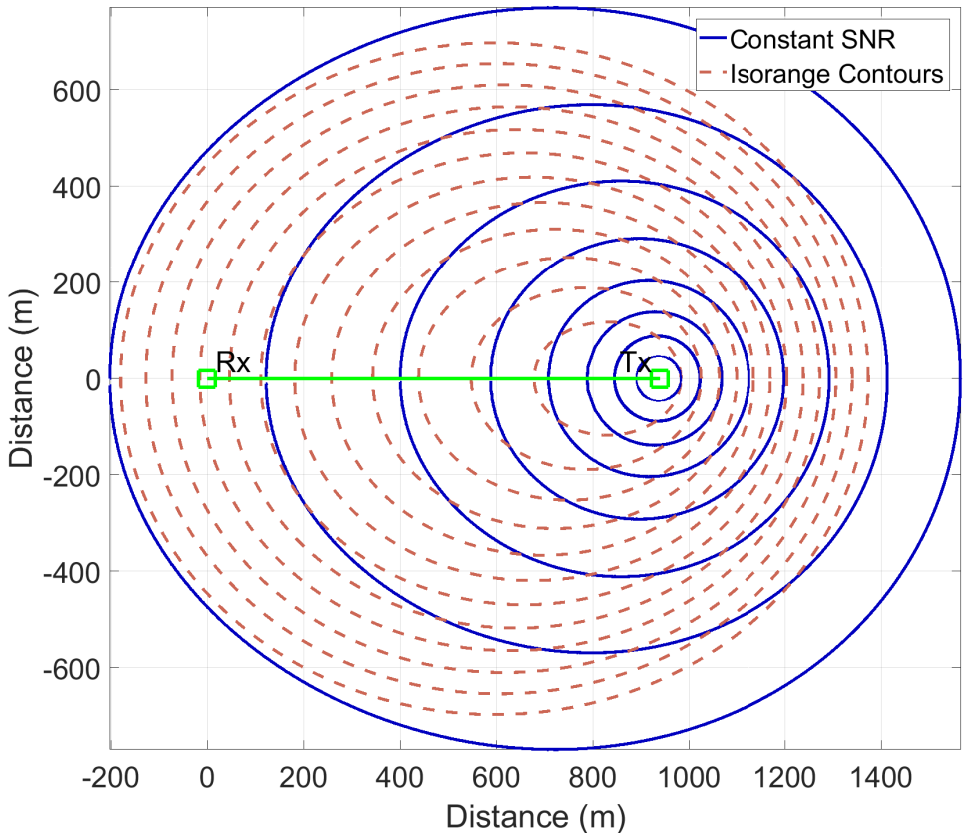

Figure 2.7: A comparison of isorange contours and constant SNR curves. Smaller R_B experience a larger dynamic range of SNR when compared to less eccentric isorange contours.

to (2.12), it is seen that a and b are defined as

$$a = \sqrt{\frac{\zeta}{\gamma} + \frac{\alpha^2}{\gamma^2}} \tag{2.23}$$

$$b = \sqrt{\zeta + \frac{\alpha^2}{\gamma}} \tag{2.24}$$

Therefore, looking at the eccentricity of an isorange contour as bistatic range, R_B, approaches infinity gives

$$\begin{aligned}
\lim_{R_B\to\infty} e &= \lim_{R_B\to\infty} \frac{c}{a} \\
&= \lim_{R_B\to\infty} \frac{\sqrt{\frac{\zeta}{\gamma}+\frac{\alpha^2}{\gamma^2}-\zeta-\frac{\alpha^2}{\gamma}}}{\sqrt{\frac{\zeta}{\gamma}+\frac{\alpha^2}{\gamma^2}}} \\
&= \frac{\sqrt{\frac{\infty}{1}+\frac{\left(\frac{L\cos\theta}{2}\right)^2}{1^2}-\infty-\frac{\left(\frac{L\cos\theta}{2}\right)^2}{1}}}{\sqrt{\frac{\infty}{1}+\frac{\left(\frac{L\cos\theta}{2}\right)^2}{1^2}}} \\
&= \frac{\sqrt{\left(\frac{L\cos\theta}{2}\right)^2+\left(\frac{L\cos\theta}{2}\right)^2-\left(\frac{L\cos\theta}{2}\right)^2}}{\sqrt{\infty+\left(\frac{L\cos\theta}{2}\right)^2}} \\
&= \frac{\left(\frac{L\cos\theta}{2}\right)}{\infty} \\
&= 0.
\end{aligned} \tag{2.25}$$

The result from (2.25) states that the isorange contour becomes circular in the limit. If the range ring becomes circular in the limit, then $R_R = R_T$ and the Cassini oval becomes circular in the limit. Therefore, as range increases performance mimics monostatic radar in nature because the bistatic geometry is less influential.

2.2 Space-Time Adaptive Processing Introduction

When a multi-channel radar is mounted to an aerospace platform, the returned ground clutter extends in both range and angle and exhibits induced Doppler spread from the platform motion [59]. Improved target detection can be attained through spatial and temporal diversity otherwise known as degrees of freedom (DoF) [60]. Steering vector notation is often used to represent the change in phase of the received radar signal over space and time. If the coherent processing interval (CPI) is M pulses, then the n^{th} antenna channel measures complex baseband voltages from a point source as [61]

$$\begin{aligned}\mathbf{x_{t,k}}(n) = \alpha_{s,k}(n)\big[1 \quad \exp(j\bar{f}_d) \quad \exp(j2\bar{f}_d)\cdots \\ \exp(j(M-2)\bar{f}_d) \quad \exp(j(M-1)\bar{f}_d)\big]^{\mathrm{T}},\end{aligned} \tag{2.26}$$

where T is the transpose operator, $\alpha_{s,k}(n)$ represents a random scalar the n^{th} channel measures at the k^{th} rangebin, $\mathbf{x_{t,k}}(n)$ is the temporal snapshot for the n^{th} channel, and $\bar{f}_d$ is the normalized Doppler frequency. The column vector in (2.26) is defined as the temporal steering vector, $\mathbf{s_t}(\bar{f}_d)$ [61],

$$\begin{aligned}\mathbf{s_t}(\bar{f}_d) = \big[1 \quad \exp(j\bar{f}_d) \quad \exp(j2\bar{f}_d)\cdots \\ \exp(j(M-2)\bar{f}_d) \quad \exp(j(M-1)\bar{f}_d)\big]^{\mathrm{T}}.\end{aligned} \tag{2.27}$$

Furthermore, the measured complex baseband voltage of the m^{th} pulse across N channels from a point source is given as [61],

$$\mathbf{x_{s,k}}(m) = \alpha_{t,k}(m)\big[1 \quad \exp(j\vartheta) \quad \exp(j2\vartheta)\cdots \\ \exp(j(N-2)\vartheta) \quad \exp(j(N-1)\vartheta)\big]^{\mathrm{T}}, \tag{2.28}$$

where $\alpha_{t,k}(m)$ represents a measured random scalar from the m^{th} pulse at the k^{th} rangebin, $\mathbf{x_{s,k}}(m)$ is the spatial snapshot for the m^{th} pulse, and ϑ is the normalized spatial frequency. Thus the spatial steering vector, $\mathbf{s_s}(\vartheta)$, is defined as

$$\mathbf{s_s}(\vartheta) = \big[1 \quad \exp(j\vartheta) \quad \exp(j2\vartheta)\cdots \\ \exp(j(N-2)\vartheta) \quad \exp(j(N-1)\vartheta)\big]^{\mathrm{T}}. \tag{2.29}$$

It is now possible to define the space-time steering vector, $\mathbf{s}(\vartheta, \bar{f}_d)$, as

$$\begin{aligned}\mathbf{s}(\vartheta, \bar{f}_d) &= \mathbf{s_t}(\bar{f}_d) \otimes \mathbf{s_s}(\vartheta) \\ &= \big[1\mathbf{s_t}^{\mathrm{T}} \quad e^{j\vartheta}\mathbf{s_t}^{\mathrm{T}} \quad e^{j2\vartheta}\mathbf{s_t}^{\mathrm{T}}\cdots \\ &\quad e^{j(N-2)\vartheta}\mathbf{s_t}^{\mathrm{T}} \quad e^{(j(N-1)\vartheta}\mathbf{s_t}^{\mathrm{T}}\big]^{\mathrm{T}},\end{aligned} \tag{2.30}$$

where $\otimes$ denotes the kronecker product. When a normalized spatial and Doppler frequency is hypothesized, $(\hat{\vartheta}, \hat{\bar{f}}_d)$, the space-time steering vector

represents a matched filter ($\mathbf{w_k}$)

$$\mathbf{w_k} = \mu \mathbf{s}(\hat{\vartheta}, \hat{\bar{f}}_d) \tag{2.31}$$

and thus maximizes the signal power relative to white Gaussian noise for arbitrary scalar μ [61]. The goal in STAP; however, is to maximize signal to interference-plus-noise ratio (SINR).

The received signal, $\mathbf{x_k}$, is characterized by two models,

$$\begin{aligned} H_0 : \quad & \mathbf{x_k} = \mathbf{c_k} + \mathbf{n_k} \\ H_1 : \quad & \mathbf{x_k} = \mathbf{t_k} + \mathbf{c_k} + \mathbf{n_k}, \end{aligned} \tag{2.32}$$

where H_0 is commonly known as the null hypothesis and the H_1 hypothesis contains a target. The elements $\mathbf{t_k}$, $\mathbf{c_k}$, $\mathbf{n_k}$ represent the contributions from a target, clutter, and receiver noise respectively. Therefore, SINR is defined by [61]

$$\begin{aligned} \text{SINR} &= \frac{E\left[\mathbf{w_k}^{\mathrm{H}} \mathbf{t_k} \mathbf{t_k}^{\mathrm{H}} \mathbf{w_k}\right]}{E\left[\mathbf{w_k}^{\mathrm{H}} \mathbf{x_{k|H_0}} \mathbf{x_{k|H_0}}^{\mathrm{H}} \mathbf{w_k}\right]} \\ &= \frac{\sigma_s^2 \left|\mathbf{w_k}^{\mathrm{H}} \mathbf{s}(\vartheta, \bar{f}_d)\right|^2}{\mathbf{w_k}^{\mathrm{H}} \mathbf{R_k} \mathbf{w_k}}, \end{aligned} \tag{2.33}$$

where H denotes a Hermitian or conjugate transpose. It is assumed $\mathbf{t_k} = \alpha_{tgt}\mathbf{s}(\vartheta_{tgt}, \bar{f}_{d,tgt})$ and α_{tgt}, ϑ_{tgt}, and $\bar{f}_{d,tgt}$ are the target's corresponding complex RMS voltage, spatial, and Doppler frequencies. Furthermore, it is assumed the data for the null case, $\mathbf{x_{k|H_0}}$, is colored Gaussian noise where $\mathbf{x_{k|H_0}} \sim CN(0, \mathbf{R_k})$ and $\mathbf{R_k} = \mathbf{x_{k|H_0}}\mathbf{x_{k|H_0}}^{\mathrm{H}}$ is the interference covariance matrix at range bin k. Finally, σ_s^2 represents the signal power at a single channel and single pulse given as $\sigma_s^2 = E[|\alpha_{tgt}|^2]$.

The optimal filter that maximizes SINR is

$$\mathbf{w_k} = \beta \mathbf{R_k}^{-1}\mathbf{s}, \tag{2.34}$$

where β represents an arbitrary scalar that does not alter the SINR output [62], [63]. Also note the notation for the steering vector's dependency on spatial and Doppler frequencies is dropped for convenience. Substituting (2.34) into (2.33) yields the optimal SINR for the clairvoyant case as

$$\begin{aligned} \mathrm{SINR_{opt}} &= \frac{\sigma_s^2 \beta^2 \left|\mathbf{s}^{\mathrm{H}}\mathbf{R_k}^{-1}\mathbf{s}\right|^2}{\beta^2 \mathbf{s}^{\mathrm{H}}\mathbf{R_k}^{-1}\mathbf{R_k}\mathbf{R_k}^{-1}\mathbf{s}} \\ &= \frac{\sigma_s^2 \left|\mathbf{s}^{\mathrm{H}}\mathbf{R_k}^{-1}\mathbf{s}\right|^2}{\mathbf{s}^{\mathrm{H}}\mathbf{R_k}^{-1}\mathbf{s}} \\ &= \sigma_s^2 \left|\mathbf{s}^{\mathrm{H}}\mathbf{R_k}^{-1}\mathbf{s}\right|. \end{aligned} \tag{2.35}$$

SINR can be calculated over a two-dimensional angle[†]/Doppler space. However, a spatial frequency/angle is usually held constant and referred to as a spatial cut. SINR is then calculated over $-0.5 \leq \bar{f}_d < 0.5$. As an example, a clairvoyant SINR curve is plotted in Figure 2.8 at a spatial cut of $\vartheta = 0$. Figure 2.8 also labels some common nomenclatures used in STAP that include the noise and clutter limited regions[‡] and the clutter notch. At a spatial cut of zero the Doppler frequency of the clutter is also zero, which is what produces the sharp drop in loss that is known as the clutter notch. Different spatial cuts will cause induced Doppler shifts on stationary clutter and result in the clutter notch shifting to the appropriate Doppler frequency. Finally, the extent of the clutter notch is directly related to the clutter strength. Larger clutter returns cause deeper notches while weak clutter results in more shallow notches.

The interference covariance matrix for the clairvoyant case, $\mathbf{R_k}$, is not known in practice and must therefore be estimated. A common estimation technique is termed the sample matrix inversion (SMI) [64] where $\hat{\mathbf{R}}_\mathbf{k}$ is

$$\hat{\mathbf{R}}_\mathbf{k} = \frac{1}{P} \sum_{p=1}^{P} \mathbf{x_p} \mathbf{x_p}^{\mathrm{H}}. \tag{2.36}$$

[†]The relationship between angle and spatial frequency is defined in Section 3.2.1.
[‡]These terms have also been coined as exo-clutter and endo-clutter regions.

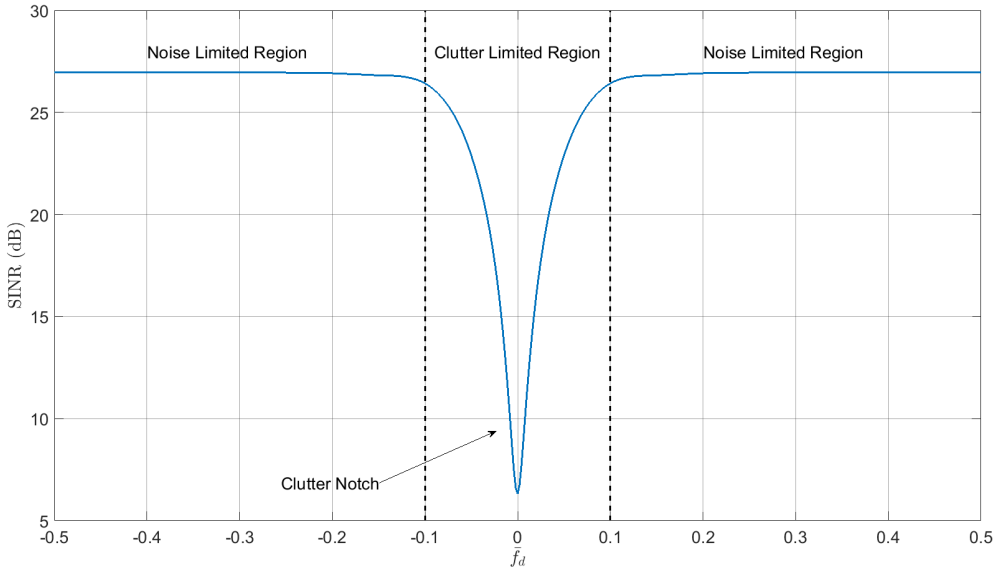

Figure 2.8: Example of a SINR curve with nomenclature labeled.

The data set $\{\mathbf{x_p}, p \in [1, P]\}$ are from range bins outside the range bin/cell under test (CUT) and commonly known as the secondary or training data [60]. If the training data are range independent and identically distributed, then the so-called RMB rule (named after inventors) states $P \approx 2NM$ will yield an average performance loss of 3 dB [63].

With $\hat{\mathbf{R}}_\mathbf{k}$ defined, the adaptive filter becomes

$$\hat{\mathbf{w}}_\mathbf{k} = \beta \hat{\mathbf{R}}_\mathbf{k}^{-1} \mathbf{s}. \tag{2.37}$$

While β is arbitrary, certain definitions of β can be be more beneficial for target detection. As an example, if β is

$$\beta = \frac{1}{\sqrt{\mathbf{s}^{\mathrm{H}}\hat{\mathbf{R}}_{\mathbf{k}}^{-1}\mathbf{s}}}, \tag{2.38}$$

then the adaptive matched filter (AMF) test statistic that is defined as

$$\begin{aligned} \varkappa &= \left|\hat{\mathbf{w}}_{\mathbf{k}}^{\mathrm{H}}\mathbf{x}_{\mathbf{k}}\right|^2 \\ &= \frac{\left|\mathbf{s}^{\mathrm{H}}\hat{\mathbf{R}}_{\mathbf{k}}^{-1}\mathbf{x}_{\mathbf{k}}\right|^2}{\mathbf{s}^{\mathrm{H}}\hat{\mathbf{R}}_{\mathbf{k}}^{-1}\mathbf{s}}, \end{aligned} \tag{2.39}$$

will display constant false alarm rate (CFAR) properties [65]. However, AMF is not the only test statistic. Others extensions of SMI that also exhibit CFAR properties include Kelly's generalized likelihood ratio test (GLRT) [66] and Kraut's adaptive cosine estimator (ACE) [67].

2.3 Extended Factor Algorithm

The extended factor algorithm (EFA) is a sub-optimal reduced dimension STAP algorithm. Common problems with STAP include the large computational costs and access to training data that are representative of the CUT. Therefore, reduced dimension algorithms decrease the STAP degrees

of freedom (NM) in order to alleviate both the computational complexity and required number of training cells, P.

In particular, EFA apodizes the slow-time data through the use of temporal weighting functions (e.g. Hanning, Hamming, etc.) in conjunction with discrete Fourier transformation. Since the frequency-domain data decorrelates at a faster rate [68], the number of pulses, M, can be replaced with a smaller number of Doppler bins. As an example, if one adjacent Doppler bin is chosen, then the Doppler degrees of freedom reduces to 3 and $P \approx 2N(3) = 6N$. The computation can be even further reduced due to the fact that the matched apodized Doppler weight vector can be pre-calculated since it is shift-invariant in the frequency domain.

The EFA will be used in later chapters to evaluate SINR performance. In particular, Chapter 3 compares SINR performance across algorithms, PBR clutter modeling, and waveform effects. Chapter 4 incorporates the modeling from Chapter 3 and compares optimal SINR across emitters. Finally, Chapter 5 illustrates the SINR performances for EFA and full dimension STAP for the LCDR algorithm.

Chapter 3

Passive STAP Modeling

Important factors in modeling a passive STAP radar system are the strength of the distributed clutter in angle-Doppler space and the performance effects associated with an uncooperative waveform. Section 3.1 introduces how to model the strength of clutter over all clutter angles while Section 3.2 defines where in angle-Doppler space the clutter strength resides. Then Section 3.3 derives the performance impact to STAP that is caused by a non-ideal radar waveform. Last, Section 3.4 compares the SINR results of the newly developed in-plane out-of-plane (IPOP) model from Section 3.1 with two different bistatic clutter models found in literature. These two previously developed clutter models are introduced in Section 3.4 and are known as the extended constant gamma (ECG) model and the Aviation and Missile Command (AMCOM) model.

3.1 Heterogeneous Clutter Modeling

Classifications of clutter can include homogeneous, heterogeneous, and range-dependent. Homogeneous and heterogeneous clutter differ in that the clutter RCS statistics over area are preserved for homogeneous and vary for heterogeneous. When the clutter's angle-Doppler power spectrum varies over range, then range-dependent clutter is obtained. Angle-Doppler power spectrum variation in range is a by-product of a bistatic geometry where the transmitter and receiver are geographically separated. The focus in this research is on heterogeneous, range-dependent clutter where the heterogeneity is by in-plane and out-of-plane clutter scattering properties [12]. These scattering properties will be introduced in the following sections.

3.1.1 Clutter Defined

At the k^{th} range bin, the clutter contributions, $\mathbf{c_k}$ are attributed to the received voltage response from scatterers within the k^{th} range bin and any ambiguous range bins [61] and written as

$$\mathbf{c_k} = \sum_{j=1}^{Na} \int_0^{2\pi} \alpha\big(\vartheta_j(\omega), \bar{f}_j(\omega)\big)\mathbf{s}\big(\vartheta_j(\omega), \bar{f}_j(\omega)\big)\mathrm{d}\omega, \tag{3.1}$$

where N_a is the number of ambiguous range bins, α is the random reflection coefficient at normalized spatial and Doppler frequencies, which are dependent on the parametric parameter, ω, of the isorange contour of interest.

This continuous sum of voltage responses around isorange contours can be discretized with the use of clutter patches that are depicted in Figure 3.1. Then $\mathbf{c_k}$ is approximated as [59]

$$\mathbf{c_k} = \sum_{j=1}^{Na} \sum_{i=1}^{Nc} \alpha_{ijk} \mathbf{s}(\vartheta_{ijk}, \bar{f}_{ijk}), \tag{3.2}$$

where N_c is the number of clutter patches within a range bin, and α_{ijk}, ϑ_{ijk}, and $\bar{f}_{ijk}$ are the random reflection coefficient, normalized spatial frequency, and normalized Doppler frequency, respectively, of the $(i^{\text{th}}, j^{\text{th}}, k^{\text{th}})$ clutter patch.

The random clutter patch reflection, α_{ijk}, is a realization from the patch clutter-to-noise ratio (CNR), ξ_{ijk}, where ξ_{ijk} is calculated with the bistatic radar range equation as

$$\xi_{ijk} = \frac{P_t G_T g_R \lambda^2 \sigma_{ijk} F_T^2 f_R^2}{(4\pi)^3 k T_s B_n L_T L_R R_T^2 R_R^2}, \tag{3.3}$$

where g_R represents the gain of one channel. Assuming a Rayleigh clutter model (e.g. Gaussian voltage), the clutter patch reflection for a single

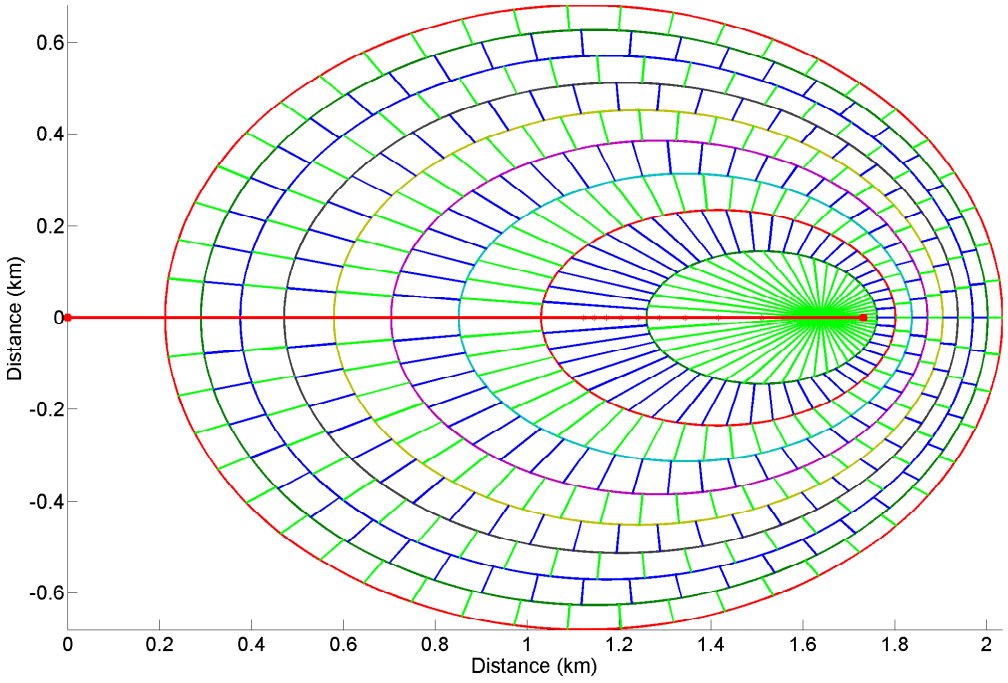

Figure 3.1: The dissection of isorange contours into clutter patches.

channel and pulse is [69]

$$\alpha_{ijk} = \Gamma\sqrt{\xi_{ijk}\sigma_n^2}, \tag{3.4}$$

where $\Gamma \sim CN(0,1)$ and σ_n is a single channel and single pulse noise power. The clutter patch bistatic radar cross section (RCS), σ_{ijk}, in (3.3) is calculated as

$$\sigma_{ijk} = \sigma_0(\theta_I, \theta_S, \phi_{OP})A_{ijk}, \tag{3.5}$$

where A_{ijk} is the area of the i^{th} j^{th} k^{th} clutter patch and σ_0 is the clutter patch normalized RCS coefficient. Previous literature shows bistatic clutter measurements where σ_0 is strongly dependent on geometry [2]–[5], [7],

[54]. However, this geometry-dependent variation is often overlooked in the simulation-based literature. Therefore, an interpolation model based off the measured responses from [54] is generated to determine σ_0 in (3.5) as a function of the clutter patch coordinate parameters θ_I, θ_S, and ϕ_{OP}. These parameters will be defined in the next section and are used to uniquely define a patch's relative location in the local clutter coordinate system.

Clutter Coordinate System

In a bistatic system, ground clutter geometry can be described by in-plane and out-of-plane scattering angles [54]. Figure 3.2 introduces the two in-plane angles, θ_I and θ_S, and the out-of-plane angle, ϕ_{OP}. For a fixed instant in time, every ground clutter patch has a unique combination of in-plane and out-of-plane angles that describe the patch's relative location in three-dimensional space with respect to the receiver and transmitter. When $\phi_{OP} = 180^\circ$ then a forward scattering case is defined, while a backscattering scenario is designated when $\phi_{OP} = 0^\circ$. If $\theta_I = \theta_S$ and $\phi_{OP} = 0^\circ$, then the angles describe a monostatic radar.

Clutter Area

Unlike a monostatic sidelooking STAP configuration, clutter patch area varies within a range bin, which can be easily seen in Figure 3.1. The reason why the patch areas change within a range bin is due to two reasons. First,

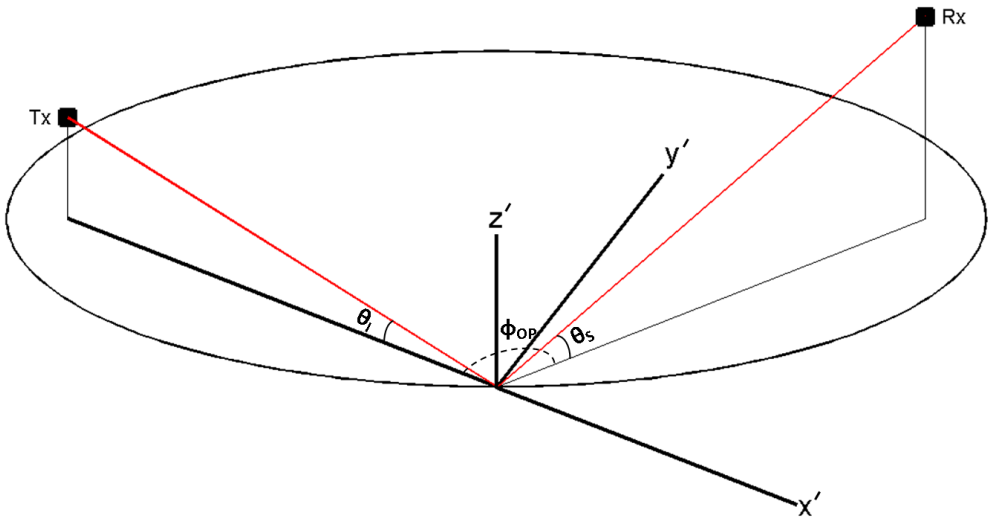

Figure 3.2: The reflectivity coefficient for each patch varies by angles θ_I, θ_S, and ϕ_{OP} defined here [54]. A forward scattering case is defined when $\phi_{OP} = 180^\circ$, while a monostatic case is when $\phi_{OP} = 0^\circ$ and $\theta_I = \theta_S$.

it is assumed that $h_R > h_T$, which creates non-concentric isorange contours. In other words, the center of each elliptical contour is unique and causes varying patch areas. Second, as R_B increases the eccentricity of the isorange contours decrease. This change in eccentricity causes patch area to change while traversing around a range bin. Figure 3.3 illustrates this concept by comparing concentric isorange contours within the bistatic plane with concentric ellipses that maintain constant eccentricity with increasing size.

After inspecting the clutter patch shapes from Figure 3.1, a four sided polygon appears to approximate the patch area effectively. Figure 3.4 magnifies one patch from Figure 3.1 to qualitatively showcase this approxima-

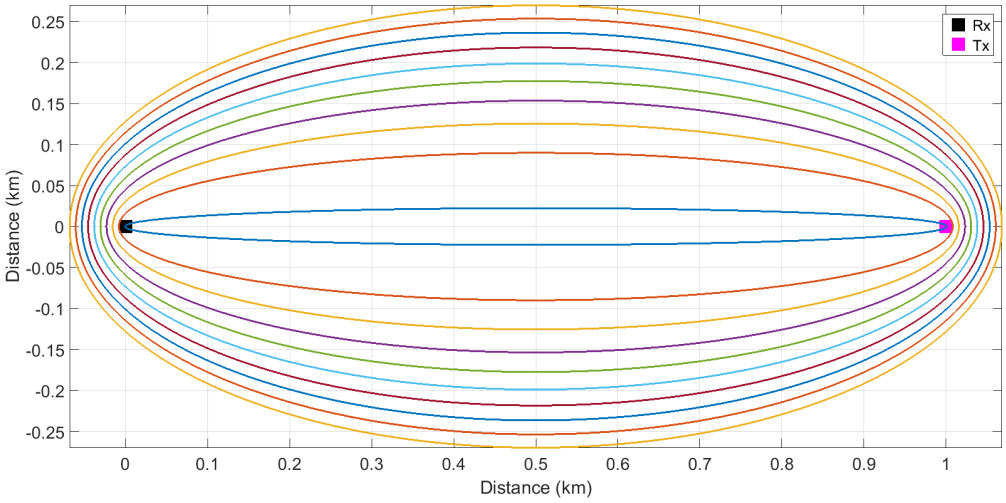

(a) Isorange contours within the bistatic plane

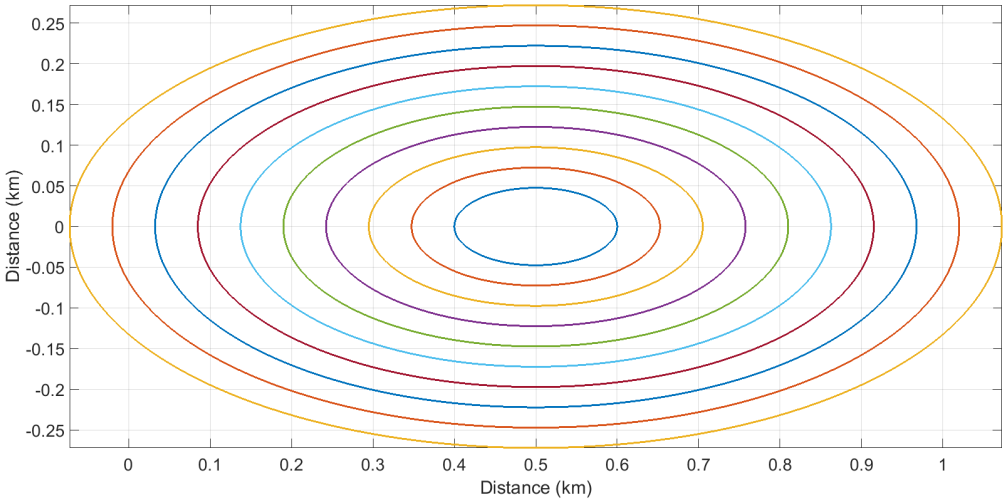

(b) Concentric ellipses that maintain eccentricity

Figure 3.3: Concentric ellipses in (a) maintain foci locations that cause eccentricity to change while concentric ellipses in (b) maintain eccentricity that cause foci to change locations.

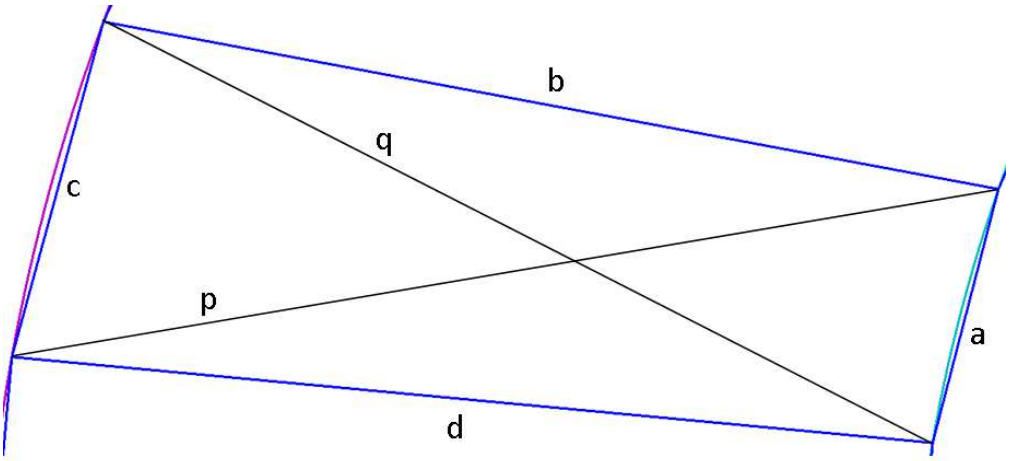

Figure 3.4: The area of a clutter patch is approximated as a general quadrilateral defined above.

tion. The area of a general quadrilateral is calculated as [70]

$$A = \frac{1}{4}\sqrt{4p^2q^2 - (b^2 + d^2 - a^2 - c^2)^2}, \tag{3.6}$$

where the variables a, b, c, d, p, and q are lengths denoted in Figure 3.4.

Clutter RCS Coefficient

As previously stated, the RCS coefficient is found from an interpolation model that is generated from scattering observations presented in Figures 9.2 and 9.5 of [54].The value of σ_0 depends on the combination of the in-plane and out-of-plane ground clutter patch angles [2]–[5]. Overall, the angle that contributed the greatest impact on the clutter patch RCS coefficient was seen as ϕ_{OP}. When ϕ_{OP} is at an extreme, that is either 0° (back scattering) or 180° (forward scattering), σ_0 is at its strongest reflectivity. However,

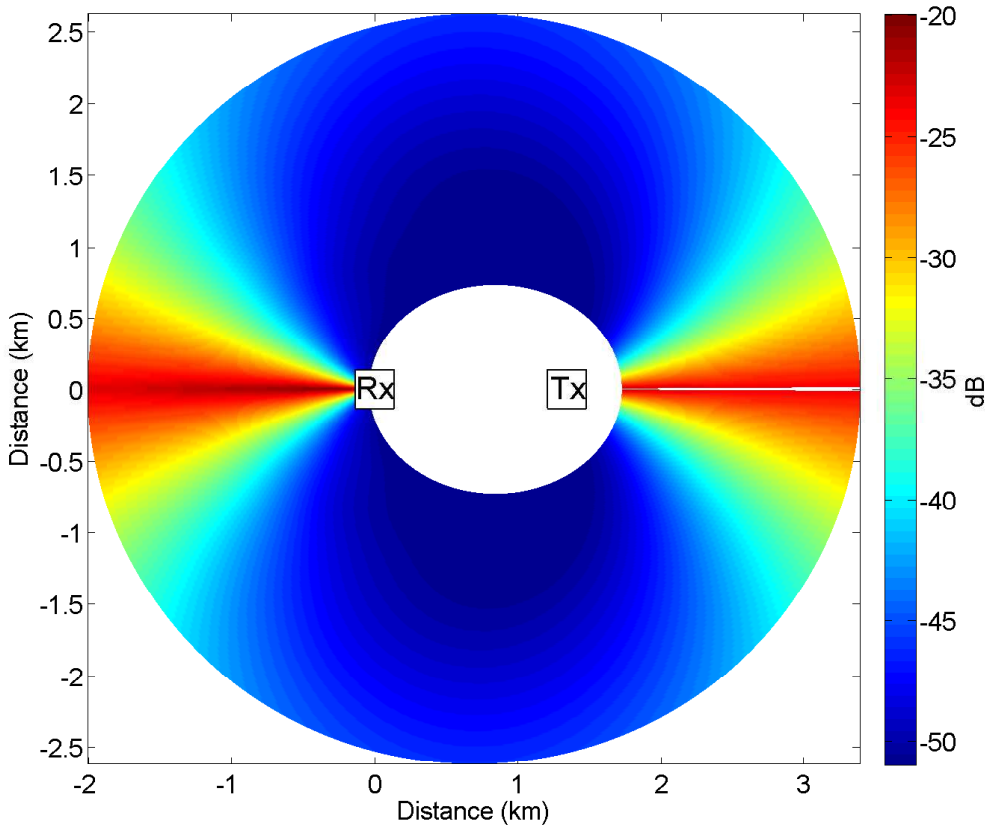

Figure 3.5: Modeled σ_0 for every clutter patch when $h_R = 1$ km, $h_T = 60$ m, $\theta = -35^\circ$ and $L \approx 1.6$ km.

the weakest value for σ_0 is when ϕ_{OP} is around 90° [12]. Figure 3.5 depicts the variation of σ_0 over wide range of clutter patch angles where the receiver and transmitter locations are $(0, 0, 1.0\text{km})$ and $(1.3\text{km}, 0, 60\text{m})$ respectively. High reflectivity is shown in the red regions where ϕ_{OP} is near 0°.

3.1.2 Clutter Power Results

The received clutter power, $\xi\sigma_n^2$, from (3.3) is depicted over a large area in Figure 3.6. Every variable from the bistatic radar equation is taken into

account in Figure 3.6. The receiver was assumed to have a backlobe attenuation of 30 dB in the calculation. Furthermore, the receiver's antenna was modeled as a uniform linear array (ULA) with eight sub-arrays at half-wavelength spacing in azimuth. Plus, the sub-array consisted of eight vertically stacked antenna elements spaced at half-wavelength increments. These sub-array antenna patterns contain elevation nulls that are seen in Figure 3.6 as the circular notches. Overall, the most influential variables on the clutter power distribution were the antenna patterns, clutter patch RCS, and range.

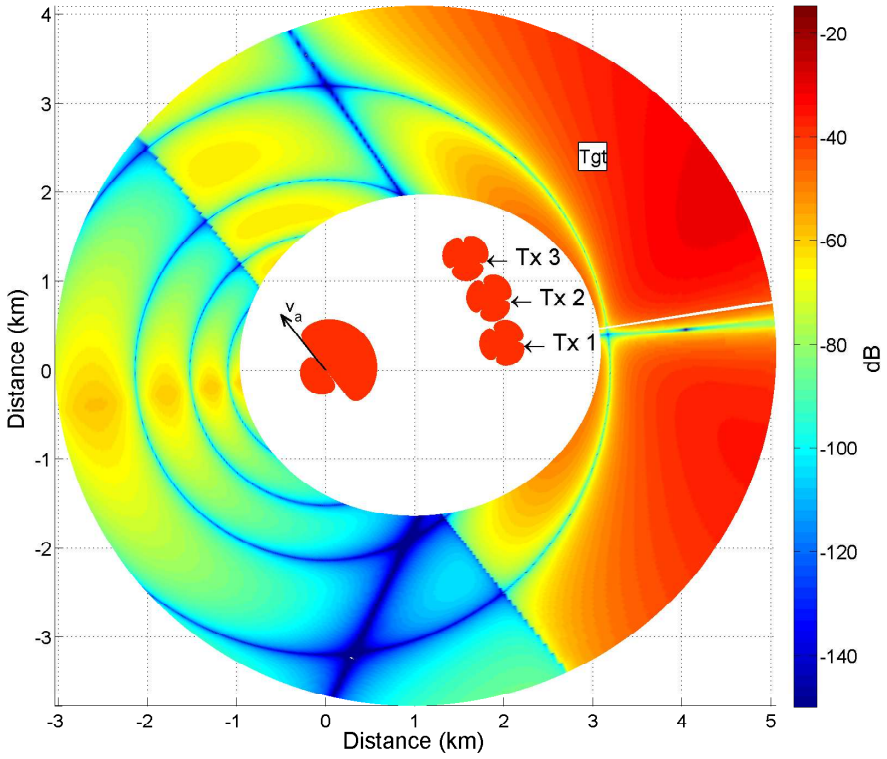

Figure 3.6: Received clutter power for transmitter one emissions over all range bins of interest. The calculated power received takes into account all variables in the radar range equation for each bistatic combination. The constants across transmitters are the antenna directivity towards the target and transmit power.

3.2 Passive STAP

While Chapter 2 introduced bistatic geometry and STAP, the particular details that pertain to a PBR system were not covered. Now that the clutter interpolation model has been covered, the details of passive STAP can be discussed. First, the PBR clutter response within the angle-Doppler domain will be defined. Then a moving target's Doppler shift will be derived.

3.2.1 Passive STAP Clutter

As a reminder, the defined passive system is a multi-channel radar receiver that is mounted onto an airborne platform in a side looking configuration and uses emitters of opportunity for the radar waveform. Therefore, the airborne platform still induces a Doppler shift on the clutter that is extending in both angle and range. However, the stationary transmitter does not induce a Doppler shift on the clutter, which is unlike monostatic and bistatic systems. Therefore, a passive system results in an induced Doppler shift that is half the shift experienced by monostatic system when keeping the receive platforms' velocity and the radar waveforms' wavelengths constant. An induced Doppler shift is defined by

$$f_d = \frac{\hat{\mathbf{k}}_{\mathbf{Rx}} \cdot \mathbf{v}_{\mathbf{Rx}} + \hat{\mathbf{k}}_{\mathbf{Tx}} \cdot \mathbf{v}_{\mathbf{Tx}}}{\lambda}, \tag{3.7}$$

where the unit vectors $\hat{\mathbf{k}}_{\mathbf{Rx}}$ and $\hat{\mathbf{k}}_{\mathbf{Tx}}$ represent the respective line of sight directions from the receiver and transmitter to a point on the ground, and $\mathbf{v}_{\mathbf{Rx}}$ and $\mathbf{v}_{\mathbf{Tx}}$ are the respective receiver and transmitter velocity vectors in three-dimensional space. For a monostatic case where $\hat{\mathbf{k}}_{\mathbf{Rx}} = \hat{\mathbf{k}}_{\mathbf{Tx}}$ and $\mathbf{v}_{\mathbf{Rx}} = \mathbf{v}_{\mathbf{Tx}}$, (3.7) reduces to the familiar equation of $f_d = 2v_r/\lambda$ where v_r is the projected radial velocity of the monostatic platform. However, a PBR system where $\mathbf{v}_{\mathbf{Tx}} = 0$ causes (3.7) to reduce to

$$f_d = \frac{v_r}{\lambda}. \tag{3.8}$$

For a ULA with elemental azimuth spacing defined by $\mathbf{d} = d\hat{\mathbf{y}}$ and the receive platform velocity given as $\mathbf{v}_{\mathbf{Rx}} = v_a\hat{\mathbf{y}}$, then $\hat{\mathbf{k}}_{\mathbf{Rx}}$ can be formally written as

$$\hat{\mathbf{k}}_{\mathbf{Rx}} = \cos\theta\cos\phi\hat{\mathbf{x}} + \cos\theta\sin\phi\hat{\mathbf{y}} + \sin\theta\hat{\mathbf{z}}, \tag{3.9}$$

where θ and ϕ are the elevation (defined as negative) and azimuth angles from the ULA reference channel to a point on the ground ($x-y$ plane). The normalized Doppler shift for a clutter patch , $\bar{f}$, becomes

$$\bar{f} = \frac{\hat{\mathbf{k}}_{\mathbf{Rx}} \cdot \mathbf{v}_{\mathbf{Rx}}}{\lambda f_r} = \frac{v_a}{\lambda f_r}\cos\theta\sin\phi, \tag{3.10}$$

where f_r is the pulse repetition frequency. The normalized spatial frequency for a clutter patch, ϑ, is defined as

$$\vartheta = \frac{\hat{\mathbf{k}}_{\mathbf{Rx}} \cdot \mathbf{d}}{\lambda} = \frac{d}{\lambda} \cos\theta \sin\phi. \tag{3.11}$$

Equations (3.10) and (3.11) allow a clutter patch's angle-Doppler response to be defined in the following linear relationship

$$\bar{f} = \frac{v_a d}{\lambda f_r d} \cos\theta \sin\phi = \frac{v_a}{f_r d} \vartheta. \tag{3.12}$$

Overall, (3.12) shows that $\bar{f}$ is a linear function of $\cos\theta \sin\phi$, which is not the case in traditional bistatic radar where both receiver and transmitter platforms are moving. Therefore, if the azimuth and elevation angles are restricted to one elliptical range bin, then a clutter ridge is described in normalized Doppler and spatial frequency space with a linear slope, η, of

$$\eta = \frac{v_a}{f_r d}. \tag{3.13}$$

This clutter ridge relates where in $\bar{f}$ and ϑ space the clutter energy resides. In STAP, $\mathbf{w_k}$ adaptively filters the clutter contributions, $\mathbf{c_k}$, from $\mathbf{x_k}$ along this clutter ridge.

Figure 3.7 depicts linear clutter ridges for two different range bins for $\eta = 1$, or equivalently, $v_a = f_r d = f_r \lambda / 2$. In Figure 3.7a, it is seen that the clutter power distribution is more localized for an isorange contour that is highly eccentric. Meanwhile, the longer R_B shown in Figure 3.7b causes a lower eccentricity contour and results in a clutter power distribution that is more extended in angle-Doppler. This observation can be explained in two parts. First, for highly eccentric isorange contours as seen in Figure 3.1, the dynamic range of θ and ϕ restrict the dynamic range of both $\bar{f}$ and ϑ. Second, the clutter RCS varies with angle. Figure 3.5 illustrates the strongest clutter more localized at shorter ranges and becomes more widely spread with increasing bistatic range.

Finally, the monostatic and PBR clutter ridge differences must be outlined. First, monostatic radar produces a clutter ridge within a range bin where $\bar{f}$ is a linear function of $\sin\phi$ whereas $\bar{f}$ behaves linearly with $\cos\theta\sin\phi$ in a PBR system. This difference is due to the fact that $\cos\theta$ and $\sin\phi$ are decoupled in a monostatic radar because the range bins are circular (e.g. $\cos\theta$ is constant within the range bin). So maintaining a constant range for monostatic radar, results in a constant elevation angle and $\bar{f}$ changes linearly with the sine of the azimuth angle. However, to maintain constant bistatic range in a PBR system, both θ and ϕ vary while traversing the elliptical isorange contour. Second, as previously stated, the Doppler shift from a PBR system

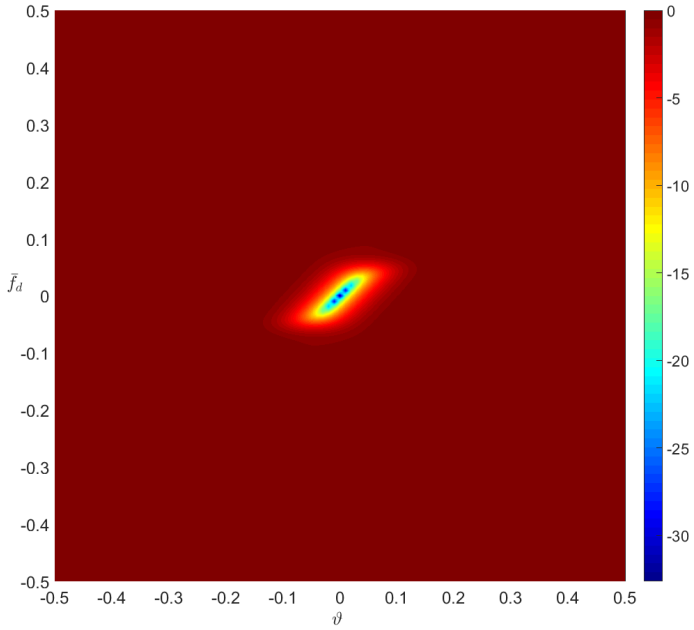

(a) For isorange contour of $R_B \approx 2.43$ km where $e \approx 0.77$

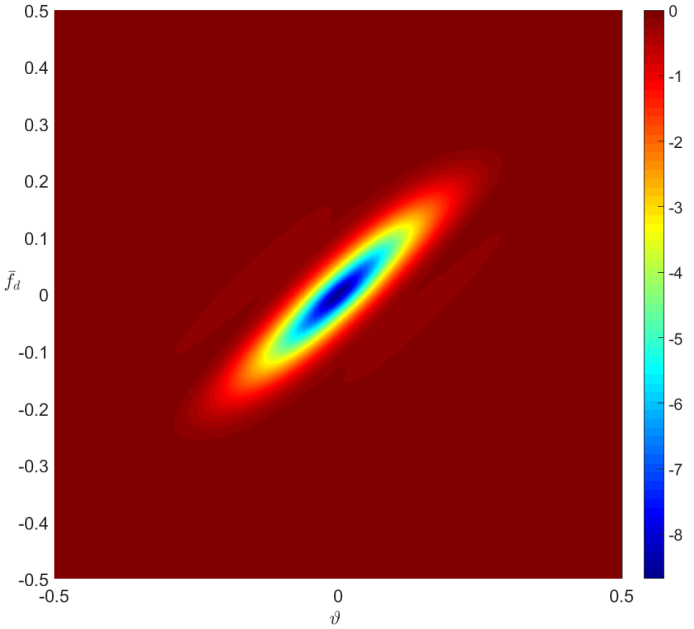

(b) For isorange contour of $R_B \approx 8.85$ km where $e \approx 0.21$

Figure 3.7: Clutter contributions over normalized Doppler and spatial frequency for two different isorange contours when the receiver and transmitter are located at $(0, 0, 1\text{ km})$ and $(1.63\text{ km}, 0, 60\text{ m})$ respectively.

is half that of a monostatic. This factor continues through to the slope of the clutter ridge. So keeping v_a, f_r, and d constant results in $\eta = \eta_M/2$, where η_M is the monostatic clutter slope.

3.2.2 Passive STAP Target Response

The total Doppler response, $\bar{f}_{tot}$ from a moving target is the sum of two Doppler shifts: 1) Doppler shift induced by the radar receiver platform, $\bar{f}$, 2) the moving target Doppler shift, $\bar{f}_{tgt}$. Similar to (3.7), the the Doppler shift induced by the moving target, f_{tgt}, is defined as

$$\begin{aligned} f_{tgt} &= \frac{\hat{\mathbf{k}}_{\mathbf{Rx}} \cdot \mathbf{v}_{\mathbf{tgt}} + \hat{\mathbf{k}}_{\mathbf{Tx}} \cdot \mathbf{v}_{\mathbf{tgt}}}{\lambda} \\ &= \frac{v_{tgt}}{\lambda} \left(\hat{\mathbf{k}}_{\mathbf{Rx}} \cdot \hat{\mathbf{v}}_{\mathbf{tgt}} + \hat{\mathbf{k}}_{\mathbf{Tx}} \cdot \hat{\mathbf{v}_{\mathbf{tgt}}} \right), \end{aligned} \tag{3.14}$$

where $\hat{\mathbf{v}}_{\mathbf{tgt}}$ and v_{tgt} are the target's velocity direction and magnitude (speed), respectively. Figure 3.8 introduces angles δ and $\beta/2$, which allow (3.14) to be expressed as

$$\begin{aligned} f_{tgt} &= \frac{v_{tgt}}{\lambda} \left[\cos\left(\delta - \frac{\beta}{2}\right) + \cos\left(\delta + \frac{\beta}{2}\right) \right] \\ &= \frac{2v_{tgt}}{\lambda} \cos\delta \cos\frac{\beta}{2}. \end{aligned} \tag{3.15}$$

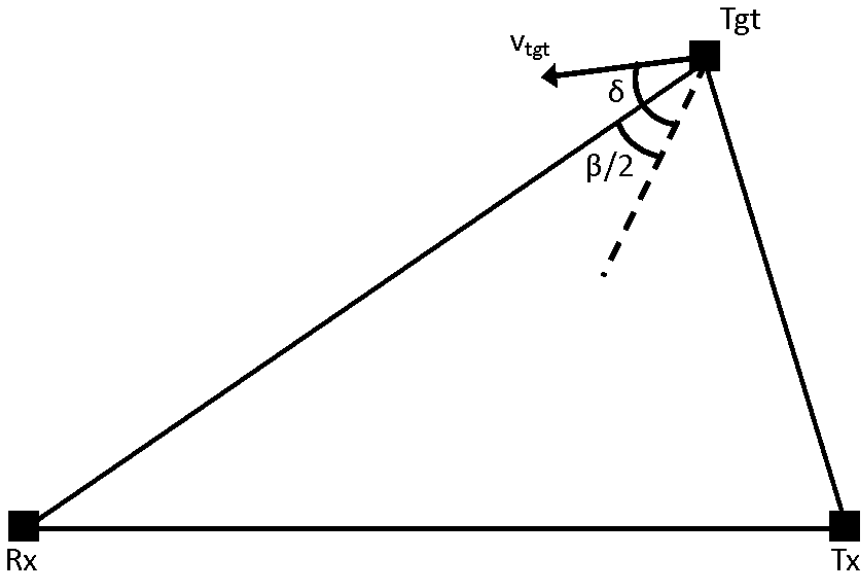

Figure 3.8: Target velocity defined in the bistatic plane.

Then the normalized target Doppler shift becomes

$$\bar{f}_{tgt} = \frac{2v_{tgt}}{\lambda f_r} \cos\delta \cos\frac{\beta}{2}, \tag{3.16}$$

and the total normalized Doppler shift, $\bar{f}_{tot}$, is

$$\begin{aligned} \bar{f}_{tot} &= \bar{f} + \bar{f}_{tgt} \\ &= \frac{v_a}{\lambda f_r} \cos\theta \sin\phi + \frac{2v_{tgt}}{\lambda f_r} \cos\delta \cos\frac{\beta}{2}, \end{aligned} \tag{3.17}$$

where θ and ϕ define the location of the target.

3.3 Waveform Analysis and Effects

The effects from an uncooperative waveform must be considered when modeling passive radar performance. In this research, the chosen passive emitter is assumed to be broadcasting an LTE signal. Therefore, an LTE waveform's structure and properties will first be introduced. Then the particular performance effects related to STAP will be described.

3.3.1 LTE Waveform

The LTE waveform is based off an orthogonal frequency division multiplexing (OFDM) scheme and is partitioned in time into frames, subframes, and slots. Each of these categories span a respective duration of 10 ms, 1 ms, and 0.5 ms. A slot consists of either six or seven symbols that are dictated by the chosen cyclic prefix (CP) [36]. Last, every slot contains a number of orthogonal subcarrier signals where the number of subcarriers are directly related to the signal's bandwidth. At the maximum number of subcarriers, a signal bandwidth of approximately 20 MHz is achieved, which gives a monostatic range resolution of approximately 7.5 m.

The CP exists to assist in the mitigation of multipath signals by making each CP a data copy of the respective symbol's end portion. The chosen CP mode defines the time duration of the CP. In the extended mode, each slot contains six symbols where all six CPs are of uniform duration equal to

16.67 μs. In turn, the data carrying symbol duration is set to 66.67 μs. So to maintain subcarrier orthogonality, a frequency step of 15 kHz is used between each subcarrier within the signals bandwidth. In the maximum LTE bandwidth configuration, there are 1320 subcarriers present, which equates to a bandwidth of $B = 15 \text{ kHz}(1320) = 19.8 \text{ MHz}$ [36]. More details about the LTE waveform can be found in the published standards from the European Telecommunications Standards Institute [71].

In this research, a pulse is defined as one LTE symbol with maximum bandwidth/subcarriers. Additionally, each pulse consists of random simulated user data; thus, the waveform is considered a pulse-diverse waveform over the CPI. Furthermore, each pulse varies in energy due to the randomness of the user data.

3.3.2 Modeling Pulse-Diverse Waveform for STAP

Unfortunately, pulse-diverse waveforms result in poor clutter filtering [45] due to pulse-to-pulse decorrelation of the clutter spectrum. If strong clutter is present, then pulse-diverse waveforms can lead to SINR performance that is clutter-limited across all Doppler shifts. This Doppler modulation effect has also been termed as clutter-Doppler spread [46], [47].

The Doppler modulation effect can be incorporated by first defining a direct path signal from the m^{th} pulse as $x_m(\tau)$. Then the normalized auto-

correlation of the m^{th} pulse, $R_{xx}^{m}(\tau)$, is

$$\begin{aligned} R_{xx}^{m}(\tau) &= \frac{x_m(\tau) * x_m^*(-\tau)}{E_m} \\ &= \frac{1}{E_m}\int_{-\infty}^{\infty} x_m(t)x_m^*(t-\tau)\,\mathrm{d}t, \end{aligned} \tag{3.18}$$

where $x_m^*(-\tau)$ is the complex-conjugated and time reversed signal of $x_m(\tau)$, and E_m is the energy in the m^{th} pulse. The pulse energy is calculated as

$$E_m = \int_0^{\Delta\tau} |x_m(t)|^2\,\mathrm{d}t. \tag{3.19}$$

At one channel, n, and one pulse, m, the clutter contributions can be defined at time τ_0 as a continuous sum of voltage response over angle and time that is written as

$$\begin{aligned} c[m,n] &= \iint_{-\infty\Delta\vartheta}^{\infty} \alpha(\tau,\vartheta)R_{xx}^{m}(\tau-\tau_0)b_m(\bar{f})a_n(\vartheta)\mathrm{d}\vartheta\mathrm{d}\tau \\ &= \iint_{-\infty\Delta\vartheta}^{\infty} \alpha(\tau,\vartheta)R_{xx}^{m}(\tau-\tau_0)b_m\left(\frac{v_a}{f_r d}\vartheta\right)a_n(\vartheta)\mathrm{d}\vartheta\mathrm{d}\tau, \end{aligned} \tag{3.20}$$

where $\Delta\vartheta$ represents the span of illuminated spatial frequencies at time τ (which maps to propagation delay), and $b_m(\bar{f})$ and $a_n(\vartheta)$ are the m^{th} and n^{th} elements in the steering vectors from (2.27) and (2.29) respectively. Additionally, (3.20) uses (3.12) to perform a change of variables and illustrate

that the slow-time phase element can be represented in terms of spatial frequency, $b_m(v_a\vartheta/f_rd)$. From here on, the temporal and spatial phase elements will be written as b_m and a_n and the integral limits will be implied.

Letting a taper, $\mathbf{t}(\tau)$, be defined as

$$\mathbf{t}(\tau) = \begin{bmatrix} R_{xx}^1(\tau) \\ R_{xx}^2(\tau) \\ \vdots \\ R_{xx}^M(\tau), \end{bmatrix} \tag{3.21}$$

allows (3.20) to be expressed as a M length vector of pulse clutter contributions at a single spatial channel, which is written as

$$\mathbf{c}[n] = \iint \alpha(\tau, \vartheta) \left(\mathbf{t}(\tau - \tau_0) \odot \mathbf{b}\right) a_n \mathrm{d}\vartheta \mathrm{d}\tau, \tag{3.22}$$

where $\odot$ is the Hadamard product (element or piece-wise product). The taper captures the pulse-dependent distributed contributions ($R_{xx}^m(\tau)$) over range, or fast-time, when integrating over τ. Additionally, the taper captures pulse-to-pulse modulation across slow-time, which gives rise to the clutter Doppler spreading seen in pulse-diverse waveforms [47]. In other words, at a particular time τ, the taper includes the scattering contributions that enter the current range bin (located at time τ_0) through the range

sidelobes while simultaneously modulating the slow-time temporal steering vector that varies with the distance from the range bin at delay τ_0. Lastly, the clutter contributions from (3.22) can be further vectorized into the common space-time notation that is given as

$$\mathbf{c} = \iint \alpha(\tau, \vartheta) \left[\mathbf{t}(\tau - \tau_0) \odot \mathbf{b}\right] \otimes \mathbf{a} \, \mathrm{d}\vartheta \mathrm{d}\tau. \tag{3.23}$$

where the clutter contributions, $\mathbf{c}$, are now a column vector of length MN.

With the definition of the space-time clutter contributions completed in (3.23), the clutter covariance matrix (CCM) at the CUT, $\mathbf{R_c}$, becomes

$$\begin{aligned}
\mathbf{R_c} &= E\left[\mathbf{c}\mathbf{c}^{\mathrm{H}}\right] \\
&= E\Bigg[\left(\iint \alpha(\tau, \vartheta) \left[\mathbf{t}(\tau - \tau_0) \odot \mathbf{b}\right] \otimes \mathbf{a} \, \mathrm{d}\vartheta \, \mathrm{d}\tau\right) \times \\
&\quad \left(\iint \alpha(\tau', \vartheta') \left[\mathbf{t}'(\tau' - \tau_0) \odot \mathbf{b}'\right] \otimes \mathbf{a}' \, \mathrm{d}\vartheta' \, \mathrm{d}\tau'\right)^{\mathrm{H}}\Bigg] \\
&= \iiiint E\left[\alpha(\tau, \vartheta)\alpha^*(\tau', \vartheta')\right] \left(\left[\mathbf{t}(\tau - \tau_0) \odot \mathbf{b}\right] \otimes \mathbf{a}\right) \times \\
&\quad \left(\left[\mathbf{t}'(\tau' - \tau_0) \odot \mathbf{b}'\right] \otimes \mathbf{a}'\right)^{\mathrm{H}} \mathrm{d}\vartheta \, \mathrm{d}\tau \, \mathrm{d}\vartheta' \, \mathrm{d}\tau'.
\end{aligned} \tag{3.24}$$

Assuming the clutter contributions are uncorrelated in space and time where $E\left[\alpha(\tau, \vartheta)\alpha^*(\tau', \vartheta')\right] = \xi(\tau, \vartheta)\delta(\tau' - \tau, \vartheta' - \vartheta)$ and $\delta(\tau' - \tau, \vartheta' - \vartheta)$ is a two-dimensional Dirac delta function, allows the incorporation of the sifting

property. Then (3.24) becomes

$$
\begin{aligned}
\mathbf{R_c} &= \iint \xi(\tau,\vartheta)\left([\mathbf{t}(\tau-\tau_0)\odot\mathbf{b}]\otimes\mathbf{a}\right)\times \\
&\quad \left([\mathbf{t}(\tau-\tau_0)\odot\mathbf{b}]\otimes\mathbf{a}\right)^{\mathrm{H}}\mathrm{d}\vartheta\,\mathrm{d}\tau \\
&= \iint \xi(\tau,\vartheta)\left[\left(\mathbf{t}(\tau-\tau_0)\otimes\mathbf{1}^{N\times N}\right)\odot(\mathbf{b}\otimes\mathbf{a})\right]\times \\
&\quad \left[\left(\mathbf{t}(\tau-\tau_0)\otimes\mathbf{1}^{N\times N}\right)\odot(\mathbf{b}\otimes\mathbf{a})\right]^{\mathrm{H}}\mathrm{d}\vartheta\,\mathrm{d}\tau \\
&= \int\left(\mathbf{t}(\tau-\tau_0)\mathbf{t}^{\mathrm{H}}(\tau-\tau_0)\otimes\mathbf{1}^{N\times N}\right)\odot \\
&\quad \int\xi(\tau,\vartheta)\,(\mathbf{b}\otimes\mathbf{a})\,(\mathbf{b}\otimes\mathbf{a})^{\mathrm{H}}\,\mathrm{d}\vartheta\,\mathrm{d}\tau \\
&= \int\mathbf{T}(\tau-\tau_0)\odot\mathbf{R}_{\mathbf{c},\tau}\,\mathrm{d}\tau,
\end{aligned}
\tag{3.25}
$$

where $\mathbf{1}^{u\times v}$ is a matrix of ones with dimensions of $u\times v$, $\mathbf{R}_{\mathbf{c},\tau}$ is the CCM evaluated at delay τ, and $\mathbf{T}(\tau-\tau_0)$ is known as a covariance matrix taper (CMT) [72]. The use of CMTs is a method developed for modeling various types of interference subspace leakage (ISL) and other decorrelating effects [73]. For example, CMTs have been used to model STAP performance effects from intrinsic clutter motion (ICM), antenna jitter, bandwidth dispersion, etc., [74]. Here, the use of CMTs has been extended to model clutter-Doppler spreading due to the decorrelation of range sidelobes resulting from a pulse diverse waveform.

It is now worth examining how (3.25) changes with different assumptions of the radar waveform. First, if the waveform is comprised of M iden-

tical pulses, then only one autocorrelation function exists causing $\mathbf{t}(\tau) = R_{xx}(\tau) \otimes \mathbf{1}^{M\times 1}$ and $\mathbf{T}(\tau) = R_{xx}(\tau) \otimes \mathbf{1}^{MN\times MN}$. Therefore, the CMT in (3.25) can be represented as a scalar multiplication equal to the autocorrelation function, which varies in time/range and given as

$$\mathbf{R_c} = \int R_{xx}(\tau - \tau_0)\mathbf{R}_{\mathbf{c},\tau}\,\mathrm{d}\tau. \tag{3.26}$$

The CCM calculated from (3.26) still includes the range sidelobes that result of matched filtering. However, the effects of Doppler modulation that arise from pulse diverse waveforms are now eliminated.

Alternatively, for an ideal waveform where it is assumed that no range sidelobes exist or $R_{xx}^{m}(\tau) = \delta(\tau)$, the taper and CMT respectively become $\mathbf{t}(\tau) = \delta(\tau) \otimes \mathbf{1}^{M\times 1}$ and $\mathbf{T}(\tau) = \delta(\tau) \otimes \mathbf{1}^{MN\times MN}$. Then after applying the sifting property, (3.25) reduces to

$$\begin{aligned}\mathbf{R_c} &= \mathbf{R}_{\mathbf{c},\tau_0} \\ &= \int \xi(\tau_0, \vartheta)\mathbf{s}\mathbf{s}^H \mathrm{d}\vartheta,\end{aligned} \tag{3.27}$$

where $\mathbf{s}$ is the steering vector defined in (2.30). The CCM in (3.27) now only depends on the clutter power within the CUT described at delay τ_0. Also note, whether or not the waveform is pulse diverse holds no bearing on the

CCM when an ideal waveform is assumed. If there are no sidelobes in fast time, then there can not be any Doppler modulation over slow time.

With clutter-Doppler spreading derived, Figure 3.9 illustrates the potential performance effects through SINR loss curves. In STAP, SINR loss represents the degradation in performance that is due to interference (other than receiver noise) where 0 dB represents no loss. At spatial frequencies where high clutter energy exists, clutter-Doppler spread occurs from the pulse-to-pulse decorrelation (slow-time or Doppler) of the clutter spectrum, which is seen as the entire curve being clutter limited across Doppler (refer to $\mathbf{R_c}$ curve in Figure 3.9). So when modeling PBR performance, clutter-Doppler spread must be included.

3.4 Model Comparison

Clutter-Doppler spreading is more prominent at spatial frequencies where large clutter power resides. Therefore, the method for modeling the RCS of bistatic ground clutter dictates the severity of the expected performance degradation from pulse-diverse waveforms. To illustrate the model dependent performance degradation effects, two previously published models will be introduced and then compared. From this point forward, the three models shall be specified as the in-plane, out-of-plane (IPOP) model as char-

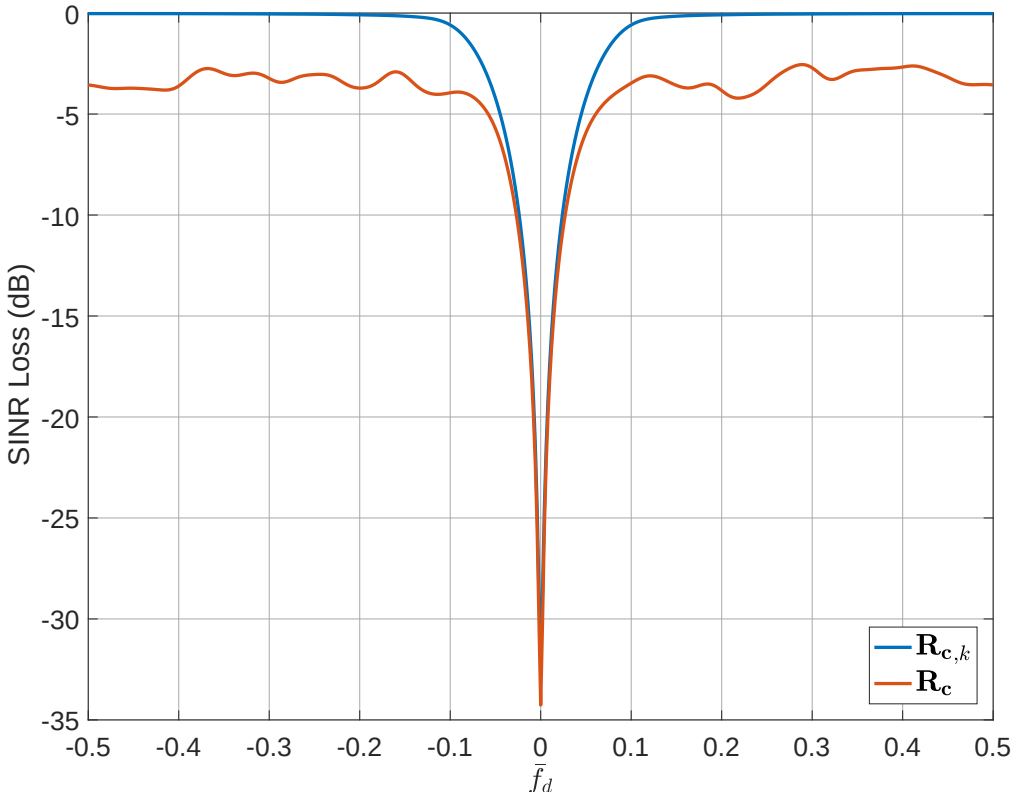

Figure 3.9: SINR Loss comparison between (3.27) and (3.25). When incorporating clutter-Doppler spreading, then the entire SINR Loss curve can become clutter limited and not reach the full potential processing gain outside the clutter notch.

acterized in Section 3.1, the extended constant gamma (ECG) model from [10], and the Aviation and Missile Command (AMCOM) model from [4].

3.4.1 ECG Model

Barton first formulated the constant gamma model as [75]

$$\sigma_0 = \gamma \sin \psi \tag{3.28}$$

where γ and ψ are the normalized reflectivity parameter and grazing angle respectively. The reflectivity parameter is scene dependent. For example, farm land is modeled around -15 dB while wooded hills force γ to be 5 dB greater [75].

The ECG model reformulates the traditional constant gamma model RCS coefficient and assimilates the propagation factors for the transmitter and receiver, F_T and F_R. So ECG defines σ_0 as

$$\sigma_0 = \gamma \sqrt{\sin(\psi_R) \sin(\psi_T)} F_T^2 F_R^2, \tag{3.29}$$

where

$$F_{T,R}^2 = 1 + \rho_{T,R}^2 - 2\rho_{T,R}\cos\left(\frac{4\pi\sigma_H \sin(\psi_{T,R})}{\lambda}\right) \tag{3.30}$$

$$\rho_{T,R}^2 = \exp\left[-\left(\frac{4\pi\sigma_H \sin(\psi_{T,R})}{\lambda}\right)^2\right]. \tag{3.31}$$

The variables $\rho_{T,R}$, $\psi_{T,R}$, and σ_H are, respectively, the specular scattering factors, grazing angles, and RMS surface roughness for the transmitter and receiver where applicable [10].

3.4.2 AMCOM Model

The AMCOM model, similar to ECG, is a specular model and defines the bistatic clutter RCS coefficient as [4]

$$\sigma_0 = \bar{\rho}_s^2 R_0^2, \tag{3.32}$$

where R_0 is the reflection coefficient for a smooth surface that is based off the Fresnal equation and $\bar{\rho}_s$ is the RMS value of the specular scattering factor. These variables are calculated as

$$\bar{\rho}_s = \frac{\lambda \sin(2\pi\Delta h \sin(\gamma)\,\lambda)}{2\pi\Delta h \sin(\gamma)} \tag{3.33}$$

$$R_0 = \frac{-\eta_1 \cos\theta_i + \eta_2 \cos\theta_t}{\eta_1 \cos\theta_i + \eta_2 \cos\theta_t}, \tag{3.34}$$

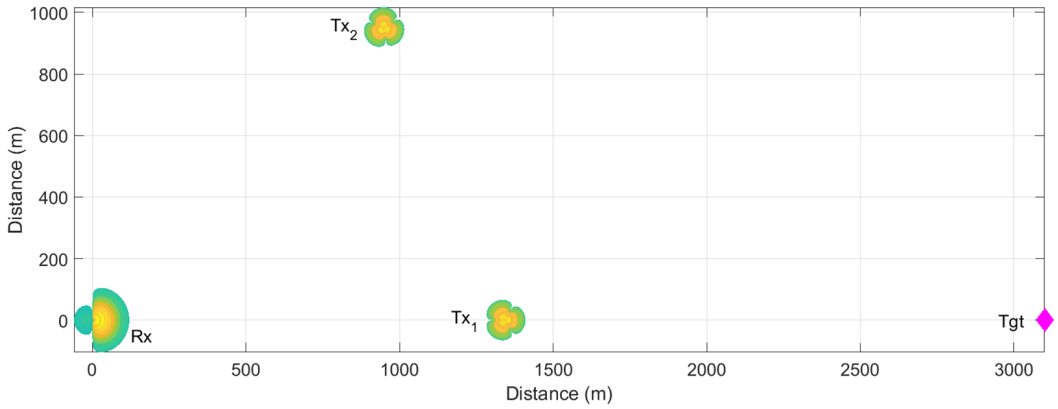

Figure 3.10: Ground plane locations for the simulation used to compare models.

where Δh and γ in (3.33) are the standard deviation of disturbance height and depression angle. Meanwhile, η_1, η_2, θ_i and θ_t in (3.34) respectively represent the intrinsic impedances of air and the clutter material and the angles of incidence and transmittance.

3.5 Analysis & Results

Consider a scenario where a receiver, two transmitters, and a target reside at global coordinates of $(0, 0, 1\text{ km})$, $(1.34\text{ km}, 0, 0.06\text{ km})$, $(0.95\text{ km}, 0.95\text{ km}, 0.06\text{ km})$, and $(3.1\text{ km}, 0, 0)$ as seen in Figure 3.10. Furthermore, assume $\mathbf{v_{Rx}} = v_a\hat{y}$ where v_a is chosen to achieve a clutter ridge slope of one. It can be seen from Figure 3.10 that the first transmitter lies in-plane relative to the receiver and target while the second transmitter is located outside of the x-z plane. Furthermore, the bistatic baseline, L, is held constant across

transmitters at roughly 1.6 km and the transmitters' antenna patterns are directed at the target.

With the simulation setup in mind, Figure 3.11 illustrates the SINR Loss in normalized angle-Doppler space for both transmitters at the respective range bins of the target for all three models: IPOP, ECG, and AMCOM. The impacts of the different methods for modeling bistatic RCS coefficients of the clutter patches are easily seen in Figure 3.11. First, while the strength of the clutter from the ECG and AMCOM models can be adjusted through their respective control parameters, both assume out-of-plane scattering to be equally strong as in-plane scattering. To be clear, in-plane scattering occurs at the spatial frequency where a transmitter is located because of backward or forward scattering effect. Therefore, in-plane scattering is at zero spatial frequency for the first transmitter and 0.29 for the second transmitter. So in theory, clutter strength should be move localized around $\vartheta = 0$ for the first transmitter (Figures 3.11a, 3.11c, and 3.11e) and $\vartheta = 0.29$ for the second transmitter (Figures 3.11b, 3.11d, and 3.11f). However, the ECG and AMCOM models produce strong clutter power that is distributed further out in angle/spatial frequency (Figures 3.11c-f). On the other hand, the IPOP method models clutter power that varies with out-of-plane angle and results in a more focused distribution across the spatial/Doppler frequencies (Figures 3.11a-b).

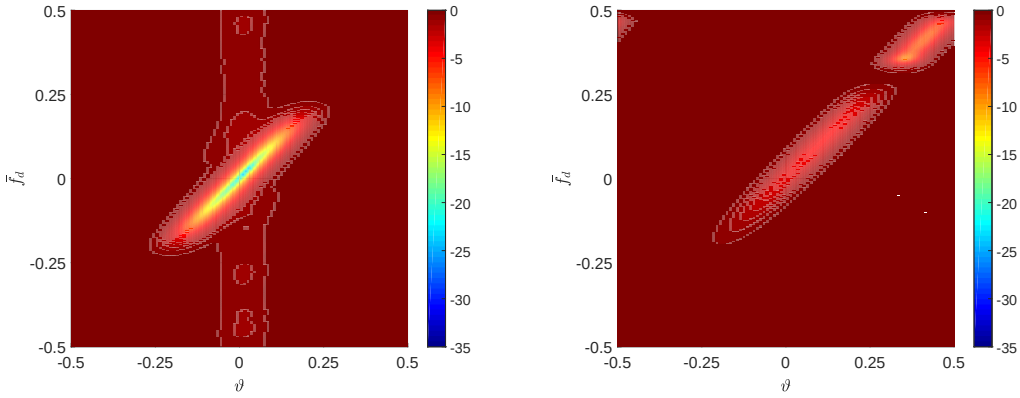

(a) IPOP Tx_1 (b) IPOP Tx_2

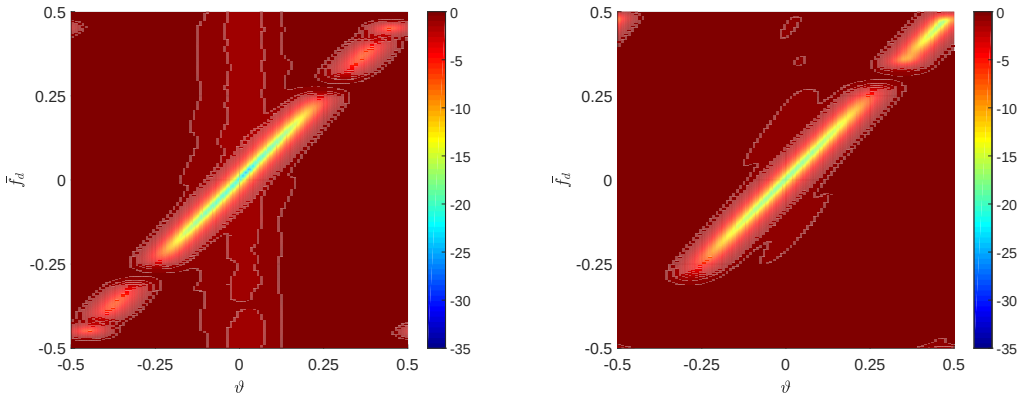

(c) ECG Tx_1 (d) ECG Tx_2

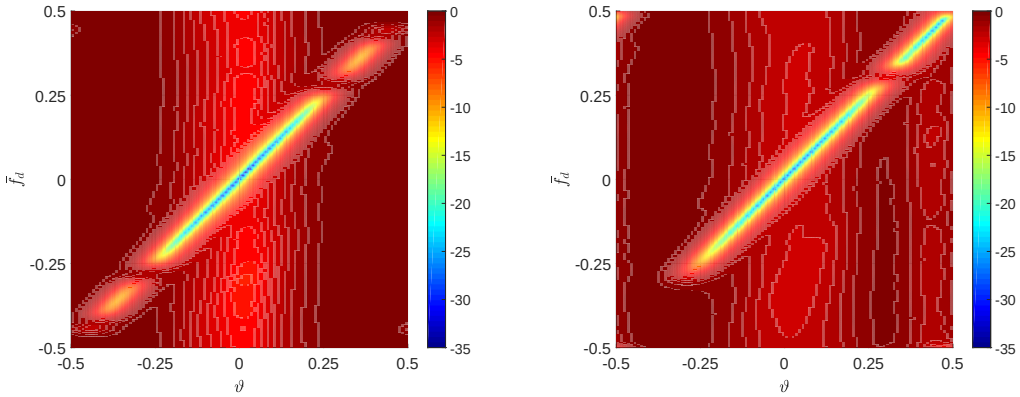

(e) AMCOM Tx_1 (f) AMCOM Tx_2

Figure 3.11: SINR Loss in angle and Doppler for three different bistatic clutter RCS coefficient models and two transmitters.

A related second observation comes from comparing the SINR loss between the transmitters. The differences between transmitters for the ECG and AMCOM models arise from the antenna pattern orientations. Figure 3.10 depicts the nulls of the transmitters' antenna patterns. These nulls appear in the two-dimensional SINR Loss curves from Figure 3.11 in the vicinity of $\vartheta = 0.25$ and $\vartheta = -0.25$ for the first transmitter (column one) and $\vartheta = 0.30$ for the second transmitter (column two). However, the IPOP method is modeling weaker RCS coefficients for the out-of-plane scatterers plus the inclusion of the antenna pattern orientations. In particular, Figure 3.11b models very weak clutter overall because the second transmitter's antenna pattern has a null where strong clutter returns appear at the in-plane scattering angle/frequency.

A third observation comes from the clutter-Doppler spread. Modeling higher clutter-to-noise ratio (CNR) increases the severity of the clutter-Doppler spread. For example, Figure 3.11 shows that the strongest clutter across models appears at the zero spatial cut for the first transmitter. However, the loss across Doppler is the worst for AMCOM. This observation can also be seen in Figure 3.12a by comparing the solid and dashed SINR curves. The solid curves represent optimal SINR without modeling a pulse-diverse waveform whereas the dashed lines are the SINR curves that include the clutter-Doppler spread effect. Notice there is about 1 dB loss across Doppler

for the IPOP and ECG models while approximately 5 dB lose is experienced for the AMCOM model. This greater loss is due to the larger modeled clutter RCS coefficients. Therefore, to understand the pulse-diverse waveform performance impacts in passive radar, the chosen clutter model will dictate the degree of impact from clutter-Doppler spread.

Figure 3.12 shows that the first transmitter in Figure 3.12a experiences higher SINR than the second in Figure 3.12b within the exo-clutter region. This better performance is attributed to the $R_T^2 R_R^2$ product from the bistatic radar range equation as discussed in Section 2.1.2. The first transmitter's location creates a range product that is approximately 2.5 dB smaller than the second transmitter's range product.

Once again the difference in modeling out-of-plane scattering can be seen when comparing the clutter notch depth between transmitters. Even though the notch depth decreases for all models when going from the first to the second transmitter, the relative decrease is greatest for the IPOP model. As previously mentioned, the decreases in notch depths are attributed to antenna patterns for the ECG and AMCOM models.

Finally, the severity of performance loss that comes from clutter-Doppler spread can be seen in Figure 3.12. In particular, the IPOP model simulates weak clutter at zero spatial frequency (target location) for the second transmitter, which causes insignificant clutter-Doppler spread. Therefore, in a

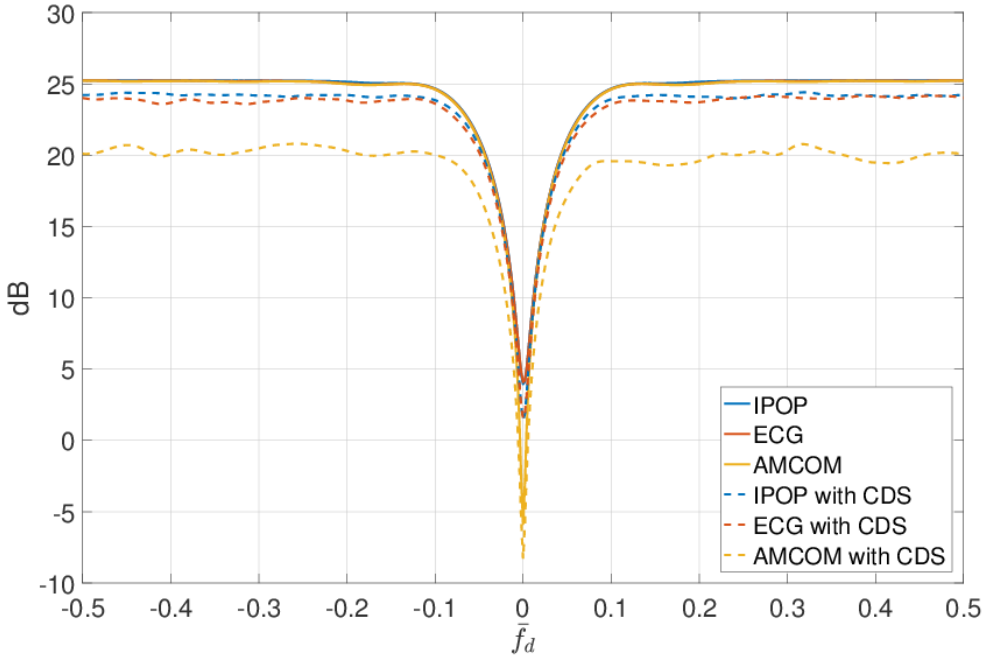

(a) Transmitter #1

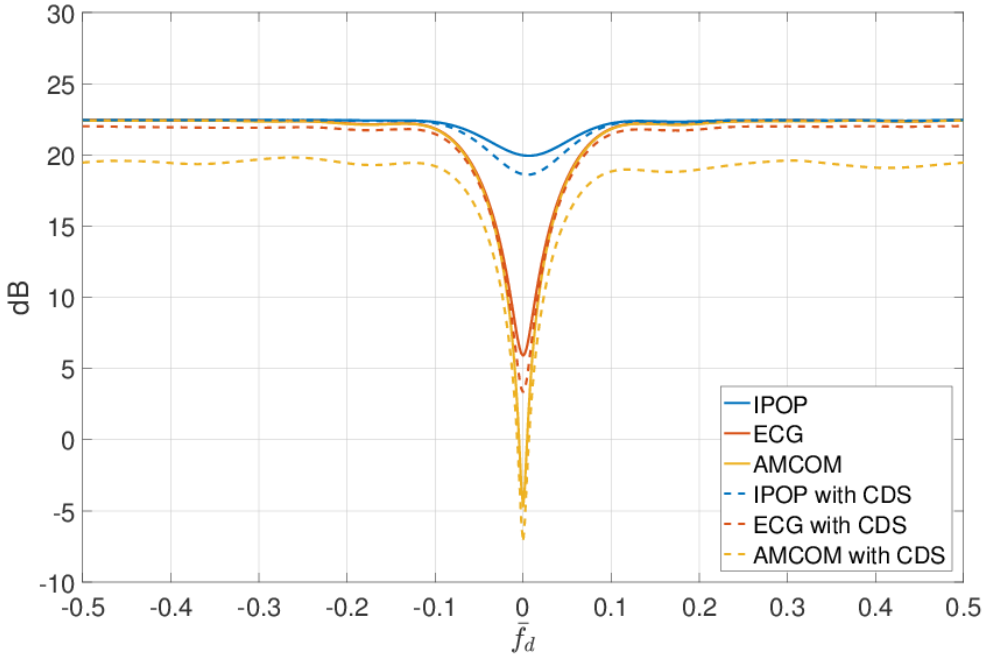

(b) Transmitter #2

Figure 3.12: SINR at the zero spatial cut for Transmitter #1 and Transmitter #2 across the three models that include and exclude clutter-Doppler spread.

scenario where the passive receive platform must down-select to an optimal emitter, the second transmitter would be chosen for the IPOP modeling method, while the first transmitter would likely be selected for the other models. The next chapter will focus on this interesting problem of how to down-select to an optimal emitter when multiple emitters are present. Furthermore, only the IPOP model will be considered henceforth.

Chapter 4

Passive STAP Emitter Selection Metrics

In a scenario where multiple emitters exist, down-selecting to an optimal emitter becomes an interesting problem. It is a difficult problem that is influenced by many competing and coupled parameters. In this chapter, four metrics will be introduced and analyzed. The choice of emitter greatly depends on where a target is located. Therefore, Section 4.2 outlines the simulation setup that is used to vary a target's location over a large spatial grid. Then, Section 4.3 gives the results of the metrics over the spatial grid while also providing a detailed analysis.

4.1 Metrics

The metrics used for comparing emitters of opportunity are the average SINR, weighted average SINR, minimum SINR, and usable velocity space fraction (UVSF). These proposed metrics attempt to distinguish the perfor-

mance between emitters against a target's four unknown parameters: (x, y) location and (v_x, v_y) velocity.

4.1.1 Average SINR

Signal-to-interference-plus-noise ratio (SINR) is the most commonly used metric for STAP performance. For Gaussian interference, probability of detection, P_d, is a monotonic function of SINR [60]. Thus, a higher average SINR can suggest a better P_d for an unknown target location and velocity. So the probability of detection for an unknown target Doppler of uniform distribution is statistically best for high average SINR. The average SINR, SINR_{Avg}, is calculated as

$$\text{SINR}_{\text{Avg}} = \int_{-0.5}^{0.5} \text{SINR}(0, \bar{f}_d) \mathrm{d}\bar{f}_d, \tag{4.1}$$

where the average is being calculated at the zero spatial cut.

4.1.2 Weighted SINR Average

Instead of a uniform Doppler distribution, let the target two-dimensional velocity be uniformly distributed. This distribution gives equal probability for an unknown target moving in any direction on the ground, which can be a practical assumption in a search scenario. Mapping the uniform veloc-

ity distribution into normalized Doppler leads to a non-uniform Doppler distribution that is dependent on target location relative to the transmitter and receiver. Figure 4.1 illustrates two different Doppler distributions for two different bistatic angles. Overall, approximately 50% of velocities occur within the boundary defined by $|\bar{f}_d| \leq 0.1$. Therefore, the weighted average SINR metric, SINR_{WA}, distinguishes transmitters by the average SINR within the boundary of $-0.1 \leq \bar{f}_d \leq 0.1$ and calculated as

$$\text{SINR}_{\text{Avg}} = \int_{-0.1}^{0.1} \text{SINR}(0, \bar{f}_d) \mathrm{d}\bar{f}_d. \tag{4.2}$$

The weighted average SINR metric, in turn, places more emphasis on slow moving targets that appear in the vicinity of the clutter notch.

4.1.3 Minimum SINR

One possible method of choosing an emitter of opportunity is by selecting the transmitter with the best worst-case performance. The worst-case performance is defined as the minimum SINR, SINR_{Min}, across all Doppler at the zero spatial cut and written as

$$\text{SINR}_{\text{Min}} = \min_{-0.5 \leq \bar{f}_d < 0.5} \left(\text{SINR}(0, \bar{f}_d) \right) \tag{4.3}$$

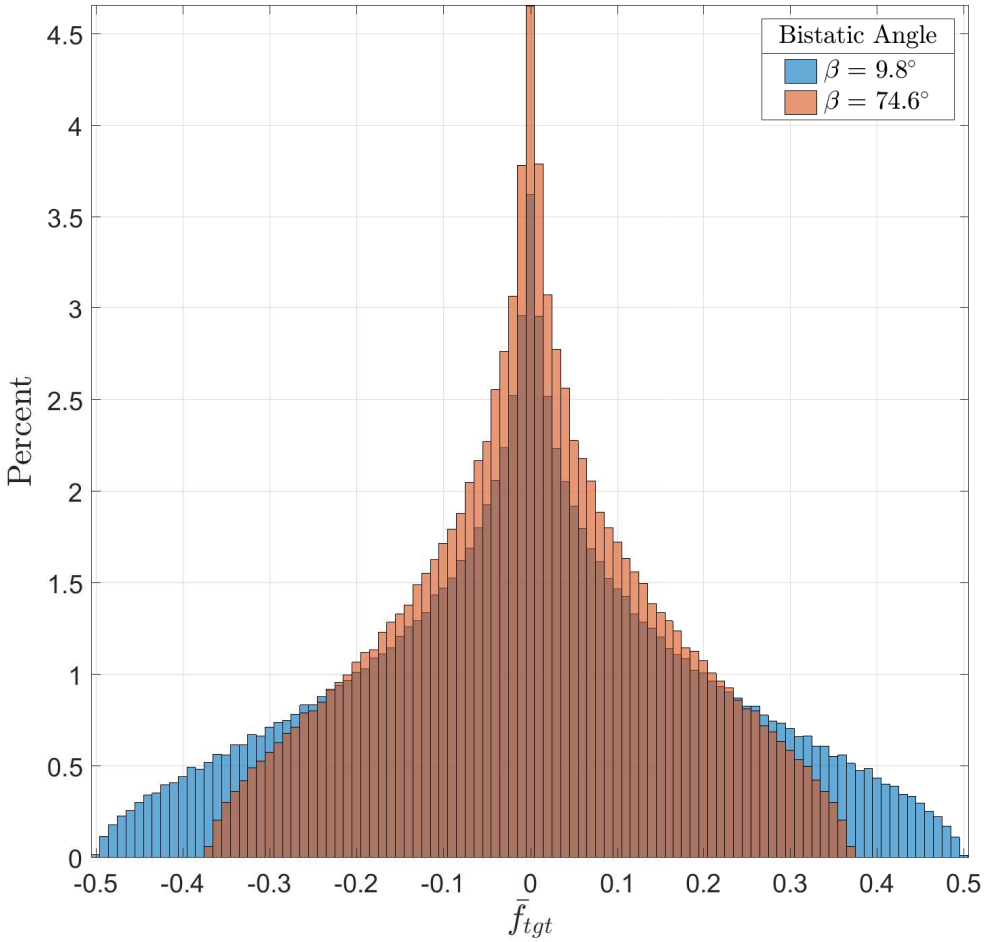

Figure 4.1: Comparison of velocity distribution for two different bistatic angles.

Selecting the highest SINR_{Min} across emitters is ultimately optimizing between low clutter energy from SINR curve and low $R_R^2 R_T^2$ product from bistatic radar range equation. In turn, this metric favors transmitters that are out-of-plane with respect to the receiver and target, while also exhibiting an $R_R^2 R_T^2$ product that gets favorable SNR. The balancing that takes place depends primarily on the relative geometries of the target, receiver, and all possible emitters.

4.1.4 Usable Velocity Space Fraction

A common STAP metric is the usable Doppler space fraction (UDSF). The UDSF is the percentage of Doppler frequencies that exceed the SINR detection threshold (DT) where the DT is the SINR performance needed to detect a target. However, the mapping from velocities to Doppler frequencies is not constant across relative geometries for bistatic radar. This is observed by referring back to Figure 4.1 where the Doppler frequencies change for different emitter locations or bistatic angles. Therefore, a new STAP metric for PBR is proposed as the usable velocity space fraction (UVSF). In lieu of Doppler frequencies, the UVSF is the percentage of unambiguous velocities that exceed the SINR DT. Thus, this metric is considered a three-step process in calculating. First, SINR Doppler frequencies that fall below the DT are captured. Second, these poor performing SINR Doppler frequencies are mapped into velocities based off the relative geometry under consideration. Third, the percentage of detectable velocities is calculated. It is assumed the necessary DT is 12 dB.

4.1.5 Discussion

Figure 4.2 graphically depicts the metrics. In Figure 4.2a the difference between SINR_{Avg}, SINR_{WA}, and SINR_{Min} is easily understood when shown on a SINR curve at a zero spatial cut. The SINR_{Avg} is equally considering

all regions of SINR, noise and clutter, when evaluating an emitter, while SINR_{WA} and SINR_{Min} put more emphasis on the clutter region. Furthermore, it is seen how SINR_{Min} puts the most emphasis on the clutter region, or in turn, slow moving targets. Note, however, that none of these three metrics use the DT. Thus, SINR_{Avg}, SINR_{WA}, and SINR_{Min} distinguish between relative performance of emitters, and do not place any assumptions on the size of a point target.

To be clear, consider the optimal SINR equation given as

$$\text{SINR}_{\text{opt}} = \sigma_s^2 \left| \mathbf{s}^{\text{H}} \mathbf{R_k}^{-1} \mathbf{s} \right|. \tag{4.4}$$

It is seen that SINR_{opt} is directly related to the signal power, σ_s^2, or alternatively, the target RCS. However, changing σ_s^2 does not change the chosen emitter when using SINR_{Avg}, SINR_{WA}, or SINR_{Min}. Therefore, these metrics are considered as relative metrics.

On the other hand, UVSF depends on a DT, which in turn depends on an assumption of the target's RCS. Figure 4.2 uses both subfigures to relate the UVSF metric. Figure 4.2a captures the range of Doppler frequencies, $\bar{f}_d$, that are below the DT, and then depicts the mapping of frequencies to velocities in Figure 4.2b. Even though Figure 4.2 shows $\bar{f}_{tgt}$, it is a one-to-one mapping between $\bar{f}_{tgt}$ and $\mathbf{v_{tgt}}$, but again, there is not a one-to-one mapping between

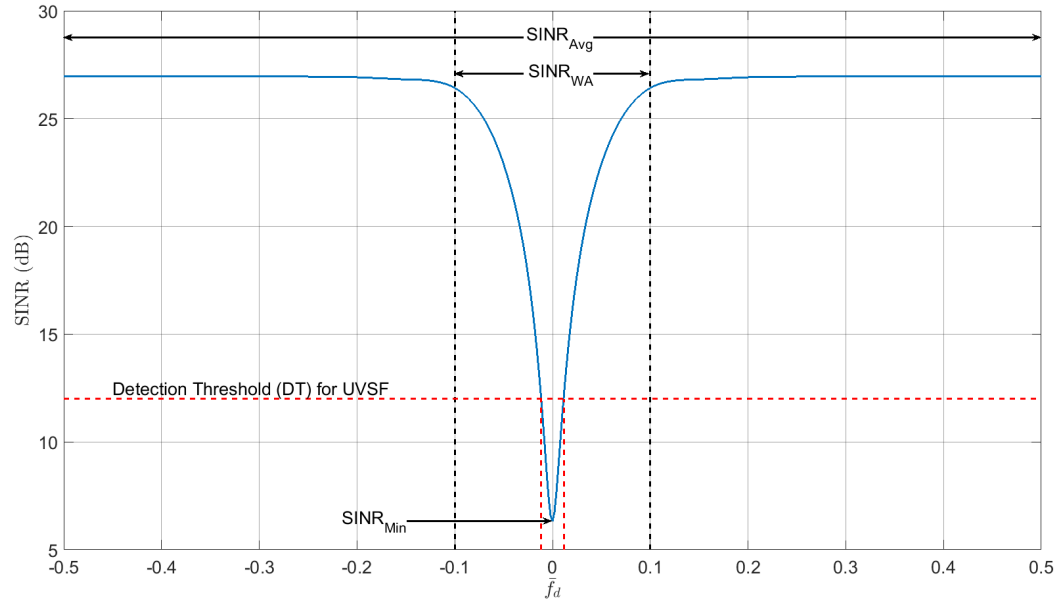

(a) Metrics

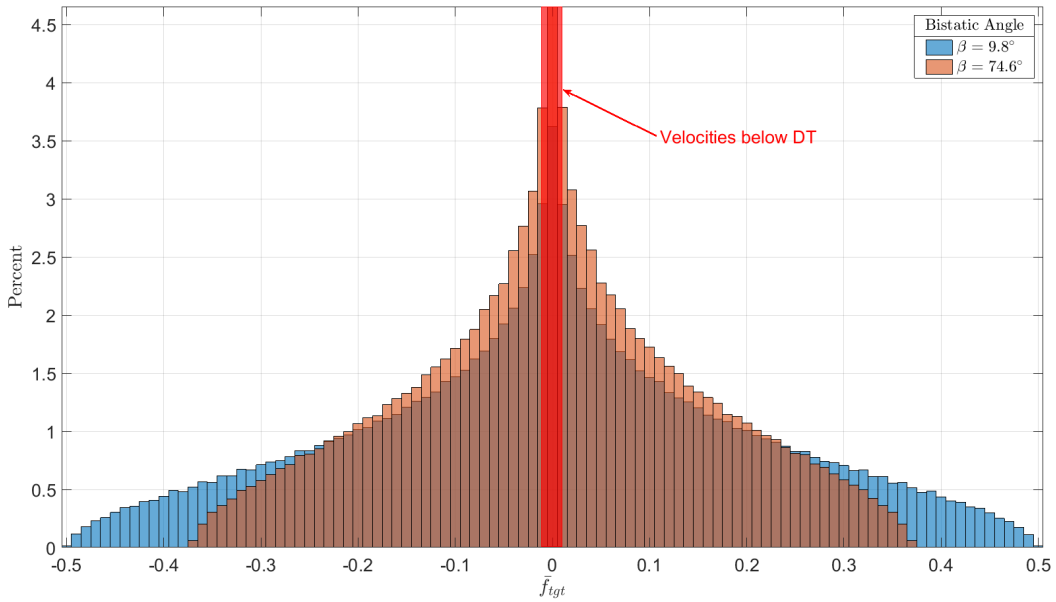

(b) UVSF Mapping

Figure 4.2: Conceptual view of metrics. UVSF is a two-step process that uses a detection threshold (DT).

$\bar{f}_d$ and $\mathbf{v_{tgt}}$. By viewing target velocities as $\bar{f}_{tgt}$, it allows different relative geometries to be plotted on the same axes.

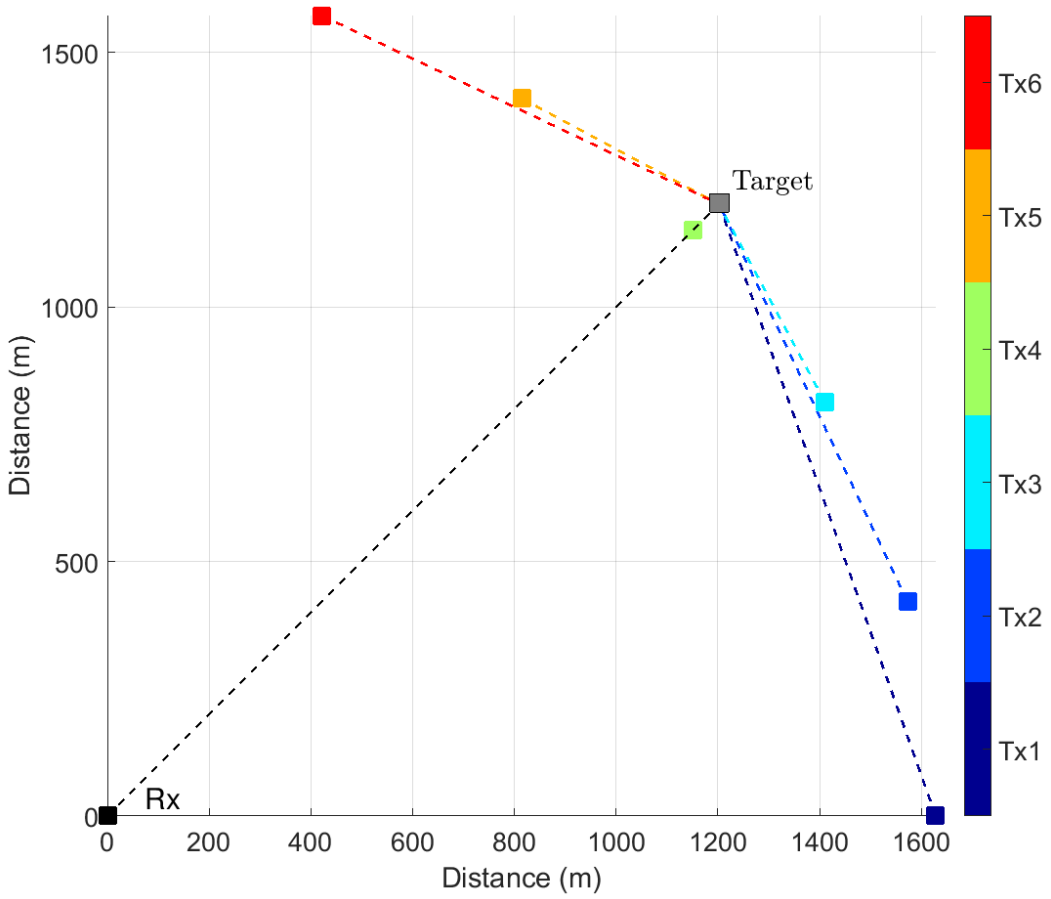

Figure 4.3: Comparison of velocity distribution for two different bistatic angles.

To clarify, consider the scenario depicted in Figure 4.3. All six emitters maintain a constant bistatic baseline, L, and constant height of 60 m. The emitters' azimuth angles, ϕ_T are spaced every 15° and all emitters have an elevation angle of $\theta_T = -35°$. The target located at (1.2km,1.2km,0) is in-plane with the receiver and fourth emitter. Finally, the receiver's coordinates are (0,0,1.0km).

By symmetry, the bistatic angles are constant when comparing either emitters three and five, or emitters two and six. In total, there are four unique bistatic angles for the six transmitters. When considering a uniform set of unambiguous target velocities, then the identical bistatic angles from the two sets of emitters create two identical sets of $\bar{f}_{tgt}$ distributions and two identical UVSF metrics within each set. These equalities only occur when considering the set of unambiguous uniformly distributed velocities as a whole. Choosing just one velocity where $|\mathbf{v_{tgt}}| \neq 0$ will generate six unique $\bar{f}_{tgt}$, where similar $\bar{f}_{tgt}$ groupings occur for emitters two and three and emitters five and six.

Figure 4.4 depicts the target Doppler frequency for each emitter when considering the maximum target speed in the set of unambiguous velocities, $|\mathbf{v_{tgt}}|_{max}$, and 360 different velocity directions, $\hat{\mathbf{v}}_{\mathbf{tgt}}$, that are incremented every degree from 0° to 359°. From Figure 4.4, it can be seen that curves for transmitters two and six, and transmitters three and five are translated versions of each other (identical in dynamic range and shape). It can also be seen how emitters two and three, and emitters five and six have very similar Doppler curves but are not identical. Recall $\bar{f}_{tgt}$ is calculated as

$$\bar{f}_{tgt} = \frac{2v_{tgt}}{\lambda} \cos\delta \cos\frac{\beta}{2}. \tag{4.5}$$

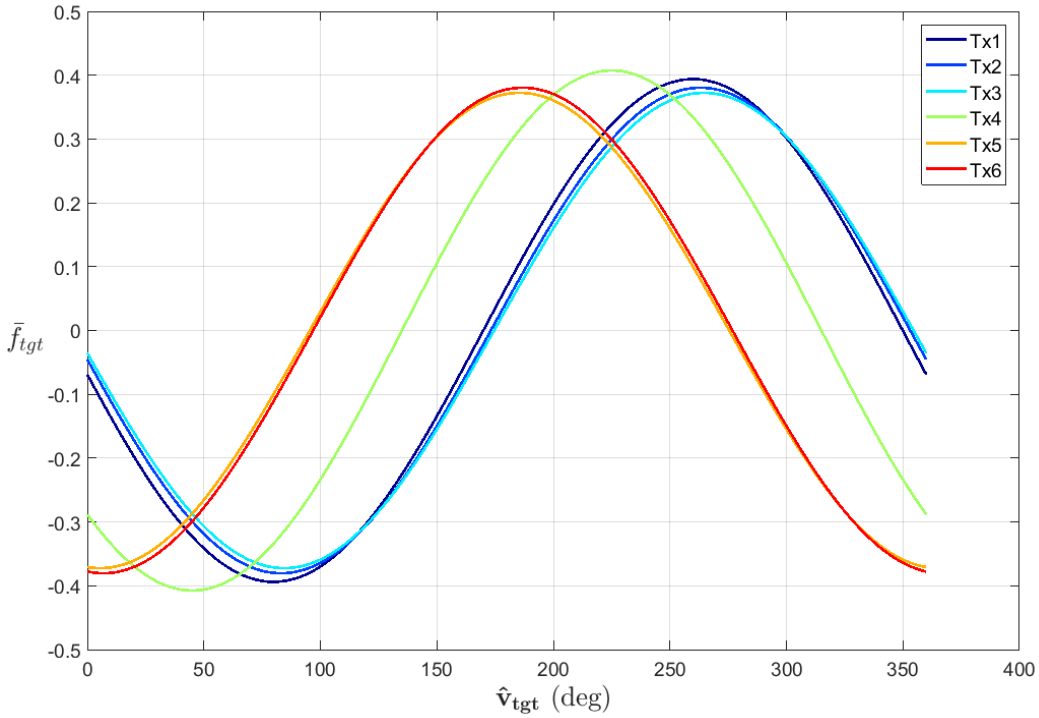

Figure 4.4: Target Doppler frequency curves over velocity angle when considering maximum speed.

The bisector of the bistatic angle controls the dynamic range of the $\bar{f}_{tgt}$ distribution while δ, as defined in Figure 3.8, controls the projection of the velocity vector onto the bisector of the bistatic angle. Figure 4.5 illustrates the changes in directions for all unambiguous velocities. Again, the two sets of transmitters two and three, and transmitters five and six are very similar per set, but could produce different UVSF metrics within each set. However, the sets of emitters two and six, and emitters three and five would have identical UVSF metrics within each set. The UVSF metric does not discriminate which unambiguous velocities are detectable. The UVSF metric

relates how many unambiguous velocities are detectable, which equates to how many target Doppler frequencies are detectable.

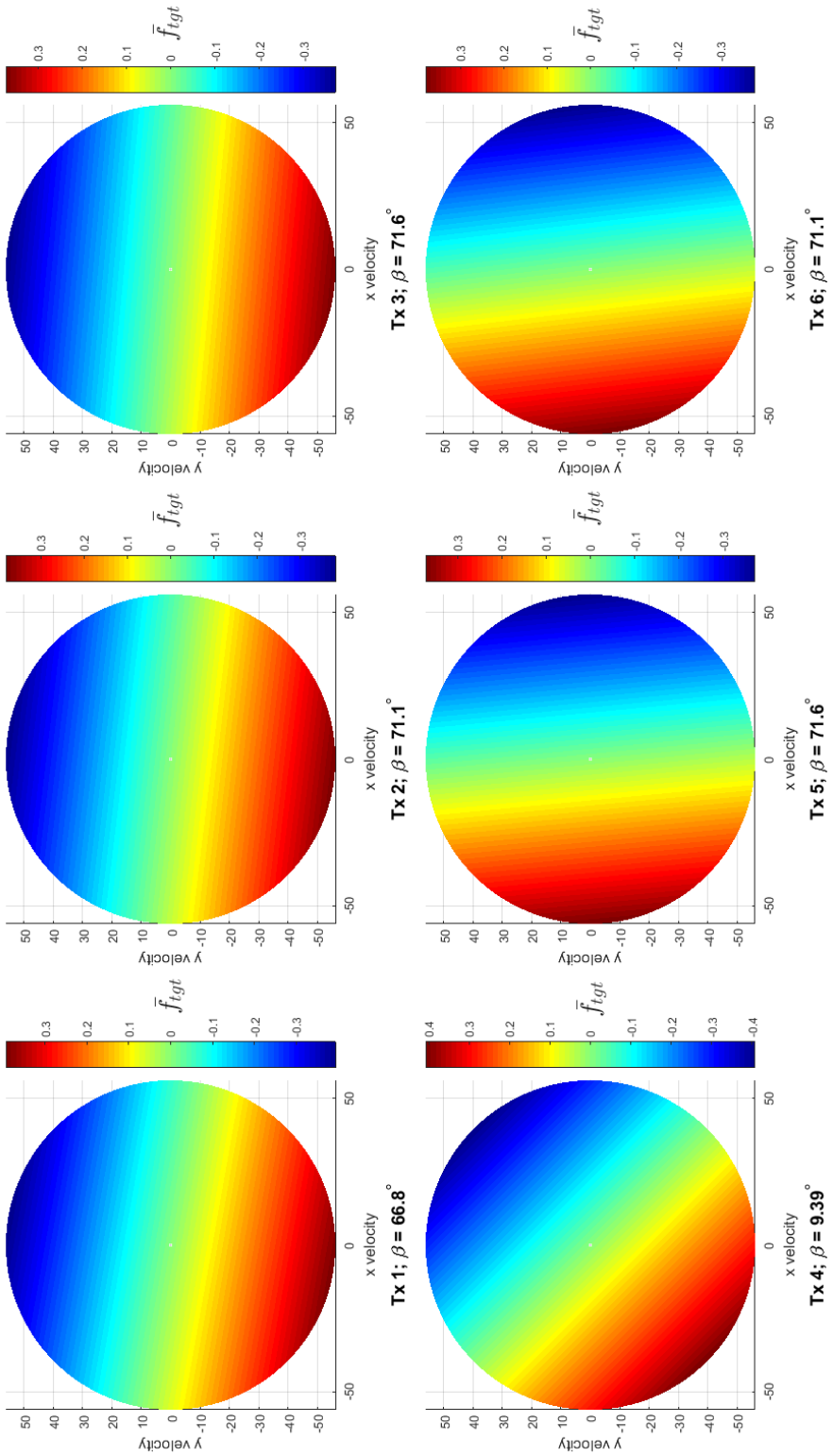

Figure 4.5: Target Doppler frequencies for uniformly spaced $\mathbf{v_{tgt}}$.

4.2 Methodology

The goal is to understand how emitter selection changes over varying target locations and velocities. In a passive radar system, GMTI performance depends on many coupled parameters to include all variables within the bistatic radar range equation, the relative geometries of the receiver, transmitter, and target, and the relative two-dimensional velocities of the receiver and target. With these dependencies in mind, a simulation was developed that calculated SINR_{opt} over a spatially diverse sector for multiple, spatially distinct long-term evolution (LTE) transmitters. Then the metrics from Section 4.1 were evaluated at every spatial point for each transmitter. Last, the emitter that achieved the highest metric was selected.

For the simulation, a pulse is defined as one LTE symbol with maximum bandwidth of 19.8 MHz. Furthermore, each pulse is unique in containing random simulated user data. Therefore, the simulation also contains the effects of clutter-Doppler spreading due to pulse-diverse waveforms [45]–[47]. However, the set of random pulses are the same across transmitters in to compare emitters.

A ground moving target was simulated at $11,250$ different locations on the global x-y plane as illustrated in Figure 4.6. At each location, all antennas from the six transmitters and one receiver were directed toward the target location. Changing the antenna directivity assisted in removing the de-

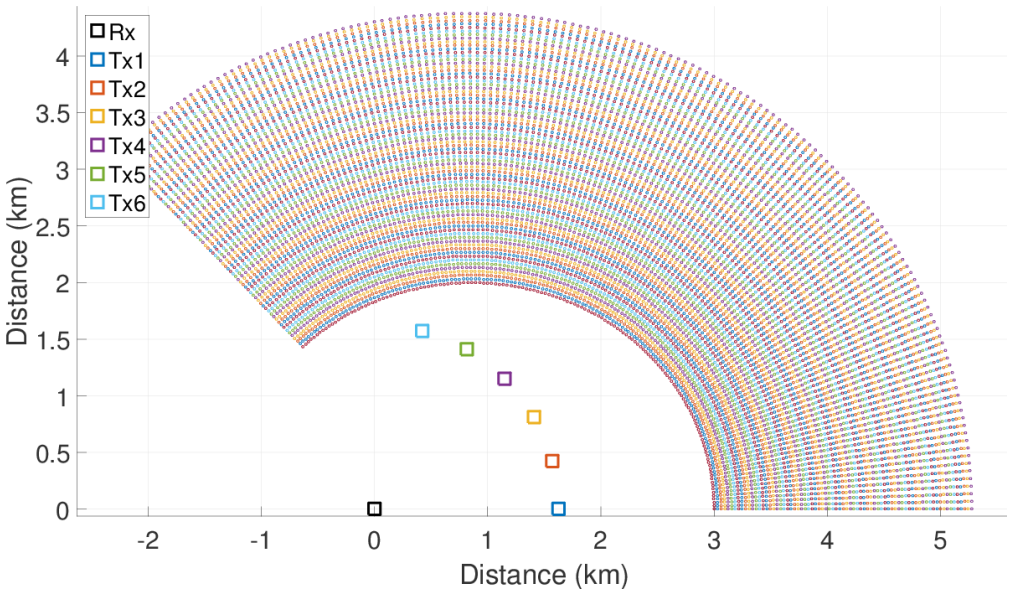

Figure 4.6: The set of spatial points where a ground moving target was simulated. The data points lie on isorange contours for transmitter 1.

pendency of antenna patterns and due to side-looking configuration, the receiver maintained a zero spatial frequency with the simulated target across all spatial data points . In turn, the total target Doppler shift at each location depended only on the Doppler shift caused by the moving target, $\bar{f}_{tgt}$.

The spatial data points consisted of 75 isorange contours for transmitter number one (Tx1) that were spaced at every eight range resolution cells. Next the isorange contour arc length of 135° was divided into 150 equal delta arc lengths; therefore, the total number of spatial data points became $75(150) = 11,250$. This method of spatial sampling allowed for a more uniform spatial distribution along the Tx1 isorange contours.

The set of velocity data points consisted of only unambiguous velocities to avoid Doppler aliasing. Therefore, the requirement is $|\bar{f}_{tgt}| \leq 0.5$. From

(3.16), this requirement becomes

$$v_{tgt} \leq \frac{\lambda f_r}{4}, \tag{4.6}$$

where $v_{tgt} = |\mathbf{v_{tgt}}|$. Furthermore, the receive platform is defined by a uniform linear array (ULA) of half-wavelength elemental spacing, and a clutter ridge slope from (3.13) of $\eta = 1$. This definition fixes the platform velocity as $v_a = f_r d = {}^{\lambda f_r}/_2$, which makes (4.6) become

$$v_t \leq \frac{v_a}{2}. \tag{4.7}$$

Therefore, the velocity magnitude became a set of 100 linearly spaced speeds from zero to ${}^{v_a}/_2$, while the velocity direction was a set of 360 angles ranging from 0° to 359°. The combination of the sets of magnitude and direction created a unique set of uniformly distributed velocity vectors of size $360(99) + 1 = 35,641$.

The ideal SINR for each transmitter at every spatial data point for the zero spatial frequency cut was linearly sampled at 501 Doppler frequencies from -0.5 to 0.5 at increments of 0.002. Then $\bar{f}_{tgt}$ was calculated for the set of velocity vectors at each spatial data point for each transmitter. Last, solving for the metrics and their findings shall be presented in the next sec-

tion. Table 4.1 lists the remaining simulations parameters as well as the ones previously discussed.

Table 4.1: Simulation Parameters

Number of Transmitters		6
Transmit Power		1000 W
Number of Channels		8
Number of Pulses		32
Height of Rx		1000 m
Height $\forall$ Tx		60 m
Baseline Separation $\forall$ Tx		1.88 km
Elevation Angle $\forall$ Tx		$-30°$
Tx Azimuth:	Tx1	$0°$
	Tx2	$15°$
	Tx3	$30°$
	Tx4	$45°$
	Tx5	$60°$
	Tx6	$75°$
Spatial Data Points:	$R_{b,min,\text{Tx1}}$	4.7 km
	$R_{b,max,\text{Tx1}}$	9.2 km
	Total	11,250
Velocity Data Points:	$\lvert\bar{v}_{min}\rvert$	0 m/s
	$\lvert\bar{v}_{max}\rvert$	$v_a/2$
	$\angle v_{min}$	$0°$
	$\angle v_{max}$	$359°$
	Total	35,641

4.3 Results

This section shall show the performance of each transmitter across the spatial grid for each specific metric introduced in Section 4.1. Next, the optimal

transmitter at each data point will be illustrated for each metric. Finally, the analysis of the metrics shall be discussed.

4.3.1 Average SINR

Figure 4.7 depicts SINR_{Avg} across the spatial grid. The first noticeable feature is that the average behaves according to Cassini ovals that show constant SNR performance. This feature is attributed to the fact that the noise limited regions of the SINR curve (see Figure 2.8) skew the SINR average toward noise limited performance, or alternatively, SNR performance. Therefore, Tx6 understandably generates the largest average SINR due to the smallest range product, $R_R^2 R_T^2$. A second relatable item is that average SINR does a poor job in relaying areas of strong clutter power because the metric is skewed toward target Doppler shifts outside of the clutter notch. Therefore, this metric can be useful if a priori knowledge exists for high target Doppler shift.

4.3.2 Weighted SINR Average

Figure 4.8 illustrates SINR_{WA} throughout the spatial points. By effectively giving more weight toward smaller Doppler magnitudes, it is possible to see regions with more clutter power due to in-plane scattering (see Figure

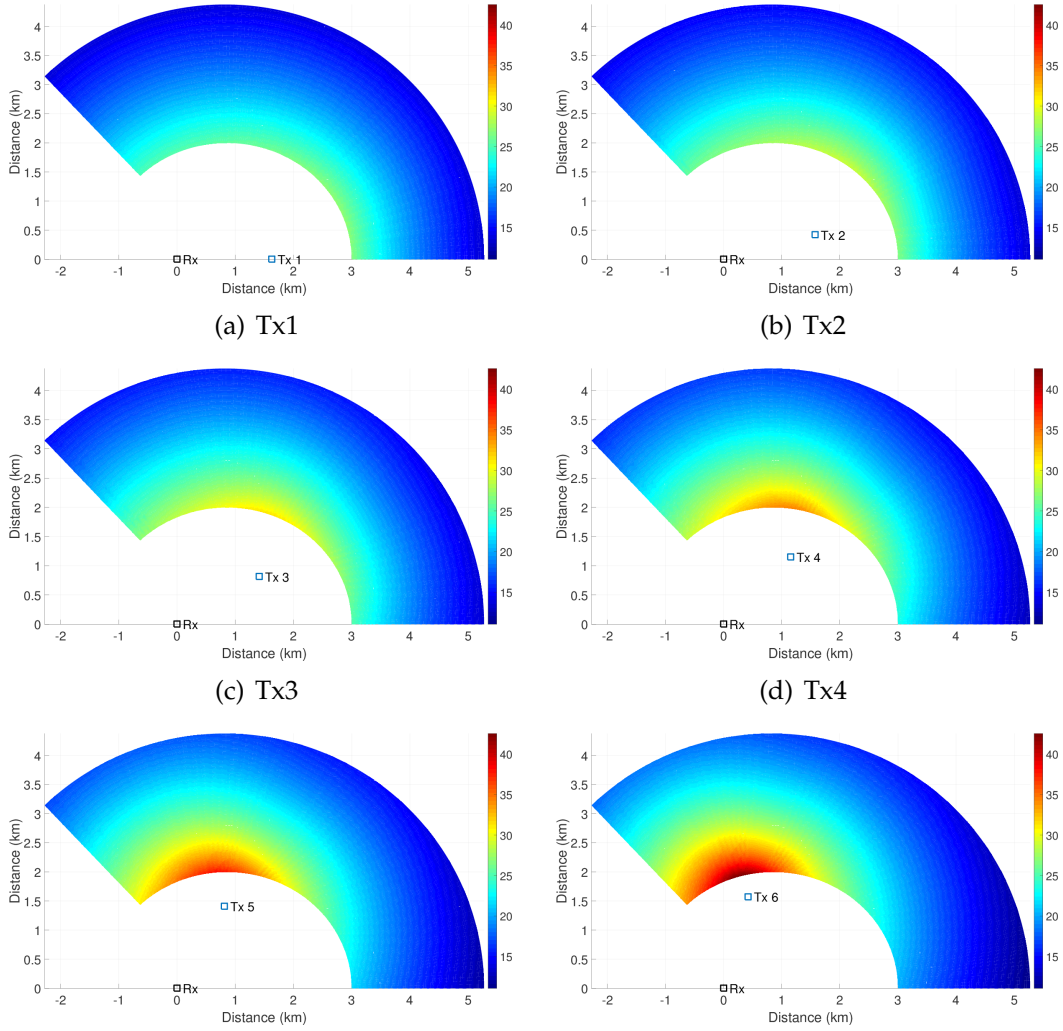

(a) Tx1 (b) Tx2

(c) Tx3 (d) Tx4

(e) Tx5 (f) Tx6

Figure 4.7: Average SINR at each spatial point for each transmitter.

3.10). Ultimately, this metric illustrates worse performance is seen when a target resides in the in-plane clutter scattering regions.

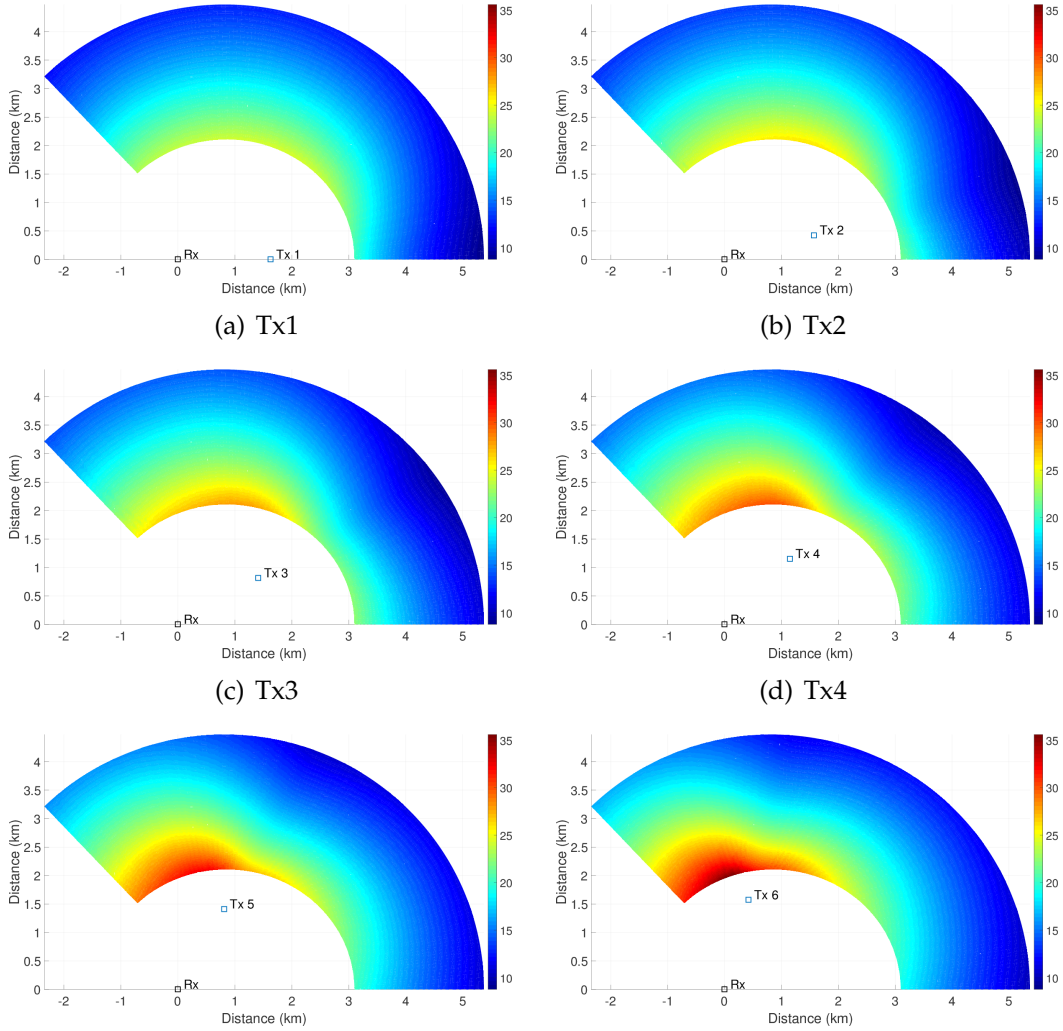

(a) Tx1 (b) Tx2

(c) Tx3 (d) Tx4

(e) Tx5 (f) Tx6

Figure 4.8: Weighted average SINR at each spatial point for each transmitter.

4.3.3 Minimum SINR

As discussed earlier, a maximin method can be used for optimal emitter selection. Therefore, Figure 4.9 illustrates SINR_{Min} across all Doppler frequencies over the spatial grid for each transmitter. Figure 4.9 mimics some of the behavior from the UVSF metric in Figure 4.10, but it discriminates be-

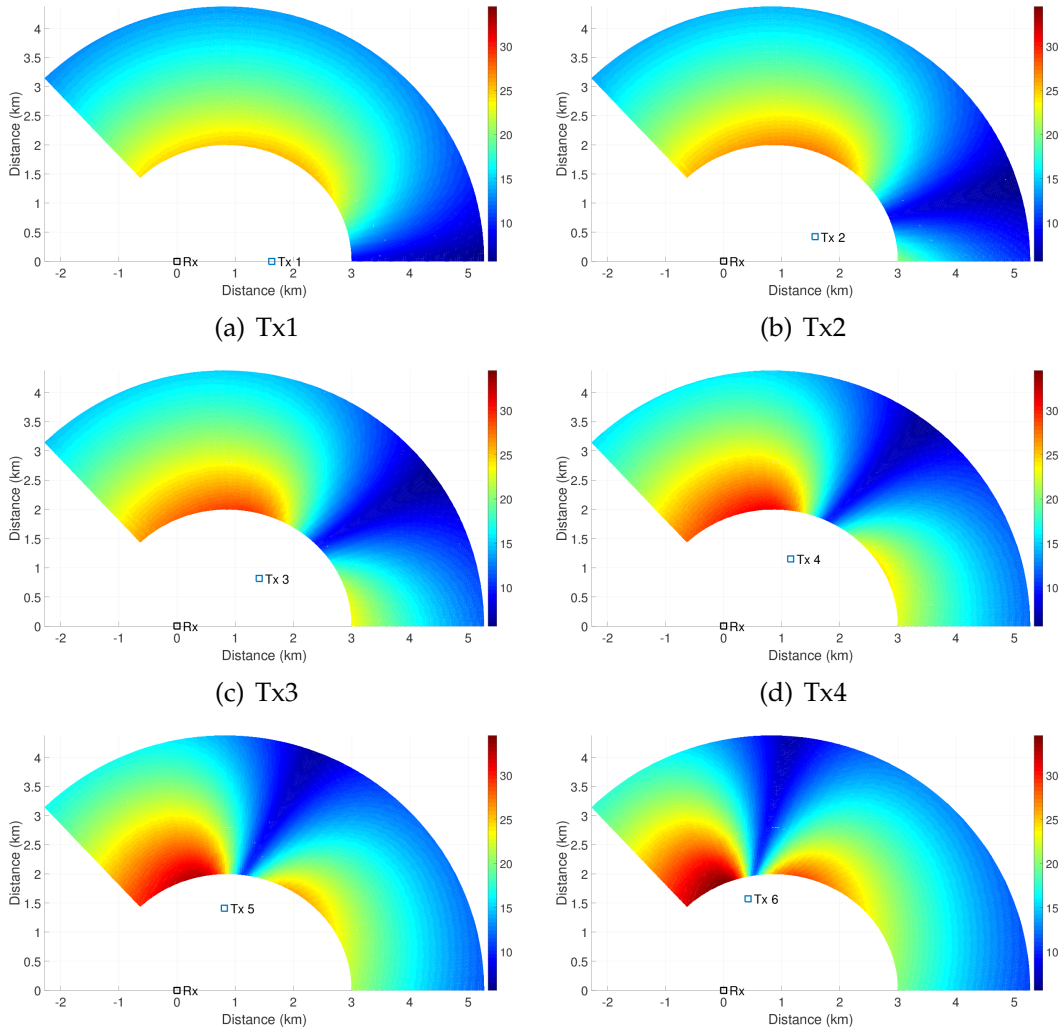

(a) Tx1 (b) Tx2

(c) Tx3 (d) Tx4

(e) Tx5 (f) Tx6

Figure 4.9: Minimum SINR at each spatial point for each transmitter.

tween transmitters in overlapping regions where UVSF equals one or zero. Again, more clutter power is seen in regions that are in-plane.

4.3.4 UVSF

Figure 4.10 depicts the performance of each transmitter for the UVSF metric. The sharp dropoff (most easily seen in Figure 4.10f) in UVSF occurs when the entire SINR curve dips below the threshold, which equates to UVSF $= 0$. In other words, the SNR is too weak due to the $R_R^2 R_T^2$ product from (2.18). In turn, the UVSF region where UVSF > 0 are shaped as a Cassini oval.

In regions of out-of-plane scattering, the entire SINR curve can rise above the DT and results in UVSF $= 1$. Unfortunately, when regions of UVSF $= 1$ overlap across multiple transmitters, the UVSF metric cannot down-select to an optimal emitter. Therefore, a second step is needed when such a situation arises.

4.3.5 Comparison

Taking Figures 4.7-4.10 and selecting the best performing transmitter at each spatial point leads to Figure 4.11. The first column consisting of (a), (c), and (e) shows SINR_{Avg}, SINR_{WA}, and SINR_{Min}, respectively. Then the second column of (b), (d), and (f) uses UVSF to perform an initial down-select that is followed by average SINR (UVSF_{Avg}), weighted average SINR (UVSF_{WA}), and minimum SINR (UVSF_{Min}), respectively. For spatial regions where the UVSF metric is unique for each transmitter, then the emitter decision is based solely on the emitter with maximum UVSF. If regions exist where

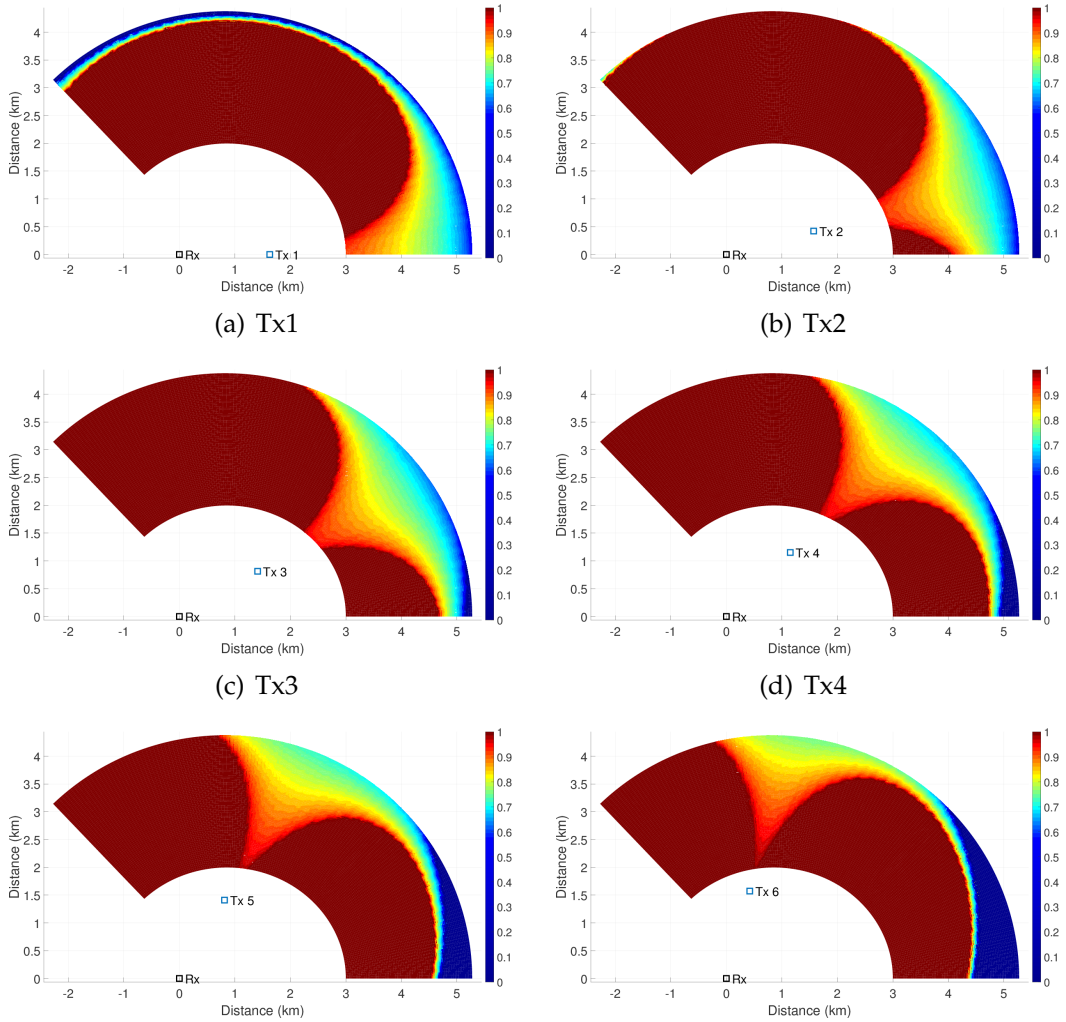

(a) Tx1 (b) Tx2

(c) Tx3 (d) Tx4

(e) Tx5 (f) Tx6

Figure 4.10: UVSF at each spatial point for each transmitter.

all six transmitters exhibit a zero UVSF (e.g. the entire SINR curve is below the DT), then no transmitter is selected.

By first focusing on subfigure (a), it can be seen that in-plane scattering influences the transmitter selection for SINR_{Avg}. It is easiest to see in the in-plane scattering regions for either Tx1 or Tx6 where SINR_{Avg} selects Tx2 and Tx5, respectively. However, when comparing Figure 4.11a with the rest of

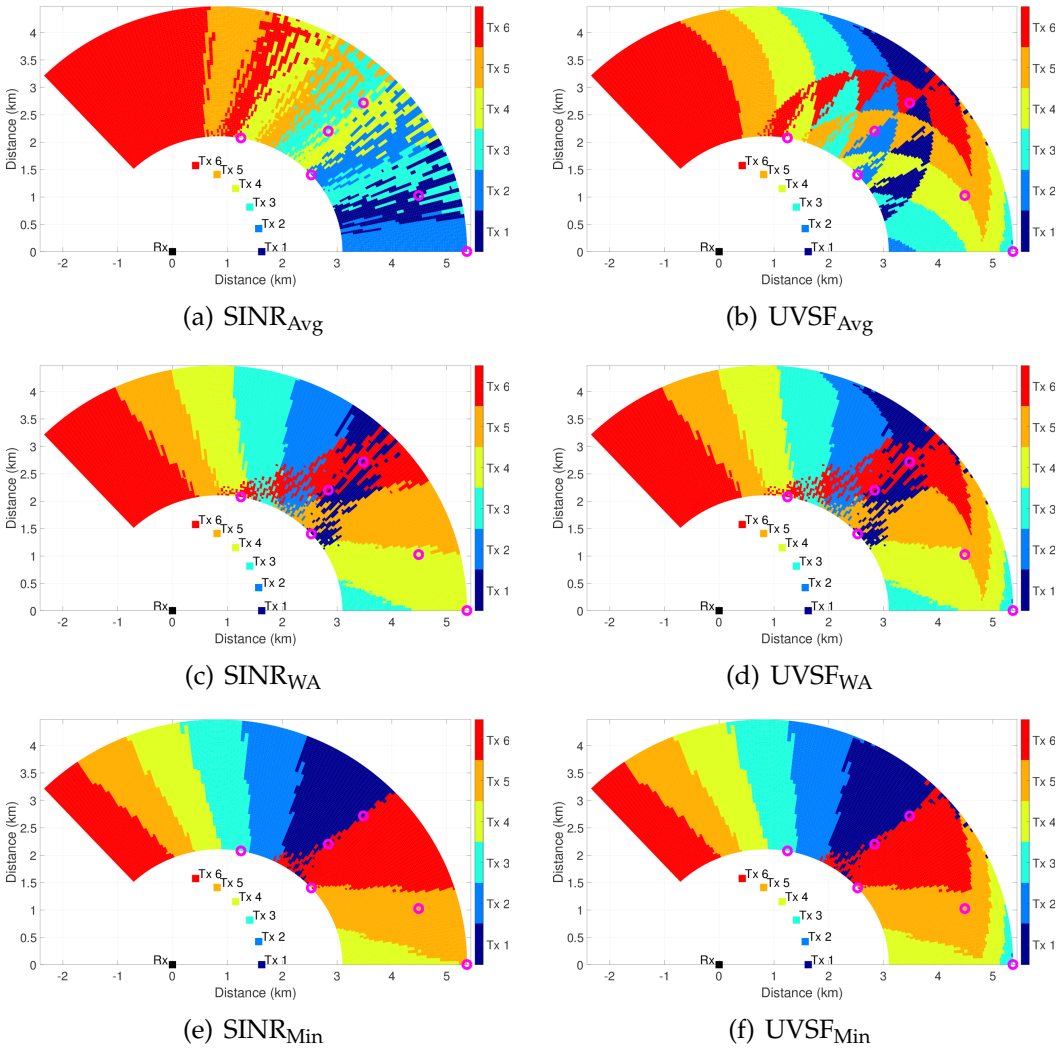

(a) SINR_{Avg} (b) UVSF_{Avg}

(c) SINR_{WA} (d) UVSF_{WA}

(e) SINR_{Min} (f) UVSF_{Min}

Figure 4.11: Optimal transmitter over the spatial grid using each of the described metrics.

the subfigures, it can be seen that the clutter power influences the SINR_{Avg} emitter selection the least. For example, the in-plane scattering region for Tx1 runs along the x-axis and SINR_{Avg} chooses Tx2, which is the adjacent emitter. However, SINR_{WA} selects either Tx3 or Tx4 (depends where on the x-axis) and SINR_{Min} selects either Tx4 or Tx5. Therefore, the SINR_{Avg} places

the least emphasis on clutter power because the in-plane scattering regions where the majority of the clutter power resides is the most narrow with SINR_{Avg}. Therefore, slow-moving targets may go undetected if the clutter notch is below the DT.

In subfigure (b), the UVSF_{Avg} metric promotes detectable SINR across Doppler frequencies, and then uses the average SINR to further distinguish between the remaining transmitters. It could be hypothesized that for an unknown target with a two dimensional uniform velocity distribution, or alternatively a $\bar{f}_{tgt}$ distribution depicted in Figure 4.1, the SINR_{Avg} metric would be inferior to the UVSF_{Avg} when pertaining to probability of detection. This hypothesis is due to the fact that approximately 50% of the velocities lie within the clutter region of the SINR curve. However, if a priori knowledge of a fast moving target existed, then SINR_{Avg} could perform better when a target's RCS is small.

In subfigure (c) the SINR_{WA} metric places more emphasis on the clutter region of the SINR curve, which in turn, places more emphasis on detecting slow moving targets. Likewise, the UVSF_{WA} metric also inherently emphasizes small Doppler shifts. Therefore, the UVSF_{WA} in subfigure (d) does not differ significantly from (c) across the spatial grid. These differences will be further discussed in the next section.

For subfigure (e), the SINR_{Min} emitter selection method ultimately down selects to the transmitter that contains a combination of the lowest clutter power present and the smallest bistatic range product, $R_R^2 R_T^2$. As an example, if the bistatic range product of transmitter A is less than transmitter B, but more clutter power is present in transmitter A, then the clutter notch of transmitter A could extend below that of transmitter B. Therefore, the SINR_{Min} selects transmitter B. The problem with this metric is that there is no sanity check against the DT. The entire SINR curve of transmitter B from the previous example could fall below the DT while only a portion of the notch from transmitter A might fall below the threshold. Therefore, it can be hypothesized that UVSF_{Min} out performs SINR_{Min} from a probability of detection point of view when assuming the previous described scenario.

4.3.6 Analysis

Figure 4.12 illustrates the SINR curves for all six transmitters for six different spatial data points that are depicted by the magenta circles in Figure 4.11. The first subfigure is labeled (a) and is for the spatial point located at $(2.5\,\text{km}, 1.4\,\text{km})$. The chosen transmitters are Tx2 for SINR_{Avg}, Tx1 for SINR_{WA}, and Tx5 for SINR_{Min}. Each of the UVSF metrics produce the same selection as if UVSF was not considered. Therefore, UVSF must have been equal to one for at least Tx2, Tx1, and Tx5. In (a) is can first be seen that

only Tx3 produces a UVSF of less than one, which explains the repeated selection pattern.

In subfigure (b) the spatial point is located at $(2.8\text{ km}, 2.2\text{ km})$. The chosen transmitters are Tx3 for SINR_{Avg}, Tx6 for SINR_{WA}, Tx1 for SINR_{Min}, Tx5 for UVSF_{Avg}, Tx6 for UVSF_{WA}, and Tx1 for UVSF_{Min}. When taking the DT into account, only Tx1, Tx2, Tx5, and Tx6 should be considered. Therefore, the average SINR method chose an unfavorable transmitter for this scenario.

For subfigure (c), the SINR curves are for the spatial location of $(4.5\text{ km}, 1.0\text{ km})$. The chosen transmitters are Tx1 for SINR_{Avg}, Tx4 for SINR_{WA}, Tx5 for SINR_{Min}, and Tx5 for all UVSF metrics. This location is interesting because only Tx5 and Tx6 are above the DT for all Doppler frequencies ($\text{UVSF} = 1$). Therefore, this is a case where the SINR_{WA} metric does not place enough emphasis toward clutter power. Even though Tx4 achieved the best average within the clutter region, there are Doppler frequencies where SINR fall below the DT. Overall, the UVSF metrics appear to have selected the best transmitter, Tx5, for this scenario.

Subfigure (d) compares the SINR curves at the location $(1.3\text{ km}, 2.1\text{ km})$, which is the shortest R_R range of any of the points. The chosen transmitters are Tx5 for SINR_{Avg}, Tx6 for SINR_{WA}, Tx3 for SINR_{Min}, Tx4 for UVSF_{Avg}, Tx6 for UVSF_{WA}, and Tx3 for UVSF_{Min}. Such a short range causes SINR

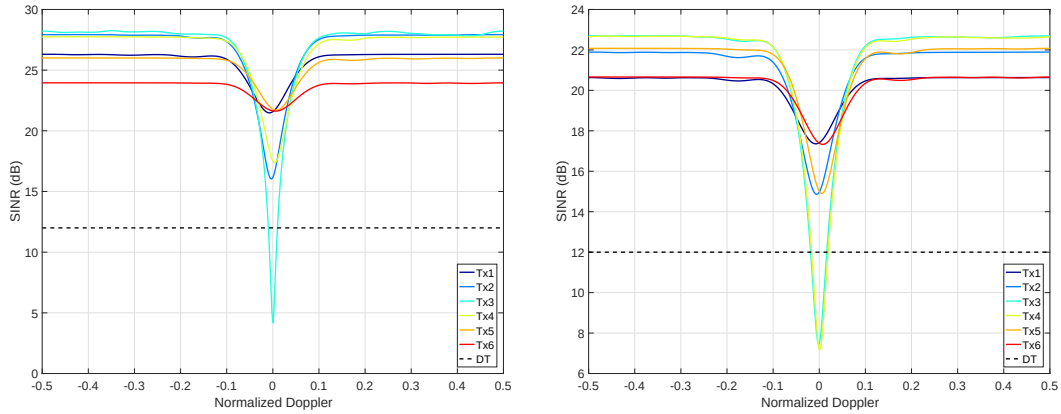

(a) $(2.5\text{ km}, 1.4\text{ km})$ (b) $(2.8\text{ km}, 2.2\text{ km})$

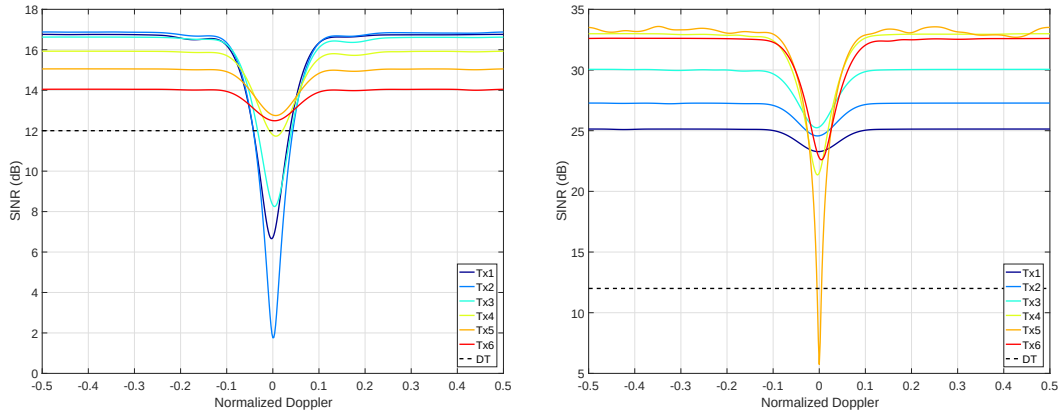

(c) $(4.5\text{ km}, 1.0\text{ km})$ (d) $(1.3\text{ km}, 2.1\text{ km})$

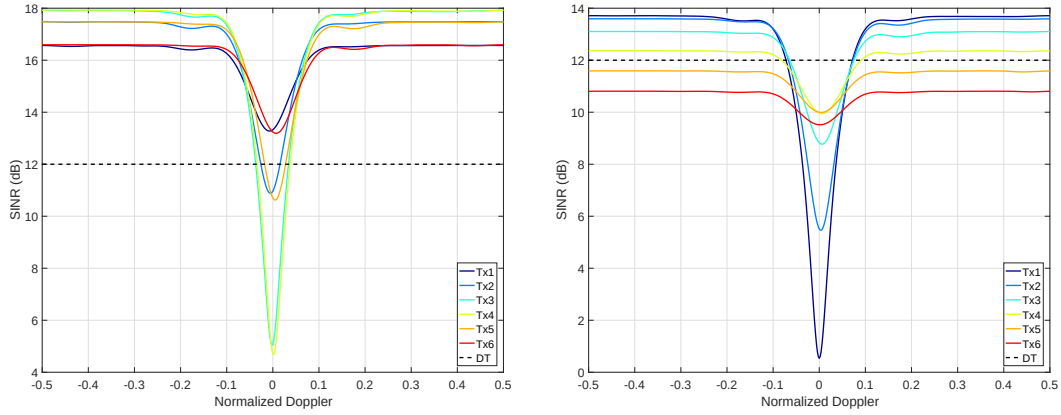

(e) $(3.5\text{ km}, 2.7\text{ km})$ (f) $(5.4\text{ km}, 0.0\text{ km})$

Figure 4.12: All six SINR curves compared to the DT at the six labeled locations.

curves that reside far above the DT. This location is in-plane with Tx5, which suggests very large clutter power returns. These large returns are seen in two ways. First, the clutter notch depth is almost 30 dB, which is the most loss for any SINR curves depicted in Figure 4.12. Second, the CDS is easily visible across Doppler frequencies. This case highlights how skewed the SINR_{Avg} can be because the metric chose an emitter with the most loss or clutter power. When taking UVSF into consideration, only Tx5 is removed (UVSF < 1), while the remaining transmitters are tied at UVSF metrics of one. From these remaining emitters, Tx3 appears to be the best overall due to high SINR performance across all Doppler frequencies. Both, SINR_{Min} and UVSF_{Min} chose Tx3.

Subfigure (e) illustrates the transmitter performances at location $(3.5$ km, 2.7 km$)$. The chosen transmitters are Tx4 for SINR_{Avg}, Tx1 for SINR_{WA}, Tx1 for SINR_{Min}, Tx6 for UVSF_{Avg}, Tx1 for UVSF_{WA}, and Tx1 for UVSF_{Min}. At this location is only Tx1 or Tx6 should be considered because their SINR curves are over the DT entirely. Furthermore, Tx1 and Tx6 appear almost identical except for the skewed notches. The notch for Tx1 exhibits higher clutter power in negative Doppler shifts while the notch for Tx6 is skewed toward positive Doppler frequencies. This case highlights how the metrics only consider SINR values and not the frequencies that experience the most loss. With nearly identical SINR curves, there could be scenarios where Tx6

is best. Therefore, a possible solution would be to down select to multiple emitters when metrics are within a small user defined tolerance.

Subfigure (f) depicts the SINR curves for the spatial point $(5.4\,\text{km}, 0.0\,\text{km})$, which is the longest R_R range of any of the considered locations. The chosen transmitters are Tx2 for SINR_{Avg}, Tx4 for SINR_{WA}, Tx5 for SINR_{Min}, and Tx2 for all UVSF. In this instance, the UVSF value is unique across transmitters, and not a single transmitter has a UVSF of zero or one. Thus, all UVSF metrics agree because the second down selection method is never reached. Interestingly is how SINR_{Avg} agreed with the UVSF metrics since the metrics differ in where they emphasize clutter power. Since the clutter notch is the first point that can dip below a DT, UVSF inherently places emphasis on the clutter region. However, it has been shown over multiple examples how SINR_{Avg} is skewed more toward the noise limited regions. Another interesting feature is how the UVSF for Tx5 is zero, yet the SINR_{Min} metric selects Tx5. This is a case were no sanity check against a DT occurs.

A summary of chosen transmitters for each spatial point can be found in Table 4.2. Overall, the selection process depends first on whether or not to consider a DT. A DT can be arbitrary at times due to the dependence the SINR curve has on an unknown target's RCS. The stronger the return from the target, then the higher the SINR curve and in turn UVSF. Likewise, for low target RCS values the UVSF could become zero. Thus, for optimal

Table 4.2: Selected Transmitters for High/Low Target RCS

Location (m)		$SINR_{Avg}$	$SINR_{WA}$	$SINR_{Min}$	$UVSF_{Avg}$	$UVSF_{WA}$	$UVSF_{Min}$
x	y						
2534	1399	2/2	1/1	5/5	2/4	1/1	5/5
2845	2197	3/3	6/6	1/1	5/6	6/6	1/1
4493	1022	1/1	4/4	5/5	5/2	5/2	5/2
1252	2075	5/5	6/6	3/3	4/4	6/6	3/3
3485	2713	4/4	1/1	1/1	6/4	1/4	1/4
5372	0	2/2	4/4	5/5	2/NA	2/NA	2/NA

transmitter selection for unknown targets, it may not be wise to consider a metric that contains an underlying dependence on a target's RCS.

However, if an assumption on target size can be made, then UVSF can assist in emitter selection. As an example, Figure 4.13 repeats the emitter selection process for only the UVSF metrics for a target with a low RCS assumption. It is now clear how UVSF relies on the size of a target's RCS.

In a scenario where a small target exists, UVSF can be beneficial for knowing where performance is lacking. If there is a desire to search a spatial grid with a zero UVSF, then possibly either the receiver platform's flight path could be altered to give a favorable UVSF or the number of pulses could be increased to achieve higher processing gain. Another benefit from

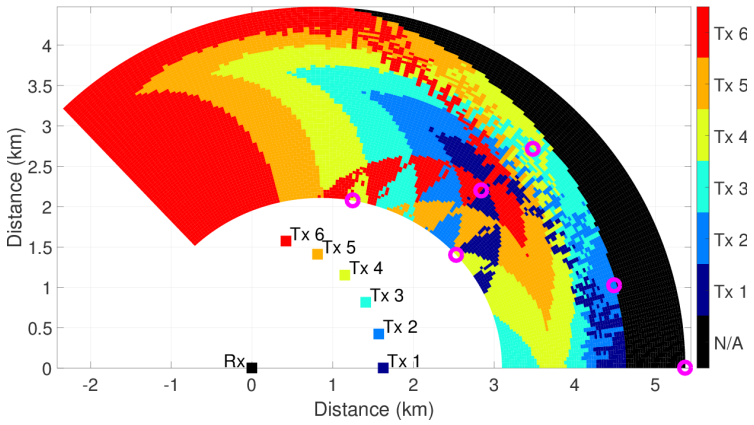

(a) UVSF_{Avg}

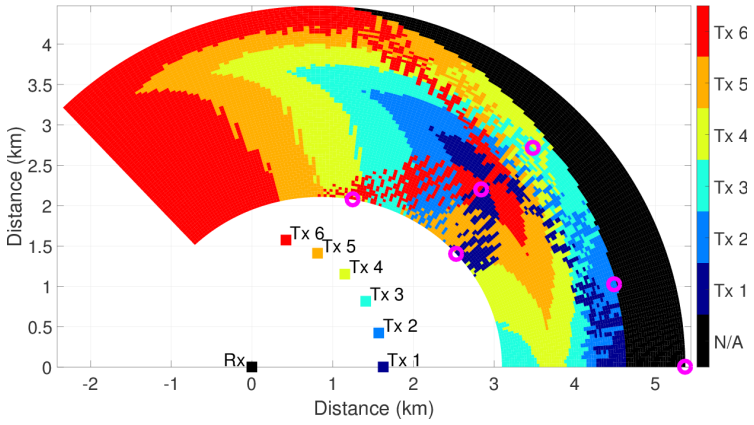

(b) UVSF_{WA}

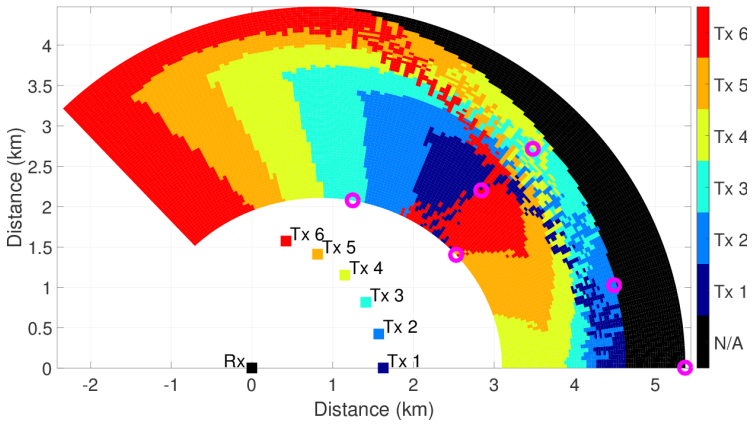

(c) UVSF_{Min}

Figure 4.13: Optimal emitter using UVSF over the spatial grid with a small target assumption.

UVSF is the search grid can be optimized for the relative locations of the receiver and transmitters, thus, limiting waste of computational resources. In other words, if a region shows a UVSF of zero for all transmitters, then exclude the region from the search grid.

On the other hand, if an assumption for a target's RCS cannot be made, then the metrics that do not use UVSF could be the optimal method for emitter selection. This is due to the fact that the non-UVSF metrics rely on relative performance differences for transmitter selection, which can be seen in Table 4.2. Notice the selected transmitters for the non-UVSF metrics do not vary between high and low target RCS values. This is because the non-UVSF metrics are rating transmitters based on the relative bistatic geometries for an assumed isotropic scattering target. Thus, for unknown targets it can be proposed that optimal metrics should be limited to either SINR_{Avg}, SINR_{WA}, or SINR_{Min}.

Furthermore, it can be argued that either SINR_{WA} or SINR_{Min} should be considered for transmitter selection for a target with unknown properties. While it may not be wise to use UVSF for selecting transmitters when no a priori knowledge exists, the same could be said for using the SINR_{Avg} metric. As previously shown, the SINR_{Avg} metric can be biased to transmitters with strong clutter notches because the spatial points with more clutter power contain attributes of being in plane with the receiver and transmit-

ter. This low out-of-plane angle can in turn lead to a transmitter with the minimum $R_R^2 R_T^2$ distance. Furthermore, a minimum range product causes the maximum SINR at high Doppler frequencies. Therefore, SINR_{Avg} can be biased towards high SINR at large Doppler frequencies because of the minimum $R_R^2 R_T^2$ that occurs at the spatial frequencies where more clutter power exists. Then depending on the target's RCS, there could be anywhere from a few to many two-dimensional target velocities that become undetectable.

Finally, another simulation was conducted with the same setup, but a large clutter discrete (LCD) was placed at $(3315 \text{ m}, 657 \text{ m})$. In short, an LCD contaminates the received data and can cause false alarms and missed detections. The presence of the discrete was most apparent for the SINR_{WA}, SINR_{Min}, and UVSF metrics. Figure 4.14 illustrates the UVSF for each transmitter. In particular, the loss in performance from the LCD is most noticeable for subfigures (d), (e), and (f) where UVSF < 1 in the vicinity of the discrete. However, take note how the impact is minimal when the LCD lies in-plane with a transmitter as in Figure 4.14a. The next chapter formally defines an LCD and will look to exploit this out-of-plane observation in order to detect, estimate, and remove the LCD from the received data.

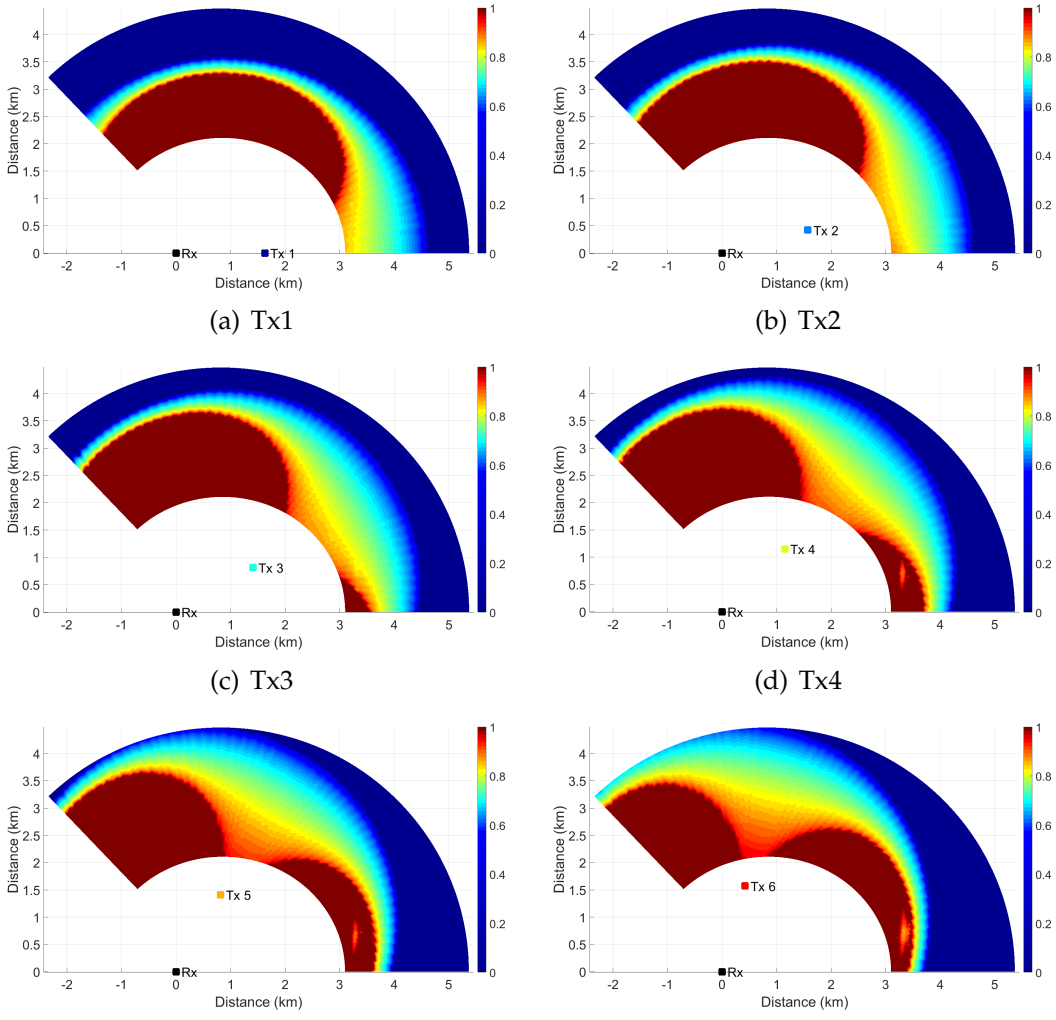

(a) Tx1 (b) Tx2

(c) Tx3 (d) Tx4

(e) Tx5 (f) Tx6

Figure 4.14: UVSF at each spatial point for each transmitter for a low target RCS and an LCD present.

Chapter 5

Large Clutter Discrete Removal

5.1 Introduction

A large clutter discrete (LCD) is classified as a strong scattering clutter return that is spatially localized. The performance impact from LCDs depends on where in range the LCD resides. If an LCD exists in the CUT, then a false alarm can likely appear at the discrete's angle-Doppler location. If an LCD exists in the training data from (5.29), then over-nulling occurs in the CUT at the discrete's angle-Doppler frequency, which can result in a degradation in moving target detection. Therefore, it is desirable to remove LCDs from a data cube no matter where they reside in range. The first step is to detect an LCD and this detection will be covered in Section 5.2. Then Section 5.3 details different estimation techniques that will be used to estimate the LCD parameters (e.g. spatial/Doppler frequencies and complex

amplitude). Then the complete algorithm will be laid out in Section 5.4 and followed up by results in Section 5.5.

5.2 LCD Detection

Detecting an LCD is accomplished through the use of a two-dimensional cell-averaging constant false alarm rate (CA-CFAR) detector. In a CA-CFAR detector, an adaptive threshold is used for hypothesis testing where the null hypothesis, H_0, does not contain an LCD and the alternative hypothesis, H_1, contains an LCD. The adaptive threshold is calculated from the arithmetic mean of the surrounding interference levels in range and spatial/Doppler frequency [76].

First a range versus clutter ridge image is generated by calculating the clutter spectral energy, $\mathbf{X}$, along the clutter ridge for all range bins in the data cube. The spectral energy at the k^{th} range bin is calculated as

$$\mathbf{X_k}[\hat{\vartheta}, \hat{\bar{f}}_d] = \mathbf{s}^{\mathrm{H}} \hat{\mathbf{R}}_\mathbf{k} \mathbf{s}, \tag{5.1}$$

where the hypothesized spatial and Doppler frequencies, $\hat{\vartheta}$ and $\hat{\bar{f}}_d$, are dictated by (3.12). The estimated clutter covariance matrix, $\hat{\mathbf{R}}_\mathbf{k}$, is

$$\hat{\mathbf{R}}_\mathbf{k} = \frac{1}{P} \sum_{|p-k| \not\leq g} \mathbf{x_p} \mathbf{x_p}^{\mathrm{H}}, \tag{5.2}$$

where P and g are the total number of training cells and number of guard cells, respectively. Furthermore, P must satisfy the RMB rule of $P \approx 2NM$ [63].

5.3 LCD Estimation

Spectrum estimation techniques can be classified into two categories, nonparametric and parametric. Both can be used for either temporal or spatial estimations. If a received signal is sampled over time with a known sampling frequency, then a temporal estimation produces a power spectral density (PSD) that portrays the distribution of signal power over frequency [77]. If an array of sensors is deployed with all sensor locations known, then spatial sampling is accomplished by capturing snapshots of the signal from all sensors at the same instant in time. With these snapshots, a spatial estimation can be accomplished to generate a PSD that relates the distribution of signal power over spatial frequency [78].

Again, both temporal and spatial estimation techniques fall into either nonparametric or parametric categories. In general, nonparametric methods do not contain any assumptions about the received data, $x[t]$, except that the data sequence comes from a wide-sense stationary random process [79]. Some nonparametric temporal estimation examples include, correlogram, periodogram, Blackman-Tukey, Bartlett, Welch, Capon, and Ampli-

tude and Phase Estimation (APES). Examples of nonparametric spatial estimators consist of primarily beamforming, Capon, and APES.

If a method assumes that $x[t]$ behaves according to a particular parametric model, then said method is classified as a parametric estimation technique. Accuracy of parametric models is only as good as the accuracy of the assumptions/behavior of the signal of interest. If little *a priori* knowledge exists about $x[t]$, then performance from parametric methods will most likely suffer. Therefore, only nonparametric models were considered for estimating the signal parameters of the LCD.

To effectively remove an LCD from the data cube, the signal parameters of spatial/Doppler frequency and the complex amplitude must first be estimated. The two examined estimation techniques are Capon [80] and Amplitude and Phase Estimation (APES) [81]. It has been shown that the Capon method achieves higher resolution and more accuracy than APES for estimating signal frequency in the presence of noise [77], [82]. However, when accurate frequency estimates exist, APES outperforms Capon in estimating complex amplitude [77], [83]. Therefore, the Capon is used to estimate an LCD's spatial/Doppler frequency, followed by APES for estimating the complex amplitude of the LCD. This combined method is known as CAPES (Capon-APES) [84].

Furthermore, when estimating amplitude, Capon and APES can be interpreted as solutions to a weighted least-squares (WLS) problem. However, when estimating the PSD, the methods are more easily interpreted as matched-filterbank (MAFI) approaches [85], [86]. As will be seen, the two methods differ in their chosen weights/filters.

The next section will first introduce the WLS framework for a one dimensional signal/dataset. Then, the Capon MAFI power estimator will be derived. Next, the Capon and APES solutions for estimating complex amplitude will be given. Finally, the Capon and APES methods will be extended for a two-dimensional signal as is representative in STAP datasets.

5.3.1 Weighted Least-Squares Signal Framework

Let an arbitrary one-dimensional time series be represented as $x[m]$ where $0 \leq m < M-1$. At a given frequency, ω, $x[m]$ can be written as

$$x[m] = \alpha(\omega)e^{j\omega m} + w_\omega[m], \tag{5.3}$$

where $\alpha(\omega)$ is a complex amplitude and $w_\omega[m]$ is a residual term that represents both random noise and other signals not at ω. Also assume the M samples are uniformly spaced in time. Let $\mathbf{y}_k$ be a subsequence of length L of the received data, $x[m]$ where k represents the k^{th} subsequence. Finally,

arrange all possible subsequences in a matrix $\mathbf{Y}$ such that

$$\mathbf{Y} \stackrel{\text{def}}{=} [\mathbf{y}_0 \cdots \mathbf{y}_{K-1}] \stackrel{\text{def}}{=} \begin{bmatrix} x[0] & x[1] & \cdots & x[K-2] & x[K-1] \\ x[1] & x[2] & & x[K-1] & x[K] \\ \vdots & & \ddots & & \vdots \\ x[L-2] & x[L-1] & & x[M-3] & x[M-2] \\ x[L-1] & x[L] & \cdots & x[M-2] & x[M-1] \end{bmatrix} \tag{5.4}$$

where $K = M - L + 1$ is the total number of subsequences.

The residual term in (5.3) can be defined in matrix form as

$$\mathbf{W}(\omega) = \begin{bmatrix} \mathbf{w}_0(\omega) & \dots & \mathbf{w}_{K-1}(\omega) \end{bmatrix}, \tag{5.5}$$

where $\mathbf{w}_k(\omega)$ is a length L subsequence of $w_\omega[m]$ that is staggered in the same method as (5.4). Let $\mathbf{a}_P(\omega)$ be defined as a steering vector of length P such that

$$\mathbf{a}_P(\omega) \stackrel{\text{def}}{=} \begin{bmatrix} 1 \\ e^{j\omega} \\ \vdots \\ e^{j(P-1)\omega} \end{bmatrix}. \tag{5.6}$$

Using (5.6), the linearly progressing phasor in (5.3) can be represented as an outer product between two steering vectors of specific lengths given as

$$\mathbf{A}(\omega) = \mathbf{a}_L(\omega)\mathbf{a}_K^{\mathrm{T}}(\omega). \tag{5.7}$$

Finally, (5.4) can be written as

$$\mathbf{Y} = \alpha(\omega)\mathbf{A}(\omega) + \mathbf{W}(\omega). \tag{5.8}$$

In estimation theory, the data model in (5.8) is known as a linear model [87]. It can be seen that the data in $\mathbf{Y}$ are observed after the parameter of interest, $\alpha(\omega)$, is operated upon by $\mathbf{A}(\omega)$. The linear signal model is the easiest to work with and the basis for nearly all practical algorithms [88]. In particular, a WLS estimate, $\hat{\alpha}(\omega)$ can be calculated by minimizing

$$\begin{aligned} J(\alpha(\omega)) &= \mathrm{Tr}\left\{ \left[\mathbf{Y} - \alpha(\omega)\mathbf{A}(\omega)\right]^{\mathrm{H}} \mathbf{\Phi} \left[\mathbf{Y} - \alpha(\omega)\mathbf{A}(\omega)\right] \right\} \\ &= \mathrm{Tr}\left\{\mathbf{Y}^{\mathrm{H}}\mathbf{\Phi}\mathbf{Y}\right\} - \alpha(\omega)\mathrm{Tr}\left\{\mathbf{Y}^{\mathrm{H}}\mathbf{\Phi}\mathbf{A}(\omega)\right\} - \alpha^*(\omega)\mathrm{Tr}\left\{\mathbf{A}^{\mathrm{H}}(\omega)\mathbf{\Phi}\mathbf{Y}\right\} \\ &\quad + \alpha^*(\omega)\alpha(\omega)\mathrm{Tr}\left\{\mathbf{A}^{\mathrm{H}}(\omega)\mathbf{\Phi}\mathbf{A}(\omega)\right\}, \end{aligned} \tag{5.9}$$

where $\mathbf{\Phi}$ is a symmetric positive definite weighting matrix. Since (5.9) is quadratic in $\alpha(\omega)$, the minimum can be found by setting the derivative with respect to $\alpha(\omega)$ equal to zero. In order to take the complex derivative of a

real scalar function, J, with respect to the complex amplitude, the Wirtinger derivative is employed (see Appendix A) [89]. Furthermore, the optimization can be accomplished through either $\partial/\partial\alpha$ or $\partial/\partial\alpha^*$. The more advantageous operator depends on the actual cost function being optimized. When quadratic functions like (5.9) are considered, the $\partial/\partial\alpha^*$ operator is preferable [90] and (5.9) becomes

$$\frac{\partial J(\alpha(\omega))}{\partial \alpha^*(\omega)} = -\mathrm{Tr}\left\{\mathbf{A}^{\mathrm{H}}(\omega)\mathbf{\Phi}\mathbf{Y}\right\} + \alpha(\omega)\mathrm{Tr}\left\{\mathbf{A}^{\mathrm{H}}(\omega)\mathbf{\Phi}\mathbf{A}(\omega)\right\} \tag{5.10}$$

Then, setting (5.10) equal to zero and solving for the amplitude leads to the WLS estimate of

$$\begin{aligned}
\hat{\alpha}(\omega) &= \frac{\mathrm{Tr}\left\{\mathbf{A}^{\mathrm{H}}(\omega)\mathbf{\Phi}\mathbf{Y}\right\}}{\mathrm{Tr}\left\{\mathbf{A}^{\mathrm{H}}(\omega)\mathbf{\Phi}\mathbf{A}(\omega)\right\}} \\
&= \frac{\mathrm{Tr}\left\{\mathbf{a}_K^*(\omega)\mathbf{a}_L^{\mathrm{H}}(\omega)\mathbf{\Phi}\mathbf{Y}\right\}}{\mathrm{Tr}\left\{\mathbf{a}_K^*(\omega)\mathbf{a}_L^{\mathrm{H}}(\omega)\mathbf{\Phi}\mathbf{a}_L(\omega)\mathbf{a}_K^{\mathrm{T}}(\omega)\right\}} \\
&= \frac{\mathbf{a}_L^{\mathrm{H}}(\omega)\mathbf{\Phi}\mathbf{Y}\mathbf{a}_K^*(\omega)}{\mathbf{a}_L^{\mathrm{H}}(\omega)\mathbf{\Phi}\mathbf{a}_L(\omega)\mathbf{a}_K^{\mathrm{T}}(\omega)\mathbf{a}_K^*(\omega)} \\
&= \frac{\mathbf{a}_L^{\mathrm{H}}(\omega)\mathbf{\Phi}\mathbf{g}(\omega)}{\mathbf{a}_L^{\mathrm{H}}(\omega)\mathbf{\Phi}\mathbf{a}_L(\omega)},
\end{aligned} \tag{5.11}$$

where $\mathbf{g}(\omega)$ is a column vector of length L defined as

$$\begin{aligned}
\mathbf{g}(\omega) &\stackrel{\text{def}}{=} \frac{1}{K}\sum_{k=0}^{K-1}\mathbf{y}_k e^{-j\omega k} \\
&= \frac{1}{K}\mathbf{Y}\mathbf{a}_K^*(\omega).
\end{aligned} \tag{5.12}$$

Equation (5.12) can be interpreted as a discrete-time short-time Fourier transform (STFT) for L windows of length K [91]. Furthermore, when the discrete-time STFT is computed for signals offset by one lag, as represented in $\mathbf{Y}$, then (5.12) can be efficiently implemented using the sliding discrete Fourier transform (SDFT) algorithm [92].

In the extreme case of $L = 1$, then $K = M$, $\mathbf{Y} = \mathbf{x}^{\mathrm{T}}$, $\mathbf{\Phi}$ disappears, and (5.11) reduces to the discrete Fourier transform (DFT)

$$\begin{aligned} \hat{\alpha}(\omega)_{DFT} &= \frac{\mathbf{x}^{\mathrm{T}}\mathbf{a}_M^*(\omega)}{\mathbf{a}_M^{\mathrm{T}}(\omega)\mathbf{a}_M^*(\omega)} \\ &= \frac{1}{M}\sum_{m=0}^{M-1} x[m]e^{-jm\omega}. \end{aligned} \tag{5.13}$$

In the case of $1 < L < N$ and $\mathbf{\Phi} = \mathbf{I}$ (independently weighted over ω), then the amplitude estimate becomes the averaged Fourier method and is equal to [82]

$$\begin{aligned} \hat{\alpha}(\omega)_{A-DFT} &= \frac{\mathbf{a}_L^{\mathrm{H}}(\omega)\mathbf{I}\mathbf{g}(\omega)}{\mathbf{a}_L^{\mathrm{H}}(\omega)\mathbf{I}\mathbf{a}_L(\omega)} \\ &= \frac{1}{L}\mathbf{a}_L^{\mathrm{H}}(\omega)\mathbf{g}(\omega) \\ &= \frac{1}{KL}\sum_{k=0}^{K-1}\sum_{l=0}^{L-1} x[k+l]e^{-j\omega(k+l)}. \end{aligned} \tag{5.14}$$

5.3.2 Capon Power Estimation

The easiest way to think about the Capon method for power estimation is as a MAFI approach [86]. The method generates a data-dependent bandpass filter at a frequency of interest, ω. From the bandpass filter, a power estimate at ω is generated from the solution of a minimization problem that is subject to linear constraints. Then, the process is repeated for all frequencies of interest to create the PSD [77].

For a filter of length L with an impulse response defined as

$$\mathbf{h} = [h_0 \; h_1 \; \ldots \; h_{L-1}]^{\mathrm{T}}. \tag{5.15}$$

The filtered output, y_F, of $\mathbf{y}_k$ is given as

$$\begin{aligned} y_F &= \sum_{l=0}^{L-1} h_l^* y_k[l] \\ &= \mathbf{h}^{\mathrm{H}} \mathbf{y}_k. \end{aligned} \tag{5.16}$$

Next, the filtered output power is defined as

$$\begin{aligned} E\left\{|y_F(t)|^2\right\} &= E\left\{\mathbf{h}^{\mathrm{H}} \mathbf{y}_k \mathbf{y}_k^{\mathrm{H}} \mathbf{h}\right\} \\ &= \mathbf{h}^{\mathrm{H}} E\left\{\mathbf{y}_k \mathbf{y}_k^{\mathrm{H}}\right\} \mathbf{h} \\ &= \mathbf{h}^{\mathrm{H}} \mathbf{R} \mathbf{h}, \end{aligned} \tag{5.17}$$

where $\mathbf{R}$ is the covariance matrix of $\mathbf{y}_k$ and formally defined as

$$\mathbf{R} \stackrel{\text{def}}{=} E\left\{\mathbf{y}_k \mathbf{y}_k^{\mathrm{H}}\right\}. \tag{5.18}$$

For an accurate estimate, the filter, $\mathbf{h}$, must not distort the signal information within the passband. The filter frequency response, $H(\omega)$, is given as

$$\begin{aligned} H(\omega) &= \sum_{l=0}^{L-1} h_l e^{-j\omega l} \\ &= \mathbf{a}_L^{\mathrm{H}}(\omega)\mathbf{h} = \mathbf{a}^{\mathrm{H}}\mathbf{h}, \end{aligned} \tag{5.19}$$

where the notations for frequency and window length have been dropped for convenience.

As previously stated, the Capon spectral estimation method can be derived through a constrained minimization problem. The function to be minimized is (5.17), which is subjected to the undistorted constraint on $H(\omega)$. This constraint is formally written as

$$\mathbf{a}^{\mathrm{H}}\mathbf{h} = 1. \tag{5.20}$$

The solution to this complex constrained minimization problem requires the use of complex Lagrangian multipliers. First let (5.20) be rewritten as

$$\left(\mathbf{a}_R^{\mathrm{T}} - j\mathbf{a}_I^{\mathrm{T}}\right)\left(\mathbf{h}_R + j\mathbf{h}_I\right) = 1, \tag{5.21}$$

or equivalently

$$\begin{aligned} \mathbf{a}_R^{\mathrm{T}}\mathbf{h}_R + \mathbf{a}_I^{\mathrm{T}}\mathbf{h}_I &= 1 \\ \mathbf{a}_R^{\mathrm{T}}\mathbf{h}_I - \mathbf{a}_I^{\mathrm{T}}\mathbf{h}_R &= 0. \end{aligned}$$

Since two sets of constraints exist now, the Lagrangian becomes

$$\begin{aligned} J(\mathbf{h}) &= \mathbf{h}^{\mathrm{H}}\mathbf{R}\mathbf{h} + \lambda_R\left(\mathbf{a}_R^{\mathrm{T}}\mathbf{h}_R + \mathbf{a}_I^{\mathrm{T}}\mathbf{h}_I - 1\right) + \lambda_I\left(\mathbf{a}_R^{\mathrm{T}}\mathbf{h}_I - \mathbf{a}_I^{\mathrm{T}}\mathbf{h}_R\right) \\ &= \mathbf{h}^{\mathrm{H}}\mathbf{R}\mathbf{h} + \lambda_R\mathrm{Re}\Big\{\mathbf{a}^{\mathrm{H}}\mathbf{h} - 1\Big\} + \lambda_I\mathrm{Im}\Big\{\mathbf{a}^{\mathrm{H}}\mathbf{h} - 1\Big\}, \end{aligned} \tag{5.22}$$

where λ_R and λ_I are real Lagrangian multipliers. However, letting $\lambda = \lambda_R + j\lambda_I$ represent a complex Lagrangian multiplier, then (5.22) simplifies

to

$$\begin{aligned} J(\mathbf{h}) &= \mathbf{h}^{\mathrm{H}}\mathbf{R}\mathbf{h} + \mathrm{Re}\Big\{ \big(\lambda_R + j\lambda_I\big)^* \big(\mathbf{a}^{\mathrm{H}}\mathbf{h} - 1\big) \Big\} \\ &= \mathbf{h}^{\mathrm{H}}\mathbf{R}\mathbf{h} + \mathrm{Re}\Big\{ \lambda^* \big(\mathbf{a}^{\mathrm{H}}\mathbf{h} - 1\big) \Big\} \\ &= \mathbf{h}^{\mathrm{H}}\mathbf{R}\mathbf{h} + \frac{1}{2}\lambda^* \big(\mathbf{a}^{\mathrm{H}}\mathbf{h} - 1\big) + \frac{1}{2}\lambda \big(\mathbf{a}^{\mathrm{T}}\mathbf{h}^* - 1\big) \\ &= \mathbf{h}^{\mathrm{H}}\mathbf{R}\mathbf{h} + \frac{1}{2}\lambda^* \big(\mathbf{a}^{\mathrm{H}}\mathbf{h} - 1\big) + \frac{1}{2}\lambda \big(\mathbf{h}^{\mathrm{H}}\mathbf{a} - 1\big). \end{aligned} \tag{5.23}$$

Since (5.23) is quadratic in $\mathbf{h}$, the minimum can be found by setting the derivative with respect to $\mathbf{h}$ equal to zero. As before, the Wirtinger derivative is employed to take the complex derivative of the real function, J, with respect to the complex filter. Furthermore, with (5.23) being quadratic in $\mathbf{h}$, the $\partial/\partial\mathbf{h}^{\mathrm{H}}$ operator is again preferable [90] and derivative becomes

$$\frac{\partial J(\mathbf{h})}{\partial \mathbf{h}^{\mathrm{H}}} = \mathbf{R}\mathbf{h} + \frac{1}{2}\lambda\mathbf{a}. \tag{5.24}$$

Setting (5.24) equal to zero and solving for $\mathbf{h}$ leads to an expression for the optimal filter, $\mathbf{h}_{opt}$, where

$$\mathbf{h}_{opt} = -\frac{\lambda}{2}\mathbf{R}^{-1}\mathbf{a}. \tag{5.25}$$

Substituting the optimal filter into (5.20) yields

$$\begin{aligned} \mathbf{a}^{\mathrm{H}}\mathbf{h}_{opt} &= 1 \\ -\frac{\lambda}{2}\mathbf{a}^{\mathrm{H}}\mathbf{R}^{-1}\mathbf{a} &= 1 \\ \frac{\lambda}{2} &= \frac{-1}{\mathbf{a}^{\mathrm{H}}\mathbf{R}^{-1}\mathbf{a}}. \end{aligned} \tag{5.26}$$

Finally substituting (5.26) for $\lambda/2$ in (5.25) produces the final expression for $\mathbf{h}_{opt}$ as

$$\mathbf{h}_{opt} = \frac{\mathbf{R}^{-1}\mathbf{a}}{\mathbf{a}^{\mathrm{H}}\mathbf{R}^{-1}\mathbf{a}}. \tag{5.27}$$

When $\mathbf{h}_{opt}$ is inserted into the filtered output power expression, (5.17), then the power spectral density (PSD) of the data, $S(\omega)$, is obtained as [79], [93], [94]

$$\begin{aligned} S(\omega) &= \mathbf{h}_{opt}^{\mathrm{H}}\mathbf{R}\mathbf{h}_{opt} \\ &= \frac{\mathbf{a}^{\mathrm{H}}\mathbf{R}^{-1}\mathbf{R}\mathbf{R}^{-1}\mathbf{a}}{\mathbf{a}^{\mathrm{H}}\mathbf{R}^{-1}\mathbf{a}\mathbf{a}^{\mathrm{H}}\mathbf{R}^{-1}\mathbf{a}} \\ &= \frac{\mathbf{a}^{\mathrm{H}}\mathbf{R}^{-1}\mathbf{a}}{\left(\mathbf{a}^{\mathrm{H}}\mathbf{R}^{-1}\mathbf{a}\right)\left(\mathbf{a}^{\mathrm{H}}\mathbf{R}^{-1}\mathbf{a}\right)} \\ &= \frac{1}{\mathbf{a}^{\mathrm{H}}\mathbf{R}^{-1}\mathbf{a}}. \end{aligned} \tag{5.28}$$

Since $\mathbf{R}$ is unknown in practice, it is estimated as

$$\begin{aligned}\hat{\mathbf{R}} &= \frac{1}{K}\sum_{k=0}^{K-1}\mathbf{y}_k\mathbf{y}_k^{\mathrm{H}} \\ &= \frac{1}{K}\mathbf{Y}\mathbf{Y}^{\mathrm{H}},\end{aligned} \tag{5.29}$$

where $\mathbf{Y}$ is expressed in (5.4). Then, the final Capon PSD estimate using all previous notations becomes

$$\hat{S}(\omega)_{CM} = \frac{1}{\mathbf{a}_L^{\mathrm{H}}(\omega)\hat{\mathbf{R}}^{-1}\mathbf{a}_L(\omega)}. \tag{5.30}$$

As an example, an LCD's location in angle can be estimated by letting the generic frequency ω be represented as spatial frequency ϑ. The ϑ that maximizes (5.30) corresponds to the relative angle between the ULA and LCD and can be formally written as

$$\hat{\vartheta}_{LCD} = \underset{\vartheta}{\operatorname{argmax}}\,\frac{1}{\mathbf{a}_L^{\mathrm{H}}(\vartheta)\hat{\mathbf{R}}^{-1}\mathbf{a}_L(\vartheta)}, \tag{5.31}$$

where $\hat{\vartheta}_{LCD}$ is the spatial frequency estimate of the LCD.

5.3.3 Capon Amplitude Estimation

Recalling the WLS solution from (5.11), the Capon method for estimating complex amplitude is defined when the weighting matrix, $\mathbf{\Phi}$, equals the in-

verse of the covariance matrix defined by (5.18) and estimated with (5.29). Thus, the Capon method produces a frequency dependent complex amplitude estimate equal to

$$\hat{\alpha}(\omega)_{CM} = \frac{\mathbf{a}_L^{\mathrm{H}}(\omega)\hat{\mathbf{R}}^{-1}\mathbf{g}(\omega)}{\mathbf{a}_L^{\mathrm{H}}(\omega)\hat{\mathbf{R}}^{-1}\mathbf{a}_L(\omega)}. \tag{5.32}$$

5.3.4 APES Amplitude Estimation

Again using the WLS solution from (5.11), the APES method estimates the complex amplitude by setting $\mathbf{\Phi} = \mathbf{Q}^{-1}(\omega)$, where $\mathbf{Q}(\omega)$ is defined as [81]

$$\mathbf{Q}(\omega) \stackrel{\text{def}}{=} \mathbf{R} - \mathbf{g}(\omega)\mathbf{g}^{\mathrm{H}}(\omega). \tag{5.33}$$

Substituting the estimated covariance matrix from (5.29) into (5.33) yields $\hat{\mathbf{Q}}(\omega)$ and causes the APES estimated complex amplitude to be

$$\hat{\alpha}(\omega)_{APES} = \frac{\mathbf{a}_L^{\mathrm{H}}(\omega)\hat{\mathbf{Q}}^{-1}(\omega)\mathbf{g}(\omega)}{\mathbf{a}_L^{\mathrm{H}}(\omega)\hat{\mathbf{Q}}^{-1}(\omega)\mathbf{a}_L(\omega)}. \tag{5.34}$$

The APES technique attempts to estimate the covariance matrix of the noise and interference by removing the data dependent contributions at ω. In turn, the APES method can be more computationally intense because a matrix inversion is required for each frequency ω. Therefore the matrix

inversion lemma is often employed for APES and expressed as [77]

$$\begin{aligned}\hat{\mathbf{Q}}^{-1}(\omega) &= \left[\hat{\mathbf{R}} - \mathbf{g}(\omega)\mathbf{g}^{\mathrm{H}}(\omega)\right]^{-1} \\ &= \hat{\mathbf{R}}^{-1} + \frac{\hat{\mathbf{R}}^{-1}\mathbf{g}(\omega)\mathbf{g}^{\mathrm{H}}(\omega)\hat{\mathbf{R}}^{-1}}{1 - \mathbf{g}^{\mathrm{H}}(\omega)\hat{\mathbf{R}}^{-1}\mathbf{g}(\omega)}. \end{aligned} \tag{5.35}$$

Substituting (5.35) into (5.34) yields the following simplified expression [77]

$$\hat{\alpha}(\omega)_{APES} = \frac{\mathbf{a}_L^{\mathrm{H}}(\omega)\hat{\mathbf{R}}^{-1}\mathbf{g}(\omega)}{\left[1 - \mathbf{g}^{\mathrm{H}}(\omega)\hat{\mathbf{R}}^{-1}\mathbf{g}(\omega)\right]\mathbf{a}_L^{\mathrm{H}}(\omega)\hat{\mathbf{R}}^{-1}\mathbf{a}_L(\omega) + \left|\mathbf{a}_L^{\mathrm{H}}(\omega)\hat{\mathbf{R}}^{-1}\mathbf{g}(\omega)\right|^2} \tag{5.36}$$

5.3.5 Two-Dimensional Extension

Next, let us define a two-dimensional space-time series as $x[n, m]$. At spatial and Doppler frequencies of ϑ and $\bar{f}$, $x[n, m]$ is expressed as

$$x[n, m] = \alpha(\vartheta, \bar{f})e^{j(\vartheta n + \bar{f}m)} + w_{\vartheta,\bar{f}}[n, m]. \tag{5.37}$$

In addition, assume the M pulses and N channels are linearly incremented in time and space. The subsequences are defined as [82]

$$\mathbf{y}_{k_N,k_M} \stackrel{\text{def}}{=} \mathrm{vec}\left(\begin{bmatrix} x[k_N, k_M] & \cdots & x[k_N, k_M + L_M - 1] \\ \vdots & \ddots & \vdots \\ x[k_N + L_N - 1, k_M] & \cdots & x[k_N + L_N - 1, k_M + L_M - 1] \end{bmatrix}\right), \tag{5.38}$$

where L_N and L_M are the respective lengths of the subsets of the space and time samples taken from $x[n,m]$. Furthermore, K_N and K_M are the number of unique windows in space and time, respectively, given as

$$K_N = N - L_N + 1 \tag{5.39}$$

$$K_M = M - L_M + 1. \tag{5.40}$$

Let $\mathbf{a}_{P_N,P_M}(\vartheta,\bar{f})$ be the space-time steering vector described by arbitrary lengths of P_N and P_M such that

$$\mathbf{a}_{P_N,P_M}(\vartheta,\bar{f}) = \begin{bmatrix} 1 & e^{j\bar{f}} & \dots & e^{j\bar{f}(P_M-1)} \end{bmatrix}^{\mathrm{T}} \otimes \begin{bmatrix} 1 & e^{j\vartheta} & \dots & e^{j\vartheta(P_N-1)} \end{bmatrix}^{\mathrm{T}}, \tag{5.41}$$

where $\otimes$ represents a Kronecker product. Next, define $\mathbf{Y}$ as the collection of snapshots (subsequences) that are arranged as

$$\mathbf{Y} = \begin{bmatrix} \mathbf{y}_{0,0} & \mathbf{y}_{1,0} & \cdots & \mathbf{y}_{K_N-1,0} & \mathbf{y}_{0,1} & \mathbf{y}_{1,1} & \cdots & \mathbf{y}_{K_N-1,K_M-1} \end{bmatrix}, \tag{5.42}$$

and let

$$\mathbf{A}(\vartheta,\bar{f}) = \mathbf{a}_{L_N,L_M}(\vartheta,\bar{f})\mathbf{a}^{\mathrm{T}}_{K_N,K_M}(\vartheta,\bar{f}). \tag{5.43}$$

An expression similar to (5.8) can then be given for the two-dimensional case as

$$\mathbf{Y} = \alpha(\vartheta,\bar{f})\mathbf{A}(\vartheta,\bar{f}) + \mathbf{W}(\vartheta,\bar{f}). \tag{5.44}$$

Going through similar derivations as before will lead to a WLS complex amplitude estimate for the two-dimensional case that is given as

$$\hat{\alpha}(\vartheta,\bar{f}) = \frac{\mathbf{a}^{\mathrm{H}}_{L_N,L_M}(\vartheta,\bar{f})\mathbf{\Phi}\mathbf{g}(\vartheta,\bar{f})}{\mathbf{a}^{\mathrm{H}}_{L_N,L_M}(\vartheta,\bar{f})\mathbf{\Phi}\mathbf{a}_{L_N,L_M}(\vartheta,\bar{f})}, \tag{5.45}$$

where $\mathbf{g}(\vartheta,\bar{f})$ is now defined as

$$\begin{aligned}\mathbf{g}(\vartheta,\bar{f}) &\stackrel{\text{def}}{=} \frac{1}{K_N K_M}\sum_{k_n=0}^{K_N-1}\sum_{k_m=0}^{K_M-1}\mathbf{y}_{k_n,k_m}e^{j(\vartheta k_n+\bar{f}k_m)} \\ &= \frac{1}{K_N K_M}\mathbf{Y}\mathbf{a}^{*}_{K_N,K_M}(\vartheta,\bar{f}).\end{aligned} \tag{5.46}$$

Finally, the estimations of the complex amplitude using the two dimensional dataset for the Capon and APES methods are

$$\hat{\alpha}(\vartheta,\bar{f})_{CM} = \frac{\mathbf{a}^{\mathrm{H}}_{L_N,L_M}(\vartheta,\bar{f})\hat{\mathbf{R}}^{-1}\mathbf{g}(\vartheta,\bar{f})}{\mathbf{a}^{\mathrm{H}}_{L_N,L_M}(\vartheta,\bar{f})\hat{\mathbf{R}}^{-1}\mathbf{a}_{L_N,L_M}(\vartheta,\bar{f})} \tag{5.47}$$

$$\hat{\alpha}(\vartheta,\bar{f})_{APES} = \frac{\mathbf{a}^{\mathrm{H}}_{L_N,L_M}(\vartheta,\bar{f})\hat{\mathbf{Q}}^{-1}(\vartheta,\bar{f})\mathbf{g}(\vartheta,\bar{f})}{\mathbf{a}^{\mathrm{H}}_{L_N,L_M}(\vartheta,\bar{f})\hat{\mathbf{Q}}^{-1}(\vartheta,\bar{f})\mathbf{a}_{L_N,L_M}(\vartheta,\bar{f})}, \tag{5.48}$$

where $\hat{\mathbf{R}}$ and $\hat{\mathbf{Q}}$ are

$$\hat{\mathbf{R}} = \frac{1}{K_N K_M}\mathbf{Y}\mathbf{Y}^{\mathrm{H}} \tag{5.49}$$

$$\hat{\mathbf{Q}}(\vartheta,\bar{f}) = \hat{\mathbf{R}} - \mathbf{g}(\vartheta,\bar{f})\mathbf{g}^{\mathrm{H}}(\vartheta,\bar{f}). \tag{5.50}$$

For completeness, the APES complex amplitude estimation can be more efficiently computed through the matrix inversion lemma and is given as

$$\hat{\alpha}(\vartheta,\bar{f})_{APES} = \frac{\mathbf{a}^{\mathrm{H}}_{L_N,L_M}(\vartheta,\bar{f})\hat{\mathbf{R}}^{-1}\mathbf{g}(\vartheta,\bar{f})}{\left[1-\mathbf{g}^{\mathrm{H}}(\vartheta,\bar{f})\hat{\mathbf{R}}^{-1}\mathbf{g}(\vartheta,\bar{f})\right]\mathbf{a}^{\mathrm{H}}_{L_N,L_M}(\vartheta,\bar{f})\hat{\mathbf{R}}^{-1}\mathbf{a}_{L_N,L_M}(\vartheta,\bar{f}) + \left|\mathbf{a}^{\mathrm{H}}_{L_N,L_M}(\vartheta,\bar{f})\hat{\mathbf{R}}^{-1}\mathbf{g}(\vartheta,\bar{f})\right|^2}. \tag{5.51}$$

Last, the Capon PSD estimate, $\hat{S}(\vartheta,\bar{f})_{CM}$, can be derived similarly as in Section 5.3.2 for the two-dimensional dataset. After solving for the constrained optimization problem by means of Lagrangian multipliers, the Capon PSD estimate becomes

$$\hat{S}(\vartheta,\bar{f})_{CM} = \frac{1}{\mathbf{a}^{\mathrm{H}}_{L_N,L_M}(\vartheta,\bar{f})\hat{\mathbf{R}}^{-1}\mathbf{a}_{L_N,L_M}(\vartheta,\bar{f})}. \tag{5.52}$$

The Capon spectrum is now two-dimensional. Therefore, searching for an LCD's location requires, in theory, a two-dimensional search across spatial and Doppler frequencies. However, with an assumption that the LCD is stationary (zero Doppler) and knowing that the clutter ridge for PBR is linear over spatial and Doppler frequencies, the two-dimensional search grid can be limited to a one-dimensional search through the use of the clutter ridge equation, (3.12).

5.4 LCD Removal Algorithm and Analysis

Overall, the LCD removal (LCDR) algorithm can be outlined in the following steps:

1. Determine range bin location of LCD using CFAR detector
2. Estimate LCD location in angle-Doppler by Capon power estimation, (5.52)
3. Estimate complex amplitude of LCD

   Use APES amplitude estimation, (5.48), at specific space-time location to attain initial guess

   Finalize complex amplitude estimate through iterative process that minimizes output power at specific space-time location
4. Subtract LCD from datacube by using the estimates from 2 and 3

Figure 5.1 illustrates the steps with a flowchart. The next sections will analyze each algorithm step and provide incremental results.

5.4.1 Step 1: LCD Detection

As in Chapter 4, the choice of an emitter impacts the performance, or in this case, the ability of detecting LCDs. To illustrate the impact of emitter se-

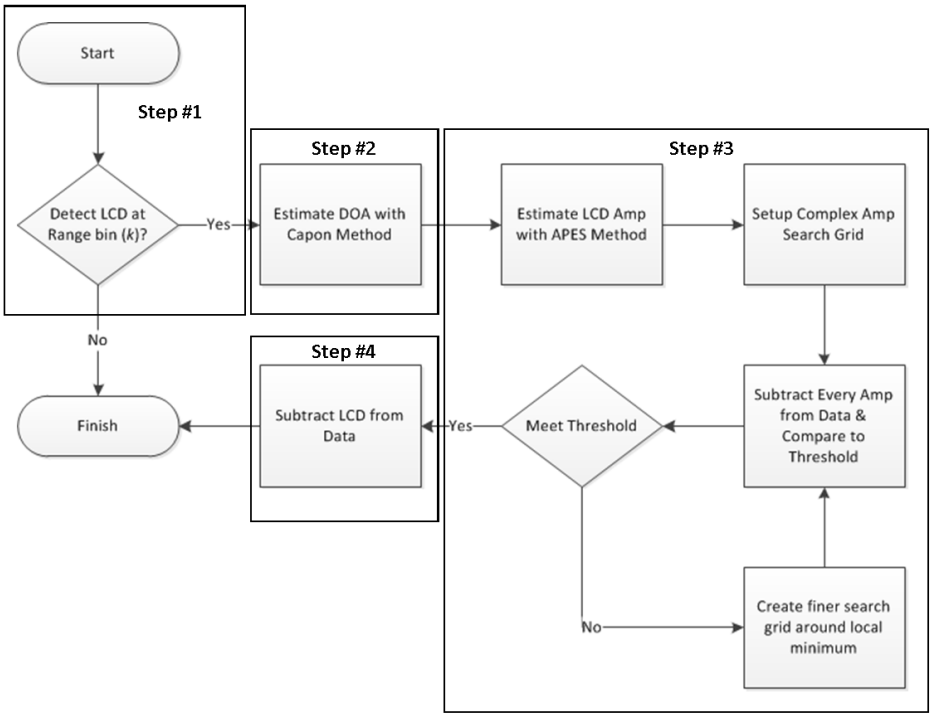

Figure 5.1: Flowchart of the LCD Removal (LCDR) algorithm.

lection, two examples will be provided. The only difference between these examples is the location of the emitter.

Unsuccessful LCD Detection

Consider the scenario illustrated in Figure 5.2 where a receiver is at $(0, 0,$ 1000 m$)$, a transmitter is at $(1573$ m, 421 m, 60 m$)$, and an LCD resides at $(3315$ m, 657 m, $0)$. This geometry creates clutter coordinates of $(\theta_I,\ \theta_S,$ $\phi_{OP}) = (1.95^\circ, 16.48^\circ, 3.52^\circ)$. These coordinates, in turn, cause the LCD to reside in an area with high clutter energy due to in-plane scattering effects.

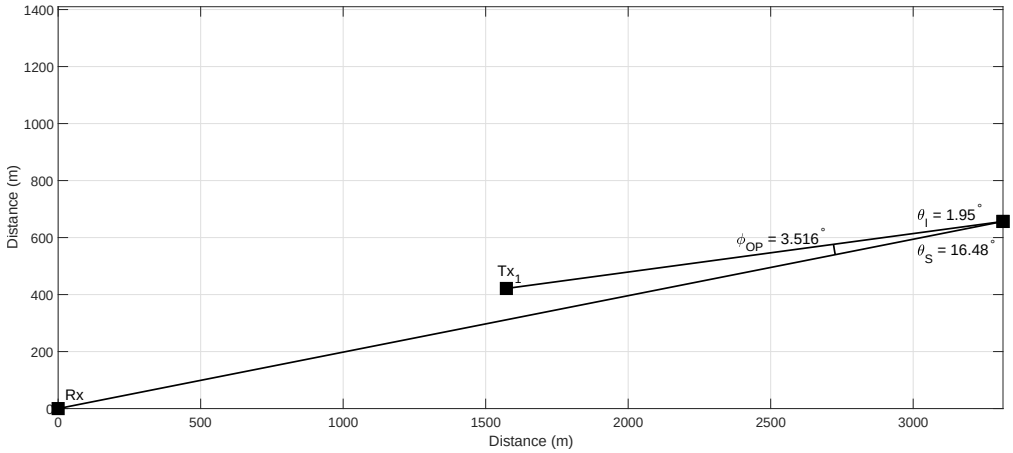

Figure 5.2: Orientation of receiver, transmitter, and target. The LCD is in the vicinity of the target in this in-plane setup.

Figure 5.3 depicts two clutter-energy-versus-range images where one is for the clairvoyant case when the clutter covariance matrix (CCM) is known while the other is when the CCM is estimated. It is easy to locate the LCD for the clairvoyant case, but the CFAR detector fails to detect the presence of

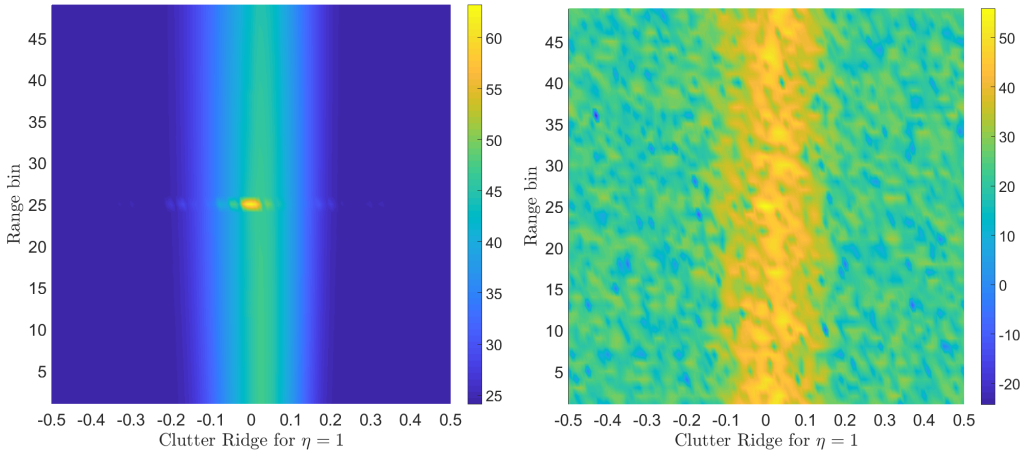

(a) Clairvoyant (b) Estimated

Figure 5.3: Clutter ridge versus range bin when using two different covariance matrices for the Figure 5.2 scenario.

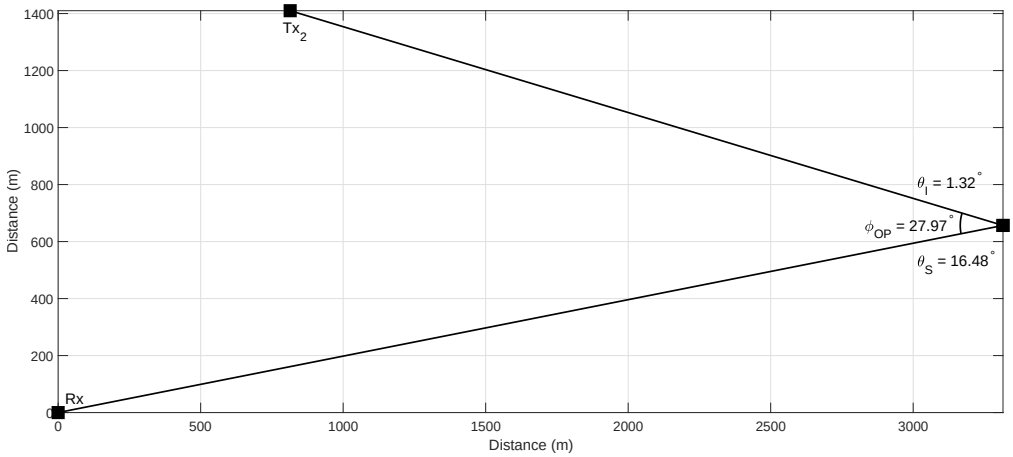

Figure 5.4: Orientation of receiver, transmitter, and target. The LCD is in the vicinity of the target in this out-of-plane setup.

the LCD with the estimated CCM. Therefore, the LCD cannot be removed due to the relative geometry of the receiver, transmitter and LCD.

Successful LCD Detection

The next example, depicted in Figure 5.4, repositions the transmitter to $(814\text{m}, 1410\text{m}, 60\text{m})$. This equates to a relative geometry where the out-of-plane angle, ϕ_{OP}, is greater than before. This greater angle causes the majority of the clutter energy to reside at higher spatial/Doppler frequencies. Therefore the LCD becomes located in a noise limited region on the clutter ridge.

Figure 5.5 shows the clairvoyant and estimated clutter energy spectra. With the LCD more isolated from strong clutter, the CA-CFAR detector accurately locates the range bin of the LCD. If multiple stationary emitters are in an area of an LCD, then selecting the emitter that does not lie in-plane

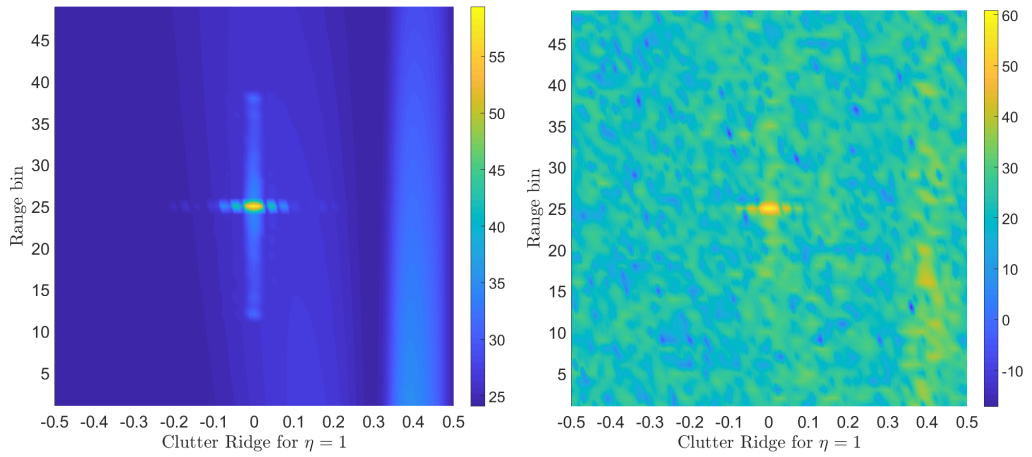

(a) Clairvoyant (b) Estimated

Figure 5.5: Clutter ridge versus range bin when using two different covariance matrices for the Figure 5.4 scenario.

with the receiver and LCD (e.g. $\phi_{OP} \neq 0°$ or $\phi_{OP} \neq 180°$) creates a more favorable detection problem.

Figure 5.6 further illustrates this concept. The LCD is difficult to detect within the received data from Tx_1 because it lies in a high-clutter region around zero spatial frequency (as seen in Figure 5.3b). However, the high clutter region from Tx_2 is located at higher spatial/Doppler frequencies away from zero. With the clutter energy shifting in frequencies, the LCD becomes much more isolated (as seen in Figure 5.5b) and easier to detect.

It is also important to highlight the impact of an LCD for the two scenarios. By comparing Figures 5.3b and 5.5b, it can be seen that the LCD is relatively stronger around its local region in the out-of-plane scenario for Tx_2. When the LCD resides within a high clutter region, then the LCD is

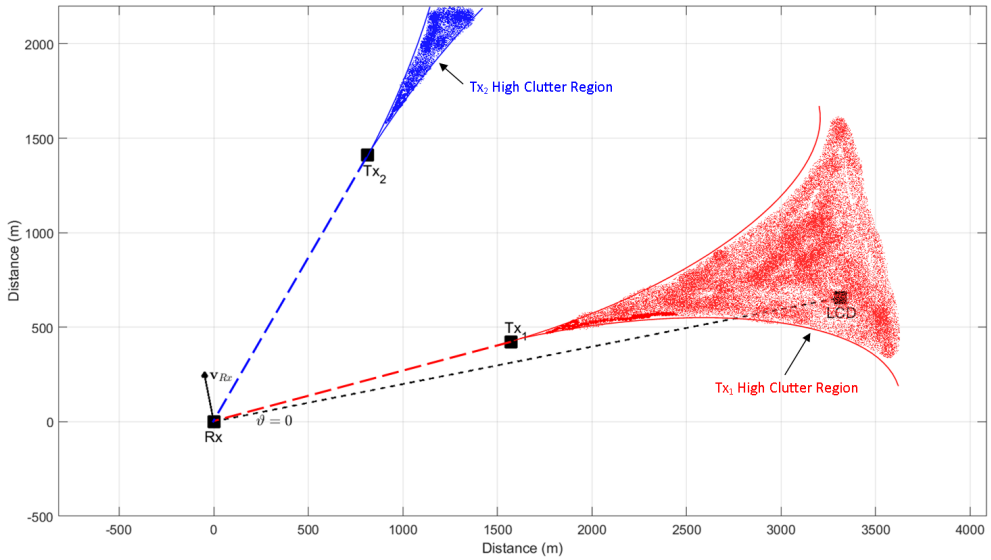

Figure 5.6: Conceptual view of where high clutter regions reside for different transmitters.

less impactful on performance and harder to detect. Therefore, if an emitter that is in-plane with an LCD is chosen as optimal, then removing an LCD may be unnecessary. However, if the chosen emitter exhibits an out-of-plane geometry with the LCD, then the LCD needs to be detected and removed.

For the remainder of Section 5.4, only the scenario with Tx_2 as described in Figures 5.4 and 5.6 will be discussed. The remaining incremental results were created off the Tx_2 simulated data.

5.4.2 Step 2: LCD Spectral Estimation

After the detection of an LCD occurs, then the spatial and Doppler frequencies are estimated using (5.52). However, the window lengths for the chan-

nel and time samples, L_N and L_M, must be chosen. Ultimately, there are MN different choices for calculating the Capon spectrum. Figure 5.7 depicts all MN Capon spectrum estimates for $M = 32$ pulses, $N = 8$ channels. The spectra are populated with approximately $5,000$ spatial and Doppler frequency pairs from the clutter ridge at the range bin of the detected LCD. The sharp peak in each sub-figure highlights the LCD's spatial and Doppler frequencies.

Previous literature states the appropriate choices for L_N and L_M should be limited by $L_N \leq N/2$ and $L_M \leq M/2$ [77], [78], [81], [86]. The reason for this limitation comes from (5.49). Whenever the limits are passed, then the estimated covariance matrix is no longer full rank. Therefore, $\hat{\mathbf{R}}$ must be diagonally loaded before calculating the Capon spectrum. Figure 5.7 suggests the limit can be violated for at least this estimation problem. The reasoning behind this observation is due to the fact that an LCD is well approximated with a rank 1 matrix. Furthermore, an LCD corresponds to the largest and most influential eigenvalue in the CCM. So even in the extreme case of $L_N = N$ and $L_M = M$, the calculated Capon spectrum produces a peak (albeit weak) at the LCD location (see Figure 5.7h). The lengths that actually produce the worst Capon spectrum are when $L_N = L_M = 1$ (see 5.7a). The poor performance occurs because no resolution can be attained

when $\hat{\mathbf{R}}$ is a scalar. So with increasing lengths, the resolution increases at the expense of $\hat{\mathbf{R}}$ becoming singular.

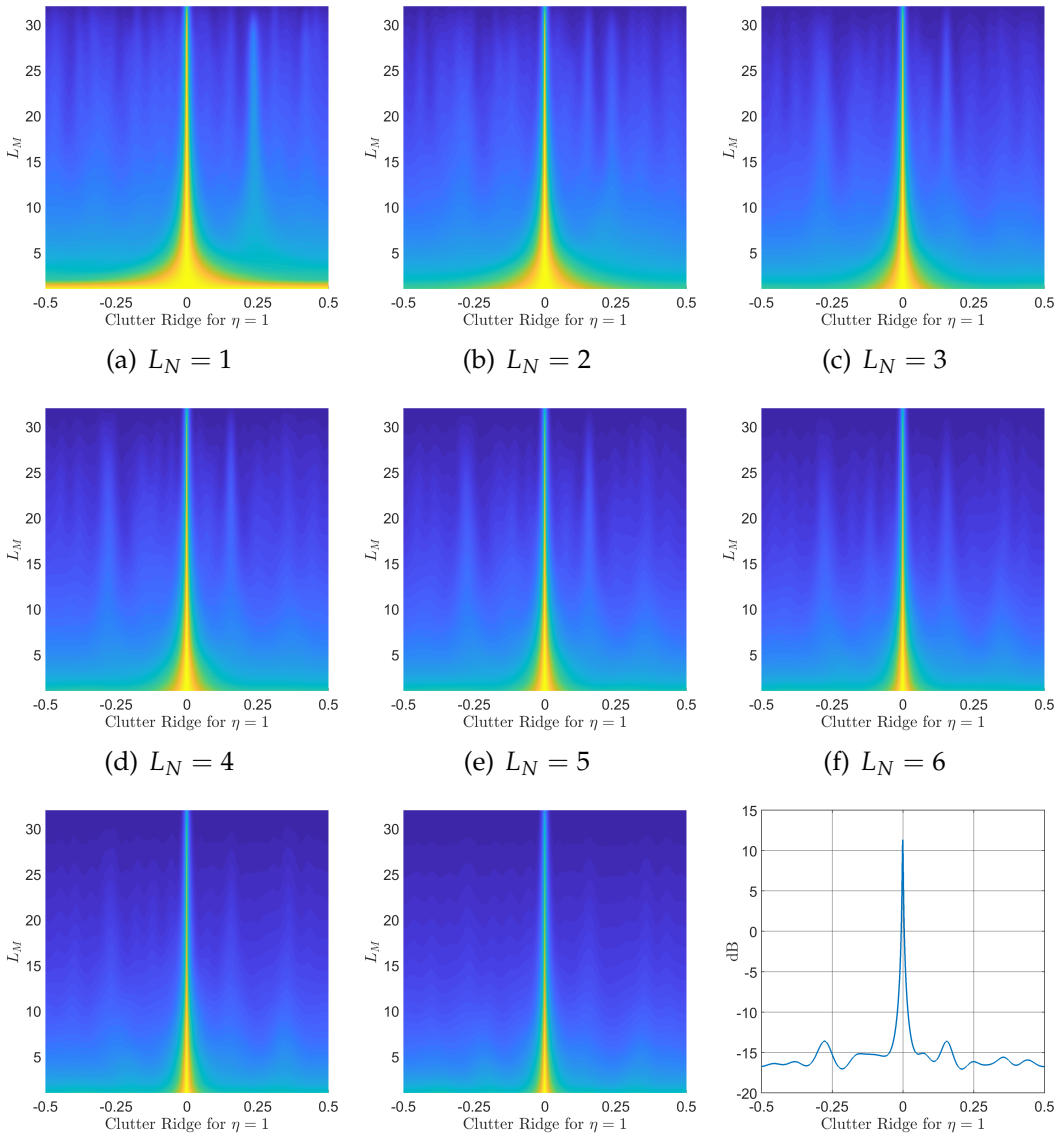

(a) $L_N = 1$ (b) $L_N = 2$ (c) $L_N = 3$

(d) $L_N = 4$ (e) $L_N = 5$ (f) $L_N = 6$

(g) $L_N = 7$ (h) $L_N = 8$ (i) $L_N = 4$ and $L_M = 16$

Figure 5.7: Capon spectrums for all combinations of L_N and L_M window lengths.

5.4.3 Step 3: LCD Amplitude Estimation

After estimating the spatial and Doppler frequencies of the LCD, the APES method from (5.48) is used to estimate the LCD's complex amplitude. Even though previous literature states the APES method is superior to the Capon technique for estimating amplitude, it was seen that the accuracy failed to achieve any substantial removal of an LCD. Therefore, the APES estimator was used for a variety of L_N and L_M to create multiple estimates. Then the statistical outliers were removed to reduce the search area as represented in Figure 5.8. With the real and imaginary amplitude limits defined, a linearly spaced search grid of size 25 by 25 is used to find the local minimum for

$$S = \mathbf{s}_{s-t}^{\mathrm{H}} \mathrm{vec}\left\{\mathbf{x}_k - \hat{\alpha}\mathbf{s}_s\mathbf{s}_t^{\mathrm{T}}\right\} \mathrm{vec}\left\{\mathbf{x}_k - \hat{\alpha}\mathbf{s}_s\mathbf{s}_t^{\mathrm{T}}\right\}^{\mathrm{H}} \mathbf{s}_{s-t}. \tag{5.53}$$

This equation is first subtracting the hypothesized complex amplitudes in the search grid from the data at the range bin of the LCD, and then calculating the expected output power at the spatial and Doppler frequencies from step #2. Then a new and more localized search grid is created, and the process is reimplemented with (5.53). This iterative approach is used until a user defined threshold is attained as depicted in the flowchart in Figure 5.1. Figure 5.8 illustrates the first and last iteration of this approach. The goal here was not to optimize the iterative method's rate of convergence, but to

verify that the LCD amplitude estimation step is effective for the ultimate removal of LCD.

5.4.4 Step 4: LCD Removal

Once the iterative process produces the final complex amplitude estimate, the LCD and its sidelobes are subtracted from the data cube. To subtract the sidelobes from the radar data cube, the full range profile that is pulse dependent must be used in the subtraction. The new data cube, $\mathbf{x}'_k$, is defined as

$$\mathbf{x}'_k = \mathbf{x}_k - \hat{\alpha}_{LCD,k_0}\Big(\mathbf{1}_{N\times 1}\cdot \mathbf{R}_{xx}[k_0-k]\Big)\odot\Big(\mathbf{s}_s\mathbf{s}_t^{\mathrm{T}}\Big), \tag{5.54}$$

where $\odot$ is the Hadamard or piece-wise product, k_0 is the range bin where the LCD is detected, and $\mathbf{R}_{xx}[k_0-k]$ is the normalized pulse-diverse autocorrelation function given as

$$\mathbf{R}_{xx}[k_0-k] = \begin{bmatrix} R^1_{xx}[k_0-k] & R^2_{xx}[k_0-k] & \dots & R^M_{xx}[k_0-k] \end{bmatrix}. \tag{5.55}$$

Figure 5.9 depicts the clutter energy spectrum for before and after LCDR. The color scales have been set to the dynamic range of the LCDR dataset. It can be seen by comparing the two subplots in the top row that the LCD was reduced by approximately 25 dB. The reduction of range sidelobes from the LCD can be seen when comparing the two graphs from the second row.

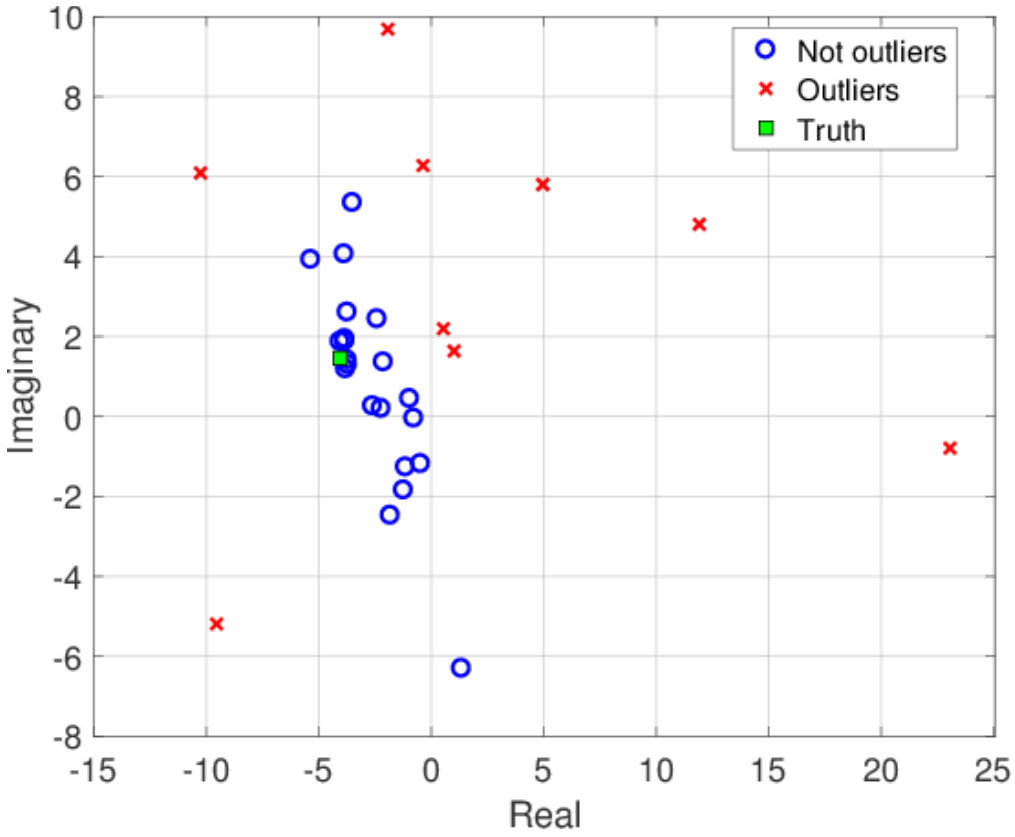

(a) Initial Estimates using APES

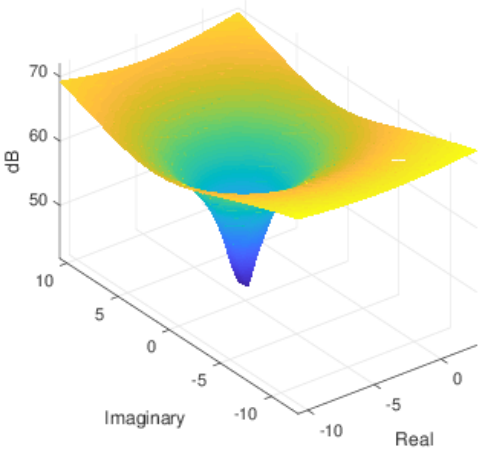

(b) First Search

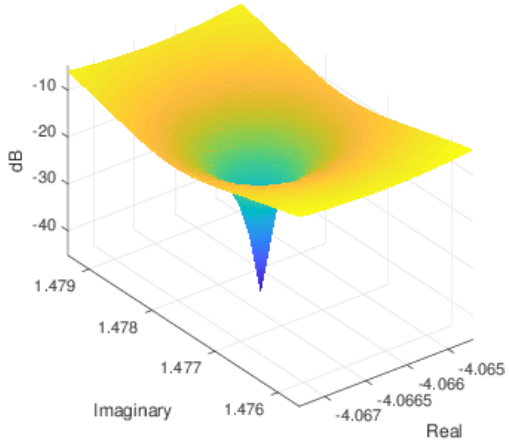

(c) Eleventh Search

Figure 5.8: Complex amplitude recursive estimation.

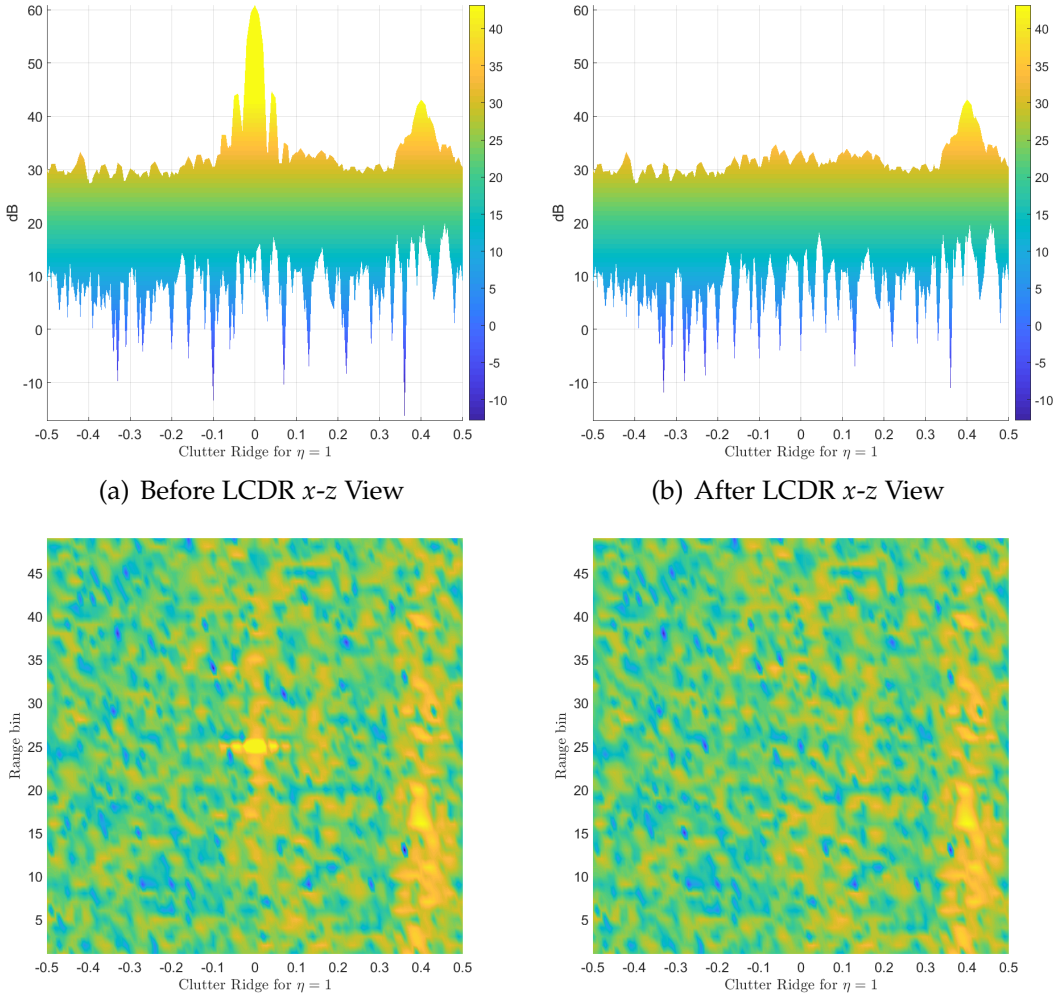

(a) Before LCDR x-z View

(b) After LCDR x-z View

(c) Before LCDR x-y View

(d) After LCDR x-y View

Figure 5.9: Clutter ridge versus range bin for before and after LCDR

These range sidelobes are easily visible in Figure 5.9c at the zero frequency cut, while they have been mitigated in Figure 5.9d at the same frequency cut.

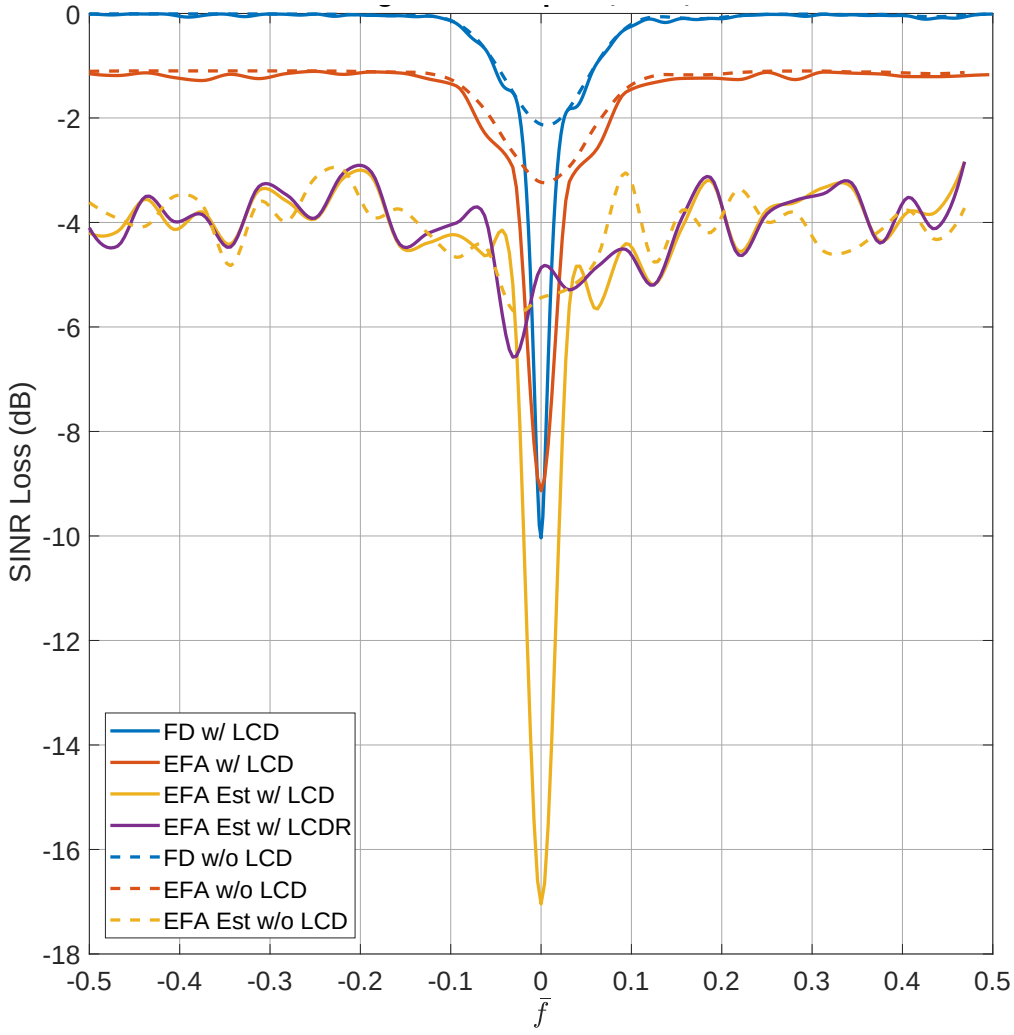

Figure 5.10: Comparison of SINR loss curves when LCD resides in the training data.

5.5 Results

For an LCD in the training data, the final results are given in Figure 5.10 where seven SINR loss curves are shown at a spatial cut of $\vartheta = 0$. The solid lines represent curves from a data set with an LCD while the dashed lines illustrate SINR loss from a different realization that does not contain an LCD

within the data set. Both data sets were generated using the scenario depicted in Figure 5.5. Additionally, the blue lines represent SINR loss from full dimension (FD) STAP using the ideal/clairvoyant CCM. The red lines are for extended factored algorithm (EFA) STAP when using the clairvoyant CCM. The gold lines depict EFA STAP performance when the CCM is estimated from the training data, or surrounding range bins. Finally, the purple line is the performance for EFA STAP with an estimated CCM after implementing the LCDR algorithm.

The first noticeable feature is the impact of the LCD. This can be seen when comparing like colored curves and seeing the sharp loss in SINR at the Doppler frequency of the LCD, $\bar{f} = 0$. Furthermore, the LCD impact in the clairvoyant algorithms is only due to the range sidelobes that come from the use of non-ideal pulse diverse waveforms. The LCD is actually not in the CUT, but rather in the training data. However, the range sidelobes from the LCD are in the CUT, which causes notches in performance even when using the clairvoyant CCM (solid blue and red lines). Therefore, when the CCM is estimated, as in the solid gold line, the adaptive filter over-estimates the LCD and experiences a much greater loss than necessary at $\bar{f} = 0$. This loss is about 7 dB less than optimal performance.

The performance increase from the LCDR algorithm can be measured at approximately 12 dB improvement at $\bar{f} = 0$. By successfully removing

the LCD from the dataset, the SINR loss for the estimated EFA algorithm is better performing than even the optimal FD STAP. The performance of the LCDR actually mimics the performance for the dataset where an LCD does not exist (dashed gold line).

Figure 5.11 shows the same SINR loss curves for the same geometry. However, now the LCD is in the CUT. This can be seen by comparing the notch of the gold solid line with the clairvoyant algorithms' notches. They have very similar depths because the training data is only corrupted by the range sidelobes of the LCD. Therefore, the estimated covariance matrix underestimates the LCD at the CUT and could likely lead to a false alarm.

As for the LCDR algorithm performance, it again drastically improves the SINR loss. In this setup, there is almost 25 dB of improved SINR at $\bar{f} = 0$ when comparing the before and after LCDR of the estimated EFA. Then, comparing the LCDR performance to that of the optimal FD, an increase of about 20 dB is seen.

Last, the performance difference from subtracting only the LCD peak versus the LCD peak and sidelobes should be considered. Figure 5.12 repeats the SINR loss curves from Figure 5.10 for the before and after LCDR cases when implementing the EFA and using an estimated covariance matrix. The new dashed curve illustrates the SINR loss when only the peak is subtracted from the data cube. While more loss appears at the Doppler

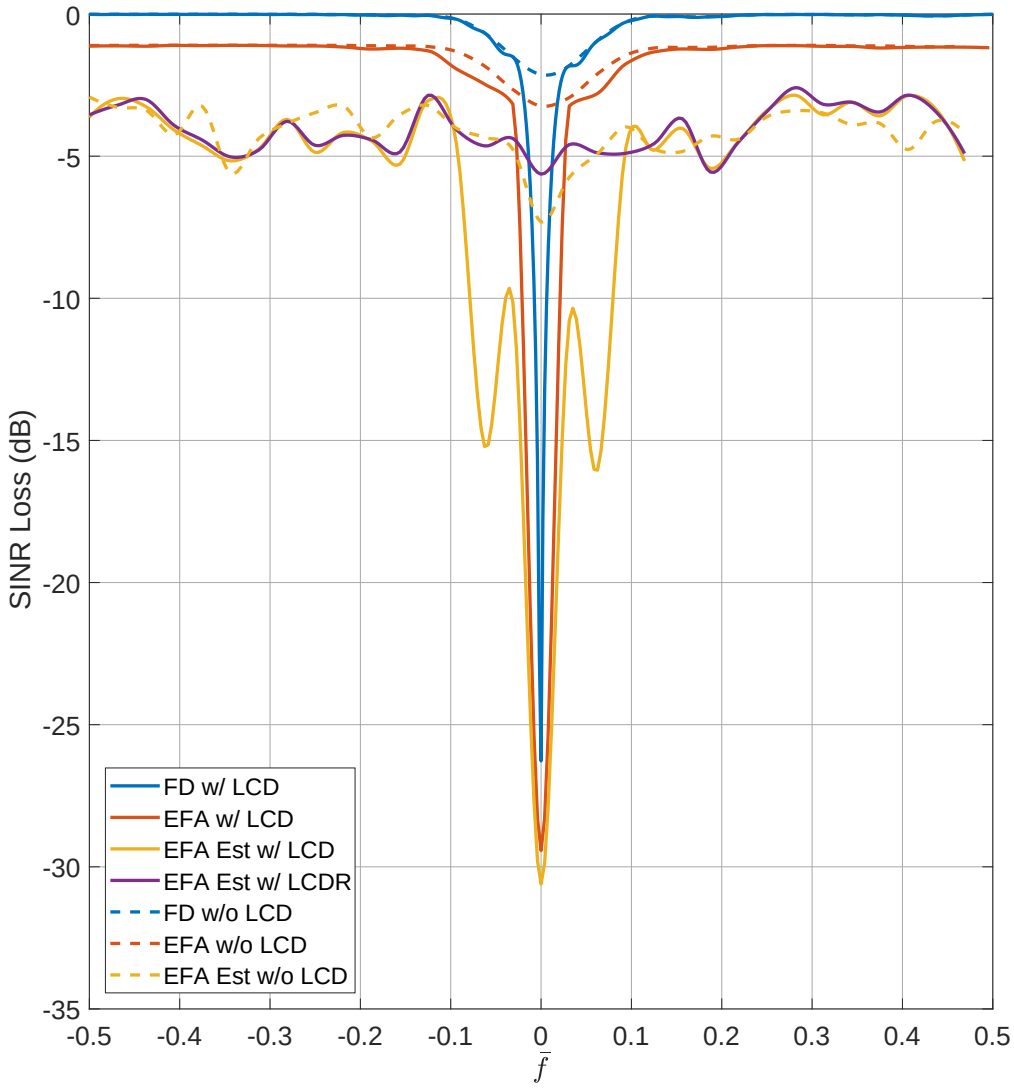

Figure 5.11: Comparison of SINR loss curves when LCD resides within the CUT.

frequency of the LCD when only subtracting the peak, it is less than 2 dB. Therefore, getting accurate estimates of the LCD is vastly more important than subtracting the LCD peak and range sidelobes.

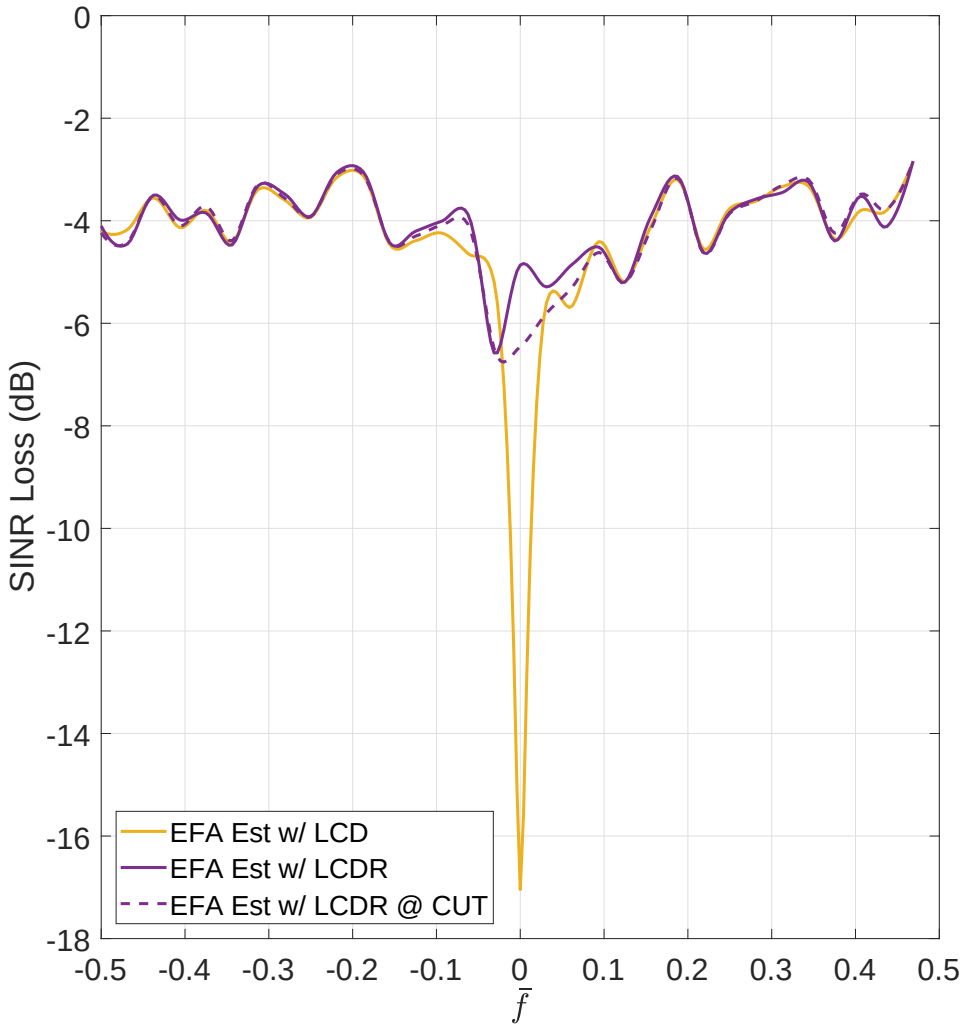

Figure 5.12: Comparison of SINR loss curves when LCD resides in the training data and not subtracting the LCD sidelobes.

Chapter 6

Conclusions

In conclusion, a heterogeneous clutter model was developed that mimics bistatic clutter measurements taken over various in-plane and out-of-plane angles. Furthermore, clutter Doppler spread was derived for the first time and then related to covariance matrix tapers (CMT) in order to apply the spreading. The clutter reflectivity modeling is applicable to any bistatic system while the CMTs can be applied to any pulse-diverse waveform simulation.

Down-selecting to an optimal emitter of opportunity was done through metrics studied in Chapter 4. It was seen that the best choice depends on the coupling of the relative geometry of the target, receiver, and transmitters with that of the target's RCS and two-dimensional velocity in relation to the receiver's velocity vector. The usable velocity space fraction (UVSF) was developed to reduce a four-dimensional problem down into one number. However, it was found that UVSF is only as good as the assumed target

RCS. Therefore, the best metric depends on the target detection scenario and whether any a priori knowledge exists. Overall, slower targets have a better chance of being detected when they lie outside of the plane that contains the transmitter and receiver. However, fast moving targets with small RCS have a better chance of detection for high-SNR Cassini ovals, which could be in the same plane as the transmitter and receiver.

Finally, a large clutter discrete (LCD) was successfully simulated, detected, estimated, and removed. The detection and estimation of the LCD from random data was assisted from the LCD being more isolated on the clutter ridge for out-of-plane geometries. The algorithm was unsuccessful when the LCD was present near the projected bistatic baseline. Successfully removing LCDs either improves target detections or reduces false alarms for GMTI.

6.1 Future Work

Only the 4G LTE waveform at bandwidth of approximately 20 MHz was considered due to the large amount of other variables. At this time, it is considered that the LTE waveform offers the best compromise between bandwidth and availability for a PBR system performing GMTI. However, the performance from other waveforms should be formally explored along with

future commercial waveforms such as 5G LTE. Since 5G LTE is a MIMO waveform, a feasibility study would need to be conducted.

The fidelity of the model could be improved by assuming a $4/3$ Earth model. This would greatly increase the complexity because analytical solutions to isorange rings would not exist. Instead a numerical solver would need to be utilized.

Probably more interesting would be to add to the model a feature that assesses the ability to capture a direct path signal. If a waveform cannot be captured with sufficient SNR, the integrity of the datacube is reduced. Then, target detection and/or LCD removal may fail. Furthermore, if different SNRs are modeled for different transmitters in a scene, then some transmitters could be eliminated before metrics are ever analyzed.

Another interesting topic would consider a real-world setup. This setup would include various emitter types and locations. With the addition of highways, moving target velocity vectors could be assumed along different locations on the highways. Then, an emitter selection experiment could be conducted using the metrics plus a priori knowledge.

References

[1] A. Leon-Garcia, *Probability, Statistics, and Random Processes for Electrical Engineering*. Pearson/Prentice Hall, 2008. [Online]. Available: https://books.google.com/books?id=GUJosCkbBywC.

[2] A. R. Domville, "The bistatic reflection from land and sea of x-band radio waves, part I", *GEC Electronics Ltd., Stanmore, England, Memo. SLM 1802*, 1967.

[3] ——, "The bistatic reflection from land and sea of x-band radio waves, part II", *GEC Electronics Ltd., Stanmore, England, SLM 2116*, 1968.

[4] B. L. Matkin, J. H. Mullins, T. J. Ferster, and P. J. Vanderford, "Bistatic reflectivity measurements at x, ku, ka and w-band frequencies", in *Proceedings of the 2001 IEEE Radar Conference*, 2001, pp. 404–409.

[5] ——, "Bistatic reflectivity measurements on various terrains at x, ku, ka and w-band frequencies", in *Proceedings of the 2002 IEEE Radar Conference*, 2002, pp. 266–271.

[6] D. Tan, M. Lesturgie, H. Sun, and Y. Lu, "Space-time interference analysis and suppression for airborne passive radar using transmissions of opportunity", *Radar, Sonar & Navigation, IET*, vol. 8, no. 2, pp. 142–152, 2014, ISSN: 1751-8784.

[7] S. Mudaliar, "Bistatic radar clutter simulations using scattering phenomenology", in *2006 IEEE Conference on Radar*, 2006, pp. 302–309.

[8] R. Duan, X. Wang, and Z. Chen, "Space-time clutter model for airborne bistatic radar with non-gaussian statistics", in *IEEE Radar Conference*, 2008, pp. 1–6.

[9] M. Pola and P. Bezousek, "Modeling of bistatic radar clutter", *Perners contacts. CZ*, vol. 7, no. 2, 2012.

[10] M. Pola, P. Bezousek, and J. Pidanic, "Model comparison of bistatic radar clutter", in *Microwave Techniques (COMITE), 2013l Conference on*, 2013, pp. 182–185.

[11] J. Johnson, C. Baker, G. Smith, K. Bell, and M. Rangaswamy, "The monostatic-bistatic equivalence theorem and bistatic radar clutter", in *European Radar Conference (EuRAD), 2014 11th*, 2014, pp. 105–108. DOI: 10.1109/EuRAD.2014.6991218.

[12] J. R. Lievsay and N. A. Goodman, "Multi-transmitter clutter modeling for passive stap", in *2016 IEEE Radar Conference (RadarConf)*, 2016, pp. 1–6. DOI: 10.1109/RADAR.2016.7485070.

[13] R. Klemm, "Comparison between monostatic and bistatic antenna configurations for stap", *IEEE Transactions on Aerospace and Electronic Systems*, vol. 36, no. 2, pp. 596–608, 2000, ISSN: 0018-9251.

[14] Y. Qu, G. Liao, S. Zhu, and X. Liu, "Analysis of range dependence of clutter spectrum in bistatic stap", *AEU-International Journal of Electronics and Communications*, vol. 64, no. 6, pp. 512–520, 2010.

[15] B. Himed, Y. Zhang, and A. Hajjari, "Stap with angle-doppler compensation for bistatic airborne radars", in *Proceedings of the IEEE Radar Conference*, 2002, pp. 311–317.

[16] W. L. Melvin, B. Himed, and M. E. Davis, "Doubly adaptive bistatic clutter filtering", in *Proceedings of the 2003 IEEE Radar Conference*, 2003, pp. 171–178.

[17] O. Kreyenkamp and R. Klemm, "Doppler compensation in forward-looking stap radar", *IEE Proceedings - Radar, Sonar and Navigation*, vol. 148, no. 5, pp. 253–258, 2001, ISSN: 1350-2395.

[18] S. M. Kogon and M. A. Zatman, "Bistatic stap for airborne radar systems", in *Proc. Adaptive Sensor Array Processing Workshop*, 2000, pp. 1–6.

[19] G. K. Borsari, "Mitigating effects on stap processing caused by an inclined array", in *Proceedings of the 1998 IEEE Radar Conference*, IEEE, 1998, pp. 135–140.

[20] F. Pearson and G. Borsari, "Simulation and analysis of adaptive interference suppression for bistatic surveillance radars", MIT Lincoln Laboratory, Tech. Rep., 2001.

[21] W. L. Melvin, M. J. Callahan, and M. C. Wicks, "Adaptive clutter cancellation in bistatic radar", in *Conference Record of the Thirty-Fourth Asilomar Conference on Signals, Systems and Computers*, vol. 2, 2000, 1125–1130 vol.2.

[22] B. Himed, J. H. Michels, and Y. Zhang, "Bistatic stap performance analysis in radar applications", in *Proceedings of the 2001 IEEE Radar Conference*, 2001, pp. 198–203.

[23] W. L. Melvin, M. J. Callahan, and M. C. Wicks, "Bistatic stap: Application to airborne radar", in *Proceedings of the IEEE Radar Conference*, 2002, pp. 1–7.

[24] F. D. Lapierre and J. G. Verly, "Registration-based range-dependence compensation for bistatic stap radars", *EURASIP Journal on Applied Signal Processing*, vol. 2005, pp. 85–98, 2005.

[25] B. L. McKinley and K. L. Bell, "Range-dependence compensation for bistatic stap using focusing matrices", in *2015 IEEE Radar Conference (RadarCon)*, 2015, pp. 1750–1755. DOI: 10.1109/RADAR.2015.7131282.

[26] K Milne, "Principles and concepts of multistatic surveillance radars", in *Radar, International Conf-77*, vol. 1, 1977, pp. 46–52.

[27] H. D. Griffiths and N. R. W. Long, "Television-based bistatic radar", *Communications, Radar and Signal Processing, IEE Proceedings F*, vol. 133, no. 7, pp. 649–657, 1986, ISSN: 0143-7070.

[28] J. Raout, X. Neyt, and P. Rischette, "Bistatic stap using dvb-t illuminators of opportunity", in *Radar Systems, 2007 IET International Conference on*, 2007, pp. 1–5.

[29] H. A. Harms, L. M. Davis, and J. Palmer, "Understanding the signal structure in dvb-t signals for passive radar detection", in *2010 IEEE Radar Conference*, 2010, pp. 532–537.

[30] S. Searle, S. Howard, and J. Palmer, "Remodulation of dvb-t signals for use in passive bistatic radar", in *2010 Conference Record of the Forty Fourth Asilomar Conference on Signals, Systems and Computers*, 2010, pp. 1112–1116.

[31] J. E. Palmer, H. A. Harms, S. J. Searle, and L. Davis, "Dvb-t passive radar signal processing", *IEEE Transactions on Signal Processing*, vol. 61, no. 8, pp. 2116–2126, 2012, ISSN: 1053-587X.

[32] D. Petri, C. Moscardini, M. Conti, A. Capria, J. E. Palmer, and S. J. Searle, "The effects of dvb-t sfn data on passive radar signal processing", in *2013 International Conference on Radar*, 2013, pp. 280–285.

[33] S. Searle, J. Palmer, and L. Davis, "On the effects of clock offset in ofdm-based passive bistatic radar", in *2013 IEEE International Conference on Acoustics, Speech and Signal Processing*, 2013, pp. 3846–3850.

[34] S. Searle, J. Palmer, L. Davis, D. W. O'Hagan, and M. Ummenhofer, "Evaluation of the ambiguity function for passive radar with ofdm transmissions", in *2014 IEEE Radar Conference*, 2014, pp. 1040–1045.

[35] X. Neyt, J. Raout, M. Kubica, V. Kubica, S. Roques, M. Acheroy, and J. Verly, "Feasibility of stap for passive gsm-based radar", in *2006 IEEE Conference on Radar*, 2006, pp. 546–551.

[36] A. Evers and J. Jackson, "Analysis of an LTE waveform for radar applications", in *IEEE Radar Conference*, 2014, pp. 200–205. DOI: 10.1109/RADAR.2014.6875584.

[37] A. A. Salah, R. S. A. R. Abdullah, A. Ismail, F. Hashim, C. Y. Leow, M. B. Roslee, and N. E. A. Rashid, "Feasibility study of lte signal as a new illuminators of opportunity for passive radar applications", in *RF and Microwave Conference (RFM), 2013 IEEE International*, 2013, pp. 258–262.

[38] R. S. A. Raja Abdullah, A. A. Salah, and N. E. Abdul Rashid, "Moving target detection by using new lte-based passive radar", *Progress In Electromagnetics Research B*, vol. 63, pp. 145–160, 2015.

[39] H. D. Griffiths and C. J. Baker, "Measurement and analysis of ambiguity functions of passive radar transmissions", in *IEEE International Radar Conference, 2005.*, 2005, pp. 321–325.

[40] D. Tan, M. Lesturgie, H. Sun, and Y. Lu, "Signal analysis of airborne passive radar using transmissions of opportunity", in *Radar (Radar), 2011 IEEE CIE International Conference on*, vol. 1, 2011, pp. 169–172.

[41] M. Ringer and G. J. Frazer, "Waveform analysis of transmissions of opportunity for passive radar", in *Proceedings of the Fifth International Symposium on Signal Processing and Its Applications*, vol. 2, 1999, 511–514 vol.2.

[42] H. Griffiths and C. Baker, "Passive coherent location radar systems. part 1: Performance prediction", *Radar, Sonar and Navigation, IEE Proceedings -*, vol. 152, no. 3, pp. 153–159, 2005, ISSN: 1350-2395.

[43] C. Baker, H. Griffiths, and I. Papoutsis, "Passive coherent location radar systems. part 2: Waveform properties", *Radar, Sonar and Navigation, IEE Proceedings -*, vol. 152, no. 3, pp. 160–168, 2005, ISSN: 1350-2395.

[44] H. Griffiths and C. Baker, "The signal and interference environment in passive bistatic radar", in *Information, Decision and Control, 2007. IDC '07*, 2007, pp. 1–10.

[45] D. P. Scholnik, "Range-ambiguous clutter suppression with pulse-diverse waveforms", in *2011 IEEE RadarCon (RADAR)*, 2011, pp. 336–341. DOI: 10.1109/RADAR.2011.5960555.

[46] T. Higgins, S. D. Blunt, and A. K. Shackelford, "Time-range adaptive processing for pulse agile radar", in *2010 International Waveform Diversity and Design Conference*, 2010, pp. 115–120.

[47] T. Higgins, K. Gerlach, A. K. Shackelford, and S. D. Blunt, "Aspects of non-identical multiple pulse compression", in *2011 IEEE RadarCon (RADAR)*, 2011, pp. 895–900. DOI: 10.1109/RADAR.2011.5960666.

[48] Y. Zhang and B. Himed, "Space-time adaptive processing in bistatic passive radar exploiting complex bayesian learning", in *Radar Conference, 2014 IEEE*, 2014, pp. 0923–0926. DOI: 10.1109/RADAR.2014.6875723.

[49] Z. Ul Mahmood, M. Alam, K. Jamil, and M. Elnamaky, "On modeling and hardware implementation of space-time adaptive processing (stap) for target detection in passive bi-static radar", in *Information Science, Signal Processing and their Applications (ISSPA), 2012 11th International Conference on*, 2012, pp. 1013–1017.

[50] M. Alam, K. Jamil, and S. M. Alhumaidi, "Target detection using space-time adaptive processing (stap) and a multi-band, multi-channel software defined passive radar", in *Radar Conference (EuRAD), 2015 European*, IEEE, 2015, pp. 552–555. DOI: 10.1109/EuRAD.2015.7346360.

[51] D. Page and G. Owirka, "Knowledge-aided stap processing for ground moving target indication radar using multilook data", *EURASIP Journal on Advances in Signal Processing*, vol. 2006, no. 1, p. 074 838, 2006. DOI: 10.1155/ASP/2006/74838. [Online]. Available: http://dx.doi.org/10.1155/ASP/2006/74838.

[52] Q. Wu, Y. Zhang, M. Amin, and B. Himed, "Space-time adaptive processing and motion parameter estimation in multistatic passive radar using sparse bayesian learning", *Geoscience and Remote Sensing, IEEE Transactions on*, vol. PP, no. 99, pp. 1–1, 2015, ISSN: 0196-2892.

[53] E. Loomis, *The Elements of Analytical Geometry*. New York: Harper & Brothers, 1878.

[54] N. J. Willis, *Bistatic Radar*. SciTech Publishing, Inc, 2005.

[55] J. Burt, "Giovanni domenico cassini", in, Great Neck Publishing, 2006, ISBN: 9781429807555.

[56] I. B. Cohen, "Leibniz on elliptical orbits: As seen in his correspondence with the academie royale des sciences in 1700", *Journal of History of Medicine and Allied Sciences*, vol. 17, no. 1, pp. 72–82, 1962.

[57] A. B. Basset, *An Elementary Treatise on Cubic and Quartic Curves*. Cambridge: Deighton, Bell, 1901.

[58] A. E. Hirst and E. K. Lloyd, "Cassini, his ovals and a space probe to saturn", *The Mathematical Gazette*, vol. 81, no. 492, pp. 409–421, 1997.

[59] J. Ward, "Space-time adaptive processing for airborne radar", Lincoln Laboratory, Massachusetts Institue of Technology Lexington, Massachusetts, Technical Report 1015, 1994.

[60] W. L. Melvin, "A stap overview", *Aerospace and Electronic Systems Magazine, IEEE*, vol. 19, no. 1, pp. 19–35, 2004, ISSN: 0885-8985.

[61] N. J. Willis and H. Griffiths, Eds., *Advances in bistatic radar*. SciTech Publishing, 2007, ch. 11, pp. 432–481.

[62] L. E. Brennan and L. S. Reed, "Theory of adaptive radar", *IEEE Transactions on Aerospace and Electronic Systems*, vol. AES-9, no. 2, pp. 237–252, 1973, ISSN: 0018-9251.

[63] I. S. Reed, J. D. Mallett, and L. E. Brennan, "Rapid convergence rate in adaptive arrays", *Aerospace and Electronic Systems, IEEE Transactions on*, no. 6, pp. 853–863, 1974, ISSN: 0018-9251.

[64] H. L. Van Trees, *Detection, Estimation, and Modulation Theory, Optimum Array Processing*. Wiley, 2004. [Online]. Available: `https://books.google.com/books?id=K5XJC_fMMAwC`.

[65] W.-S. Chen and I. S. Reed, "A new cfar detection test for radar", *Digital Signal Processing*, vol. 1, no. 4, pp. 198–214, 1991, ISSN: 1051-2004/91.

[66] E. J. Kelly, "An adaptive detection algorithm", *IEEE Transactions on Aerospace and Electronic Systems*, vol. AES-22, no. 2, pp. 115–127, 1986, ISSN: 0018-9251.

[67] S. Kraut, L. L. Scharf, and L. T. McWhorter, "Adaptive subspace detectors", *IEEE Transactions on Signal Processing*, vol. 49, no. 1, pp. 1–16, 2001, ISSN: 1053-587X.

[68] R. C. DiPietro, "Extended factored space-time processing for airborne radar systems", in *[1992] Conference Record of the Twenty-Sixth Asilomar Conference on Signals, Systems & Computers*, 1992, 425–430 vol.1.

[69] W. L. Melvin and M. E. Davis, "Adaptive cancellation method for geometry-induced nonstationary bistatic clutter environments", *IEEE Transactions on Aerospace and Electronic Systems*, vol. 43, no. 2, pp. 651–672, 2007, ISSN: 0018-9251.

[70] D. Zwillinger, Ed., *CRC Standard Mathematical Tables and Formulae*, 30th ed. Boca Raton, FL: CRC Press, 1996.

[71] *Lte: Evolved universal terrestrial radio access (e-utra), physical channels and modulation*, European Telecommunications Standards Institute, 2015. [Online]. Available: www.etsi.org.

[72] J. R. Guerci, "Theory and application of covariance matrix tapers for robust adaptive beamforming", *IEEE Transactions on Signal Processing*, vol. 47, no. 4, pp. 977–985, 1999, ISSN: 1053-587X.

[73] ——, *Space-Time Adaptive Processing for Radar*, 2nd. Artech House, 2015.

[74] J. R. Guerci and J. S. Bergin, "Principal components, covariance matrix tapers, and the subspace leakage problem", *IEEE Transactions on Aerospace and Electronic Systems*, vol. 38, no. 1, pp. 152–162, 2002, ISSN: 0018-9251.

[75] D. K. Barton, "Land clutter models for radar design and analysis", *Proceedings of the IEEE*, vol. 73, no. 2, pp. 198–204, 1985, ISSN: 0018-9219/1558-2256.

[76] M. Weiss, "Analysis of some modified cell-averaging cfar processors in multiple-target situations", *IEEE Transactions on Aerospace and Electronic Systems*, vol. 18, no. 1, pp. 102–114, 1982, ISSN: 0018-9251. DOI: 10.1109/TAES.1982.309210.

[77] P. Stoica and R. L. Moses, *Spectral Analysis of Signals*. Pearson Prentice Hall, 2005. [Online]. Available: https://books.google.com/books?id=h78ZAQAAIAAJ.

[78] P. Stoica, H. Li, and J. Li, "A new derivation of the apes filter", *IEEE Signal Processing Letters*, vol. 6, no. 8, pp. 205–206, 1999, ISSN: 1070-9908.

[79] P. M. Djuric, "Spatial spectrum estimation", in *Handbook on Array Processing and Sensor Networks*, S. Haykin and K. J. R. Liu, Eds., Wiley-IEEE Press, 2009, pp. 29–58. [Online]. Available: http://ieeexplore.ieee.org/xpl/articleDetails.jsp?arnumber=5675865.

[80] J. Capon, "High-resolution frequency-wavenumber spectrum analysis", *Proceedings of the IEEE*, vol. 57, no. 8, pp. 1408–1418, 1969, ISSN: 0018-9219.

[81] J. Li and P. Stoica, "An adaptive filtering approach to spectral estimation and sar imaging", *IEEE Transactions on Signal Processing*, vol. 44, no. 6, pp. 1469–1484, 1996, ISSN: 1053-587X.

[82] E. G. Larsson, J. Li, and P. Stoica, *High-resolution nonparametric spectral analysis: Theory and applications*. New York, NY, USA: Marcel-Dekker, 2003.

[83] F. D. Lapierre and J. G. Verly, "Registration-based solutions to the range-dependence problem in stap radars", in *Adaptive Sensor Array Processing (ASAP) Workshop*, 2003.

[84] A. Jakobsson and P. Stoica, "Combining capon and apes for estimation of spectral lines", *Circuits, Systems and Signal Processing*, vol. 19, no. 2, pp. 159–169, 2000. DOI: 10.1007/BF01212468. [Online]. Available: http://dx.doi.org/10.1007/BF01212468.

[85] H. Li, P. Stoica, J. Li, and A. Jakobsson, "On the performance analysis of forward-only and forward-backward matched-filterbank spectral estimators", in *Conference Record of the Thirty-First Asilomar Conference on Signals, Systems and Computers (Cat. No.97CB36136)*, vol. 2, 1998, pp. 1210–1214.

[86] H. Li, J. Li, and P. Stoica, "Performance analysis of forward-backward matched-filterbank spectral estimators", *IEEE Transactions on Signal Processing*, vol. 46, no. 7, pp. 1954–1966, 1998, ISSN: 1053-587X.

[87] S. M. Kay, *Fundamentals of statistical signal processing: Estimation theory*, A. V. Oppenheim, Ed. Prentice-Hall, Inc., 1993, vol. 1, p. 595.

[88] S. M. Kay, *Fundamentals of Statistical Signal Processing, Volume III: Practical Algorithm Development*. Pearson Education, 2013. [Online]. Available: https://books.google.com/books?id=wrBbrJwt4eMC.

[89] W. Wirtinger, "Zur formalen theorie der funktionen von mehr komplexen veränderlichen (on the formal theory of the functions of more complex variables)", in *Mathematische Annalen (Mathematical Annals)*, vol. 97, Springer, 1927, pp. 357–375.

[90] R. F. H. Fischer, *Precoding and Signal Shaping for Digital Transmission*. Wiley, 2005. [Online]. Available: https://books.google.com/books?id=jtputBwrGvcC.

[91] A. V. Oppenheim and R. W. Schafer, *Discrete-time Signal Processing*, 3rd ed. Pearson, 2010.

[92] E. Jacobsen and R. Lyons, "The sliding dft", *IEEE Signal Processing Magazine*, vol. 20, no. 2, pp. 74–80, 2003, ISSN: 1053-5888.

[93] A. Jakobsson, T. Ekman, and P. Stoica, "Computationally efficient 2-d spectral estimation", in *2000 IEEE International Conference on Acoustics, Speech, and Signal Processing. Proceedings (Cat. No.00CH37100)*, vol. 6, 2000, 2151–2154 vol.4.

[94] A. Jakobsson, S. L. Marple, and P. Stoica, "Computationally efficient two-dimensional capon spectrum analysis", *IEEE Transactions on Signal Processing*, vol. 48, no. 9, pp. 2651–2661, 2000, ISSN: 1053-587X.

[95] J. W. Brown and R. V. Churchill, *Complex Variables and Applications*, 9th ed. 2 Penn Plaza, New Yourk, NY 10121: McGraw-Hill Education, 2014, ISBN: 978-0-07-338317-0.

[96] F. J. Flanigan, *Complex Variables: Harmonic and Analytic Functions*. Dover Publications, 1972. [Online]. Available: https://books.google.com/books?id=nGugK5grZPgC.

[97] P. Bouboulis and S. Theodoridis, "Extension of wirtinger's calculus to reproducing kernel hilbert spaces and the complex kernel lms", *IEEE Transactions on Signal Processing*, vol. 59, no. 3, pp. 964–978, 2011, ISSN: 1053-587X.

[98] P. Bouboulis. (2010). Wirtinger's calculus in general hilbert spaces. English, [Online]. Available: https://arxiv.org/pdf/1005.5170.pdf.

[99] H. Li and T. Adali, "Complex-valued adaptive signal processing using nonlinear functions", *EURASIP Journal on Advances in Signal Processing*, vol. 2008, p. 122, 2008.

Appendix A

Wirtinger Calculus

In 1927 the Austrian mathematician Wilhelm Wirtinger formulated a useful method of differential calculus that is being referred to as Wirtinger Calculus. In engineering, finding optimal solutions is a common task. For example, estimation theory often relies on the use of optimal filters derived through constrained minimization problems [87]. For a complex cost function, an analytical solution is found from setting particular partial derivatives of the real and imaginary portions equal to zero. Then the optimal solution is found through solving these set of equations. However, in communications and engineering, it is more common to optimize a real function that depends on complex parameters/signals. Here is where the use of Wirtinger Calculus resides[90].

A.1 Derivatives

Consider first the real valued function of a real variable given as

$$f : \mathbb{R} \ni x \mapsto y = f(x) \in \mathbb{R}. \tag{A.1}$$

Then an extremum is found in some continuous region $\mathcal{R}$ at point x_{opt} only if

$$\left.\frac{\mathrm{d}f}{\mathrm{d}x}\right|_{x_{opt}} \stackrel{!}{=} 0, \tag{A.2}$$

where it is assumed the derivative exists.

Comparable to a real function, a complex function of a complex variable is defined as

$$f : \mathbb{C} \ni z \mapsto w = f(z) \in \mathbb{C}, \tag{A.3}$$

and the derivative is formally given as [95]

$$\begin{aligned} f'(z_0) &\stackrel{\text{def}}{=} \left.\frac{\mathrm{d}f}{\mathrm{d}z}\right|_{z_0} \\ &= \lim_{z \to z_0} \frac{f(z) - f(z_0)}{z - z_0}. \end{aligned} \tag{A.4}$$

Furthermore, if (A.4) exists within a region $\mathcal{R} \subset \mathbb{C}$, then $f(z)$ is analytic[†] in $\mathcal{R}$.

[†]Terms regular and holomorphic can be seen in literature and are synonymous with analytic.

Let $u + jv$ be the value of $f(z)$ when $z = x + jy$. Each real number, u and v, only depend on real variables x and y. Therefore, $f(z)$ can be expressed as

$$f(z) = u(x, y) + jv(x, y). \tag{A.5}$$

With (A.5) defined, $f(z)$ can be classified as analytic if the real component functions, $u(x, y)$ and $v(x, y)$, satisfy the well known Cauchy-Riemann equations of [90], [95]

$$\frac{\partial u(x, y)}{\partial x} = \frac{\partial v(x, y)}{\partial y} \tag{A.6a}$$

$$\frac{\partial v(x, y)}{\partial x} = -\frac{\partial u(x, y)}{\partial y}. \tag{A.6b}$$

If $f(z)$ is analytic, then the complex derivative is expressed as [95]

$$\frac{\mathrm{d}f(z)}{\mathrm{d}z} = \frac{\partial u(x, y)}{\partial x} + j\frac{\partial v(x, y)}{\partial x}. \tag{A.7}$$

In complex analysis, the complex derivative of a complex function serves an important role. However, common engineering optimization problems deal with real functions that can depend on complex variables. Maximization of a complex cost function does not make sence because the maximum modulus principle states [95]

Theorem 1 *If a function f is analytic and not constant in a given domain D, then $|f(z)|$ has no maximum value in D. That is, there is no point z_0 in the domain such that $|f(z)| \leq |f(z_0)|$ for all points z in it.*

Furthermore, minimization does not exist either under the circumstances given by the minimum modulus principle as [96]

Corollary 1.1 *Let f be non-constant analytic on a domain D with $f(z) \neq 0$[‡] for z in D. Then $f(z)$ does not attain its minimum modulus $|f(z)|$ at any point of D.*

Therefore, complex cost functions are of no interest for the optimization problems covered in this paper.

A.2 Wirtinger Calculus

As previously stated, real cost functions of complex variables are of real interest. Therefore, let the functions be defined as

$$f : \mathbb{C} \ni z = x + jy \mapsto w = f(z) = u(x, y) \in \mathbb{R}. \tag{A.8}$$

With $v(x, y) \equiv 0$, the function $f(z)$ is generally not analytic. The only case that satisfies the Cauchy-Riemann equations is when $u(x, y)$ is constant, which is disregarded.

[‡]The stipulation of $f(z) \neq 0$ is necessary to make $1/f(z)$ analytic and defined in D.

To solve for the optimal solution to (A.8), let $f(z) = u(x, y)$. Now $f(z)$ is represented as a function of two real variables instead of a real function of one complex variable. Thus, optimization occurs when the real partial derivatives equal zero [90]. For functions categorized by (A.8), the requirement is written as

$$\begin{aligned} \frac{\partial u(x,y)}{\partial x} &\stackrel{!}{=} 0 \\ \frac{\partial u(x,y)}{\partial y} &\stackrel{!}{=} 0. \end{aligned} \tag{A.9}$$

Combining the requirements above into a linearly complex valued equation leads to

$$a_1 \frac{\partial u(x,y)}{\partial x} + j a_2 \frac{\partial u(x,y)}{\partial y} \stackrel{!}{=} 0 + j0 = 0, \tag{A.10}$$

where a_1 and a_2 are arbitrary non-zero real constants. Equation (A.10) is only equivalent to (A.9) due to the fact that real and imaginary components are orthogonal. This process allows for a more compact representation [90].

Representing the real and imaginary components of z as the ordered pair (x, y) allows the following differential operator to be defined [90]

$$\frac{\partial}{\partial z} \stackrel{\text{def}}{=} a_1 \frac{\partial}{\partial x} + j a_2 \frac{\partial}{\partial y}, \tag{A.11}$$

where the operator can be used on complex functions. This makes sense because real cost functions can be composed of complex functions such as

$$\begin{aligned} f(z) &= |z|^2 \\ &= z \cdot z^* \\ &= f_1(z) \cdot f_2(z). \end{aligned}$$

The final undertaking is assigning values for a_1 and a_2. Wilhelm Wirtinger established these constants as $a_1 = 1/2$ and $a_2 = -1/2$ [89], which meet all necessary requirements as will be shown. With these constants in mind, the partial derivatives of a complex function $f(z)$ with respect to complex variables z and z^* are respectively defined as

$$\frac{\partial f}{\partial z} \stackrel{\text{def}}{=} \frac{1}{2}\left(\frac{\partial f}{\partial x} - j\frac{\partial f}{\partial y}\right) \tag{A.12}$$

and

$$\frac{\partial f}{\partial z^*} \stackrel{\text{def}}{=} \frac{1}{2}\left(\frac{\partial f}{\partial x} + j\frac{\partial f}{\partial y}\right). \tag{A.13}$$

A.2.1 Wirtinger Identities

Let $f(z) = cz$ where c is a complex constant. The derivative with respect to z yields

$$\begin{aligned} \frac{\partial f}{\partial z} &= \frac{1}{2}\left(\frac{\partial c(x+jy)}{\partial x} - j\frac{\partial c(x+jy)}{\partial y}\right) \\ &= \frac{1}{2}\left(c - j\left(jc\right)\right) \\ &= c, \end{aligned} \tag{A.14}$$

whereas the derivative with respect to z^* is

$$\begin{aligned} \frac{\partial f}{\partial z^*} &= \frac{1}{2}\left(\frac{\partial c(x+jy)}{\partial x} + j\frac{\partial c(x+jy)}{\partial y}\right) \\ &= \frac{1}{2}\left(c + j\left(jc\right)\right) \\ &= 0. \end{aligned} \tag{A.15}$$

If $f(z) = cz^*$ then the respective partial derivatives become

$$\begin{aligned} \frac{\partial f}{\partial z} &= \frac{1}{2}\left(\frac{\partial c(x-jy)}{\partial x} - j\frac{\partial c(x-jy)}{\partial y}\right) \\ &= \frac{1}{2}\left(c - j\left(-jc\right)\right) \\ &= 0, \end{aligned} \tag{A.16}$$

and

$$\begin{aligned}\frac{\partial f}{\partial z^*} &= \frac{1}{2}\left(\frac{\partial c(x-jy)}{\partial x} + j\frac{\partial c(x-jy)}{\partial y}\right) \\ &= \frac{1}{2}\left(c + j\left(-jc\right)\right) \\ &= c. \end{aligned} \tag{A.17}$$

For the real function mentioned earlier of $f(z) = zz^* = |z|^2 = x^2 + y^2$, the partial derivatives become

$$\begin{aligned}\frac{\partial}{\partial z}zz^* &= \frac{1}{2}\left(\frac{\partial(x^2+y^2)}{\partial x} - j\frac{\partial(x^2+y^2)}{\partial y}\right) \\ &= \frac{1}{2}\left(2x - j2y\right) \\ &= z^*, \end{aligned} \tag{A.18}$$

and

$$\begin{aligned}\frac{\partial}{\partial z^*}zz^* &= \frac{1}{2}\left(\frac{\partial(x^2+y^2)}{\partial x} + j\frac{\partial(x^2+y^2)}{\partial y}\right) \\ &= \frac{1}{2}\left(2x + j2y\right) \\ &= z. \end{aligned} \tag{A.19}$$

These useful Wirtinger derivatives are summarized in Table A.1.

As illustrated in Table A.1, the derivatives behave similarly to real partial differentiation. Furthermore, z^* is considered a separate variable from that

Table A.1: Wirtinger Derivative Pairs

$f(z)$	$\frac{\partial f(z)}{\partial z}$	$\frac{\partial f(z)}{\partial z^*}$
cz	c	0
cz^*	0	c
zz^*	z^*	z

of z. Some properties from real calculus, such as linearity and the sum, product, and quotient rules, also apply. As an example, if $f(z) = f_1(z)f_2(z)$, then the derivative with respect to z is derived as

$$\begin{aligned}
\frac{\partial}{\partial z}\left(f_1(z)f_2(z)\right) &= \frac{1}{2}\left(\frac{\partial f_1(z)f_2(z)}{\partial x} - j\frac{\partial f_1(z)f_2(z)}{\partial y}\right) \\
&= \frac{1}{2}\left(\frac{\partial f_1(z)}{\partial x}f_2(z) + \frac{\partial f_2(z)}{\partial x}f_1(z)\right. \\
&\qquad \left. -j\frac{\partial f_1(z)}{\partial y}f_2(z) - j\frac{\partial f_2(z)}{\partial y}f_1(z)\right) \\
&= \frac{1}{2}\left(\frac{\partial f_1(z)}{\partial x}f_2(z) - j\frac{\partial f_1(z)}{\partial y}f_2(z)\right) \\
&\qquad \frac{1}{2}\left(\frac{\partial f_2(z)}{\partial x}f_1(z) - j\frac{\partial f_2(z)}{\partial y}f_1(z)\right) \\
&= \frac{\partial f_1(z)}{\partial z}f_2(z) + \frac{\partial f_2(z)}{\partial z}f_1(z). \qquad \text{(A.20)}
\end{aligned}$$

Likewise, the product rule for $\partial/\partial z^*$ is given as [97]

$$\frac{\partial}{\partial z^*}\left(f_1(z)f_2(z)\right) = \frac{\partial f_1(z)}{\partial z^*}f_2(z) + \frac{\partial f_2(z)}{\partial z^*}f_1(z). \tag{A.21}$$

The quotient and chain rules are respectively [97]

$$\frac{\partial}{\partial z}\left(\frac{f_1(z)}{f_2(z)}\right) = \frac{\dfrac{\partial f_1(z)}{\partial z}f_2(z) - \dfrac{\partial f_2(z)}{\partial z}f_1(z)}{(f_2(z))^2} \tag{A.22a}$$

$$\frac{\partial}{\partial z^*}\left(\frac{f_1(z)}{f_2(z)}\right) = \frac{\dfrac{\partial f_1(z)}{\partial z^*}f_2(z) - \dfrac{\partial f_2(z)}{\partial z^*}f_1(z)}{(f_2(z))^2}, \tag{A.22b}$$

and

$$\frac{\partial f(g(z))}{\partial z} = \frac{\partial f(g(z))}{\partial z}\frac{\partial g(z)}{\partial z} + \frac{\partial f(g(z))}{\partial z^*}\frac{\partial g^*(z)}{\partial z} \tag{A.23a}$$

$$\frac{\partial f(g(z))}{\partial z^*} = \frac{\partial f(g(z))}{\partial z}\frac{\partial g(z)}{\partial z^*} + \frac{\partial f(g(z))}{\partial z^*}\frac{\partial g^*(z)}{\partial z^*}, \tag{A.23b}$$

where the proofs for these rules can be found in [98].

A.2.2 Analysis

All though the Wirtinger derivatives generally do not satisfy the Cauchy-Riemann conditions, they are attractive because they obey the rules of cal-

culus and allow computations to be carried out as in a real case [99]. The derivatives can actually be viewed as something inbetween a real derivative of real functions and complex derivative of complex functions [90]. However, if the (A.12) and (A.13) are rewritten as

$$\begin{aligned}\frac{\partial f}{\partial z} &= \frac{1}{2}\left(\frac{\partial\big(u(x,y)+jv(x,y)\big)}{\partial x} - j\frac{\partial\big(u(x,y)+jv(x,y)\big)}{\partial y}\right) \\ &= \frac{1}{2}\left(\frac{\partial u(x,y)}{\partial x} + \frac{\partial v(x,y)}{\partial y} + j\left[\frac{\partial v(x,y)}{\partial x} - \frac{\partial u(x,y)}{\partial y}\right]\right), \quad \text{(A.24)}\end{aligned}$$

and

$$\begin{aligned}\frac{\partial f}{\partial z^*} &= \frac{1}{2}\left(\frac{\partial\big(u(x,y)+jv(x,y)\big)}{\partial x} + j\frac{\partial\big(u(x,y)+jv(x,y)\big)}{\partial y}\right) \\ &= \frac{1}{2}\left(\frac{\partial u(x,y)}{\partial x} - \frac{\partial v(x,y)}{\partial y} + j\left[\frac{\partial v(x,y)}{\partial x} + \frac{\partial u(x,y)}{\partial y}\right]\right), \quad \text{(A.25)}\end{aligned}$$

then the Cauchy-Riemann equations can be satisfied when $f(z)$ is analytic. Substituting (A.6a) and (A.6b) into (A.24) and (A.25) yields

$$\frac{\partial f}{\partial z} = \frac{\partial u(x,y)}{\partial x} + j\frac{\partial v(x,y)}{\partial x} \quad \text{(A.26a)}$$

$$\frac{\partial f}{\partial z^*} = 0. \quad \text{(A.26b)}$$

Therefore, when $f(z)$ is analytic, $\partial f/\partial z$ agrees with (A.7). Furthermore, (A.26b) suggests that analytic functions are not dependent on z^*. However, for non-

analytic functions, such as real cost functions, either $\partial/\partial z$ or $\partial/\partial z^*$ can be implemented for optimization [90].

A.2.3 Multivariate

Typically, practical cost functions rely on many variables where $f : \mathbb{C}^n \ni \mathbf{z} = [z_1, z_2, \ldots, z_n]^{\mathrm{T}} \mapsto w = f(\mathbf{z}) \in \mathbb{R}$. Then the optimal solution is based off n partial derivatives with respect to n unique complex variables. In vector form, these derivatives are known as gradients and are defined as

$$\frac{\partial f}{\partial \mathbf{z}} \stackrel{\text{def}}{=} \left[\frac{\partial f}{\partial z_1}, \quad \frac{\partial f}{\partial z_2}, \quad \cdots, \quad \frac{\partial f}{\partial z_n} \right]^{\mathrm{T}} \tag{A.27}$$

and

$$\frac{\partial f}{\partial \mathbf{z}^*} \stackrel{\text{def}}{=} \left[\frac{\partial f}{\partial z_1^*}, \quad \frac{\partial f}{\partial z_2^*}, \quad \cdots, \quad \frac{\partial f}{\partial z_n^*} \right]^{\mathrm{T}} \tag{A.28}$$

where the optimal solution only exists when the derivatives equal the zero vector, $\mathbf{0} \stackrel{\text{def}}{=} [0, 0, \ldots, 0]^{\mathrm{T}}$ [90].

The Wirtinger pairs in Table A.1 can be easily applied to functions $f(\mathbf{z}) = \mathbf{c}^{\mathrm{T}}\mathbf{z}$ or $f(\mathbf{z}) = \mathbf{c}^{\mathrm{T}}\mathbf{z}^*$ when $\mathbf{c}$ is a vector of constants, $\mathbf{c} = [c_1, c_2, \ldots, c_n]^{\mathrm{T}}$ as

$$\begin{aligned} \frac{\partial}{\partial \mathbf{z}} \mathbf{c}^{\mathrm{T}}\mathbf{z} &= \mathbf{c}, & \frac{\partial}{\partial \mathbf{z}} \mathbf{c}^{\mathrm{T}}\mathbf{z}^* &= \mathbf{0}, \\ \frac{\partial}{\partial \mathbf{z}^*} \mathbf{c}^{\mathrm{T}}\mathbf{z} &= \mathbf{0}, & \frac{\partial}{\partial \mathbf{z}^*} \mathbf{c}^{\mathrm{T}}\mathbf{z}^* &= \mathbf{c}. \end{aligned} \tag{A.29}$$

Then for $f(\mathbf{z}) = \mathbf{z}^{\mathrm{H}}\mathbf{z}$ the derivatives become

$$\frac{\partial}{\partial \mathbf{z}}\mathbf{z}^{\mathrm{H}}\mathbf{z} = \mathbf{z}^{*}, \tag{A.30}$$

and

$$\frac{\partial}{\partial \mathbf{z}^{*}}\mathbf{z}^{\mathrm{H}}\mathbf{z} = \mathbf{z}. \tag{A.31}$$

Finally, a commonly seen quadratic function given as $f(\mathbf{z}) = \mathbf{z}^{\mathrm{H}}\mathbf{A}\mathbf{z}$, where $\mathbf{A}$ represents a $n \times n$ matrix of constants, results in derivatives of [90]

$$\frac{\partial}{\partial \mathbf{z}}\mathbf{z}^{\mathrm{H}}\mathbf{A}\mathbf{z} = \left(\mathbf{z}^{\mathrm{H}}\mathbf{A}\right)^{\mathrm{T}}, \tag{A.32}$$

and

$$\frac{\partial}{\partial \mathbf{z}^{*}}\mathbf{z}^{\mathrm{H}}\mathbf{A}\mathbf{z} = \mathbf{A}\mathbf{z}. \tag{A.33}$$

Table A.2 summarizes these Wirtinger multivariate derivative pairs.

Table A.2: Wirtinger Multivariate Derivative Pairs

$f(\mathbf{z})$	$\frac{\partial f(\mathbf{z})}{\partial \mathbf{z}}$	$\frac{\partial f(\mathbf{z})}{\partial \mathbf{z}^{*}}$
$\mathbf{c}^{\mathrm{T}}\mathbf{z} = \mathbf{z}^{\mathrm{T}}\mathbf{c}$	$\mathbf{c}$	$\mathbf{0}$
$\mathbf{c}^{\mathrm{T}}\mathbf{z}^{*} = \mathbf{z}^{\mathrm{H}}\mathbf{c}$	$\mathbf{0}$	$\mathbf{c}$
$\mathbf{z}^{\mathrm{H}}\mathbf{z} = \mathbf{z}^{\mathrm{T}}\mathbf{z}^{*}$	$\mathbf{z}^{*}$	$\mathbf{z}$
$\mathbf{z}^{\mathrm{H}}\mathbf{A}\mathbf{z} = \mathbf{z}^{\mathrm{T}}\mathbf{A}^{\mathrm{T}}\mathbf{z}^{*}$	$\mathbf{A}^{\mathrm{T}}\mathbf{z}^{*}$	$\mathbf{A}\mathbf{z}$